JETP Letters, Vol. 81, No. 9, 2005, pp. 417–423. From Pis'ma v Zhurnal Éksperimental'noĭ i Teoreticheskoĭ Fiziki, Vol. 81, No. 9, 2005, pp. 531–537.

Observation of a Tensor Glueball in the Reactions $p\bar{p} \longrightarrow \pi\pi, \eta\eta, \eta\eta'$ ¶

V. V. Anisovich and A. V. Sarantsev

St. Petersburg Nuclear Physics Institute, Russian Academy of Sciences, Gatchina, 188300 Russia

Received March 28, 2005

Partial wave analysis of the reactions $p\bar{p} \longrightarrow \pi\pi, \eta\eta, \eta\eta'$ in the region of invariant masses 1900–2400 MeV indicates the existence of four relatively narrow tensor–isoscalar resonances $f_2(1920)$, $f_2(2020)$, $f_2(2240)$, $f_2(2300)$, as well as the broad state $f_2(2000)$. The determined decay couplings of the broad resonance $f_2(2000) \longrightarrow \pi^0\pi^0, \eta\eta, \eta\eta'$ satisfy the relations appropriate to those of a tensor glueball, while the couplings of other tensor states do not, thus verifying the glueball nature of $f_2(2000)$. © *2005 Pleiades Publishing, Inc.*

PACS numbers: 12.38.–t, 12.39.–MK, 14.40.–n

In [1], a combined partial wave analysis was performed for the high statistics data on the reactions $p\bar{p} \longrightarrow \pi^0\pi^0, \eta\eta, \eta\eta'$ taken at antiproton momenta 600, 900, 1150, 1200, 1350, 1525, 1640, 1800, and 1940 MeV/c together with data obtained for a polarized target in the reaction $p\bar{p} \longrightarrow \pi^+\pi^-$ [2] that resulted in the determination of a number of isoscalar resonances f_J with $J = 0, 2, 4$ (for a review, see [3–5]). In the 02^{++}-sector, five states are required to describe the data [1, 3]:

Resonance	Mass (MeV)	Width (MeV)
$f_2(1920)$	1920 ± 30	230 ± 40
$f_2(2000)$	2010 ± 30	495 ± 35
$f_2(2020)$	2020 ± 30	275 ± 35
$f_2(2240)$	2240 ± 40	245 ± 45
$f_2(2300)$	2300 ± 35	290 ± 50.

(1)

The resonance $f_2(1920)$ was observed earlier in the spectra $\omega\omega$ [6–8] and $\eta\eta'$ [9, 10] (see also compilation [11]). For the broad tensor–isoscalar resonance in the region around 2000 MeV, the recent analyses give the following: $M = 1980 \pm 20$ MeV, $\Gamma = 520 \pm 50$ MeV in $pp \longrightarrow pp\pi\pi\pi\pi$ [12] and $M = 2050 \pm 30$ MeV, $\Gamma = 570 \pm 70$ MeV in $\pi^- p \longrightarrow \phi\phi n$[13]. Following [1, 12, 13], we denote the broad resonance as $f_2(2000)$.

The description of data in the reactions $p\bar{p} \longrightarrow \pi^0\pi^0, \eta\eta, \eta\eta'$ is illustrated in Fig. 1. In Figs. 2 and 3, one can see the differential cross sections $p\bar{p} \longrightarrow \pi^+\pi^-$, while Fig. 4 presents the polarization data. In Fig. 5, we show cross sections for $p\bar{p} \longrightarrow \pi^0\pi^0, \eta\eta, \eta\eta'$ in the $^3P_2\,\bar{p}p$ and $^3F_2\,\bar{p}p$ waves (dashed and dotted curves) and total ($J = 2$) cross section (solid curve), as well as the Argand plots for the $^3P_2$ and $^3F_2$ wave amplitudes at invariant masses $M = 1.962$, 2.050, 2.100, 2.150, 2.200, 2.260, 2.304, 2.360, and 2.410 GeV.

Partial wave analysis [1, 3] together with recent data for $\gamma\gamma \longrightarrow K_S K_S$ [14] and reanalysis of $\phi\phi$ spectra [13] have clarified the situation with f_2 mesons in the mass region 1700–2400 MeV. Based on these data, there was performed in [15] a systematization of the nonexotic f_2 mesons on the (n, M^2) trajectories, where n is the radial quantum number of the $q\bar{q}$ state. The systematization in [15] shows us that the broad resonance $f_2(2000 \pm 30)$ is an extra state for the (n, M^2) trajectories, being apparently the lowest tensor glueball. However, the statement about the glueball nature of $f_2(2000)$ was based on indirect arguments:

(i) The leading Pomeron trajectory $\alpha_P(M^2) = \alpha_P(0) + \alpha'_P(0)M^2$ has the following values for the intercept and slope: $\alpha(0) \simeq 1.10$–1.30 and $\alpha'_P(0) \simeq 0.15$–0.25 (see, for example, [16–18]). For the tensor glueball, these Pomeron parameters give $M \simeq 1.7$–2.5 GeV.

(ii) In the lattice calculations, a close value was obtained, namely, $M \simeq 2.2$–2.4 GeV [19].

(iii) The large width of $f_2(2000)$ can be considered a signature of the glueball origin of this state. An exotic state appearing in a set of $q\bar{q}$ resonances accumulates their widths, thus transforming into a broad resonance [20]. The phenomenon of width accumulation has been studied in [21, 22] for the scalar glueball $f_0(1200$–$1600)$, and, much earlier, this phenomenon was observed in nuclear physics [23–25].

Direct arguments for the glueball nature of $f_2(2000)$ can be provided by the relations between decay cou-

¶ This article was submitted by the authors in English.

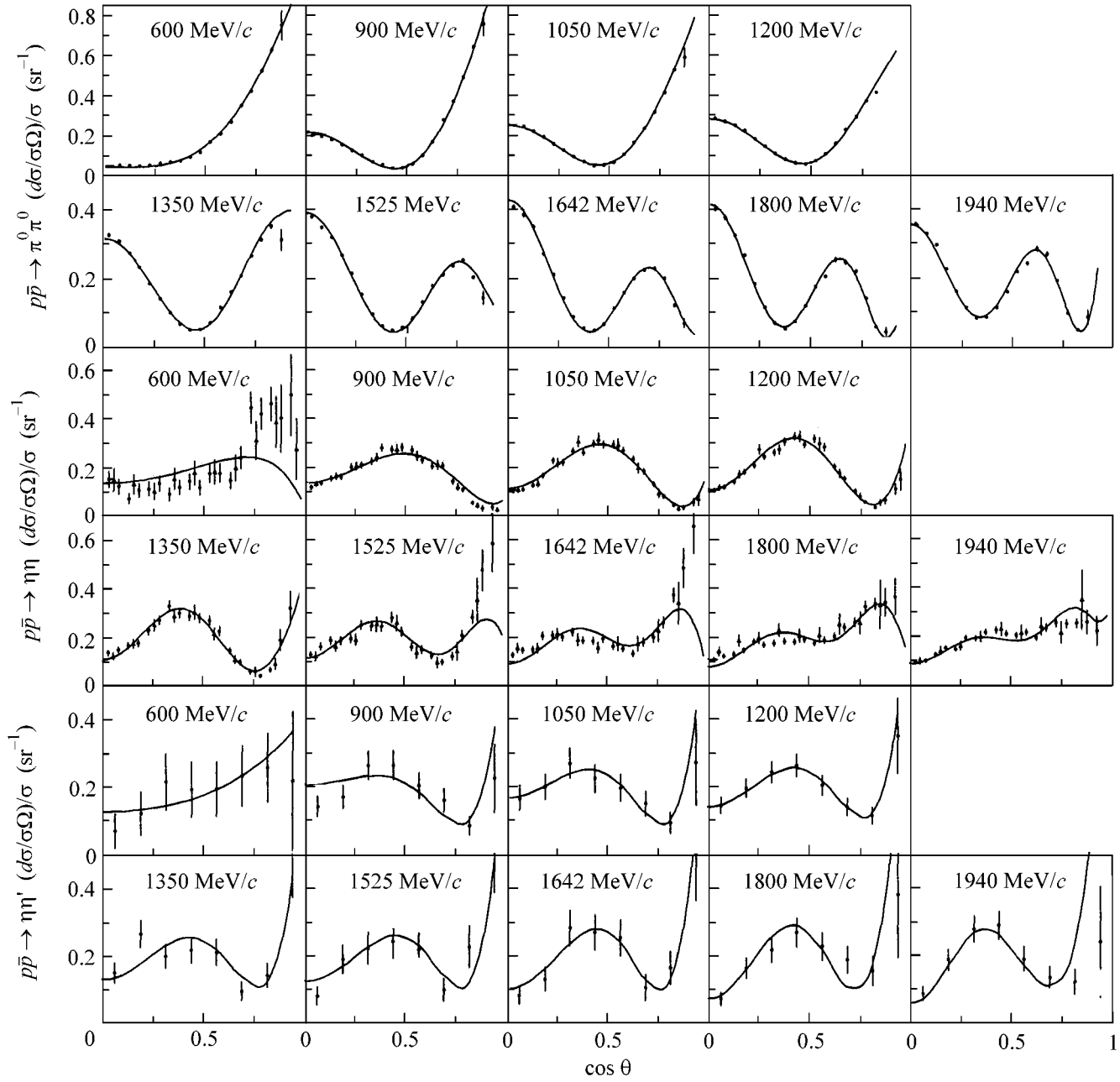

Fig. 1. Angular distributions in the reactions $p\bar{p} \longrightarrow \pi\pi$, $\eta\eta$, $\eta\eta'$ and their fit to resonances of Eq. (1).

pling constants, and, for a tensor glueball, such relations were presented in [15]. In [1, 3], the extraction of the decay couplings $f_J \longrightarrow \pi\pi$, $\eta\eta$, $\eta\eta'$ was not performed; in the present paper, we fill in this gap. The $\bar{p}p \longrightarrow \pi^0\pi^0$, $\eta\eta$, $\eta\eta'$ amplitudes provide us with the following ratios for the f_2 resonance couplings, $g_{\pi^0\pi^0}$: $g_{\eta\eta} : g_{\eta\eta'}$:

$$
\begin{aligned}
f_2(1920):&\quad 1 : 0.56 \pm 0.08 : 0.41 \pm 0.07,\\
f_2(2000):&\quad 1 : 0.82 \pm 0.09 : 0.37 \pm 0.22,\\
f_2(2020):&\quad 1 : 0.70 \pm 0.08 : 0.54 \pm 0.18,\\
f_2(2240):&\quad 1 : 0.66 \pm 0.09 : 0.40 \pm 0.14,\\
f_2(2300):&\quad 1 : 0.59 \pm 0.09 : 0.56 \pm 0.17.
\end{aligned}
\qquad (2)
$$

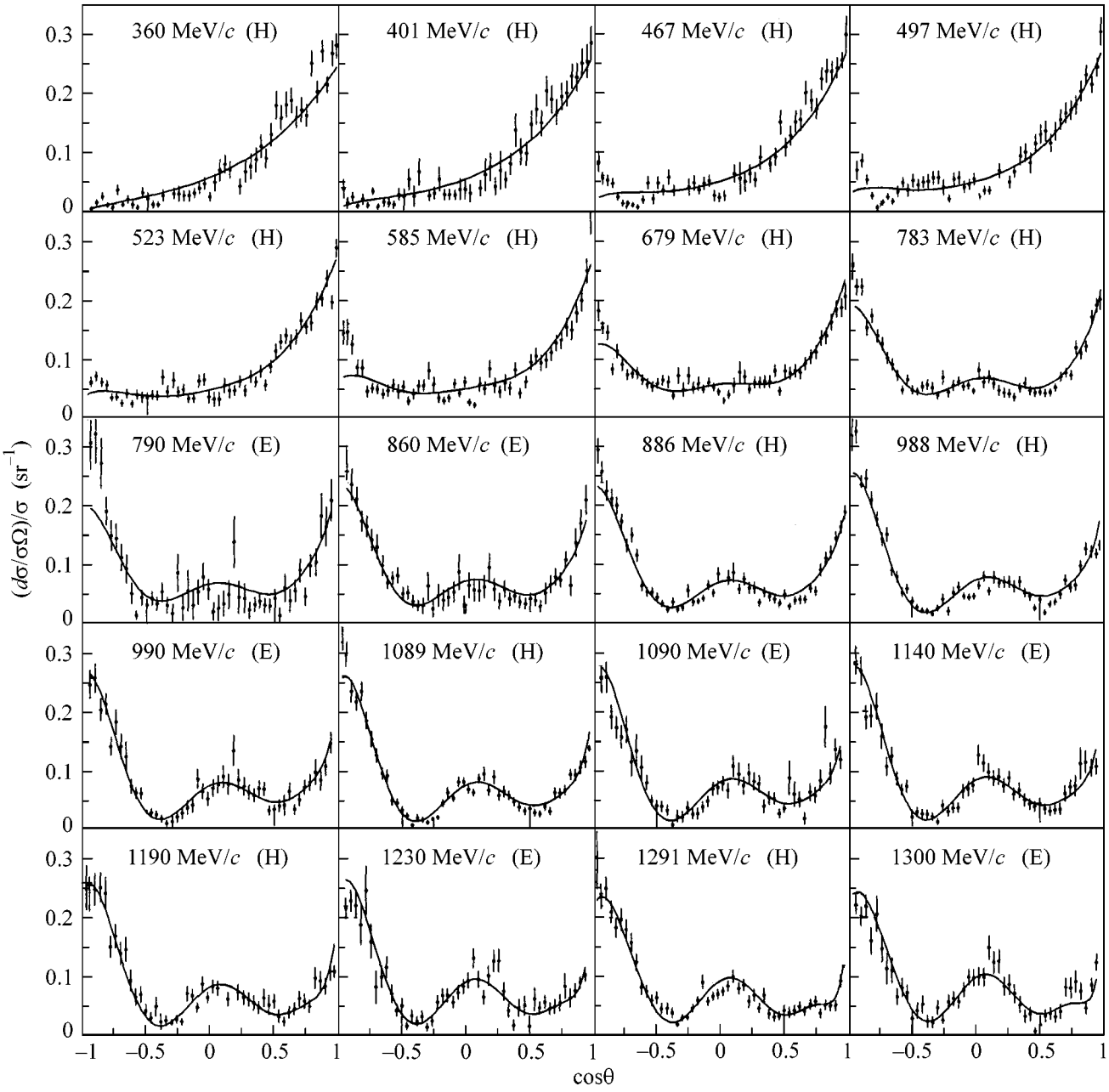

Fig. 2. Differential cross sections for the reaction $p\bar{p} \longrightarrow \pi^+\pi^-$ at proton momenta 360–1300 MeV and their fit to the resonances of Eq. (1). (E) and (H) refer to experimental data [2] of Eisenhandler *et al.* and Hasan *et al.*, correspondingly.

These ratios are to be compared with those given in [15].

In the leading terms of the $1/N_c$ expansion [26], there exist definite ratios for the glueball decay couplings. The next-to-leading terms in the decay couplings give the corrections of the order of $1/N_c$ (see, for example, [4]); numerical calculations of diagrams tell us that the $1/N_c$ factor leads to a smallness of the order of 1/10, and, thus, we neglect these terms. For the transition tensor glueball $\longrightarrow \pi^0\pi^0, \eta\eta, \eta\eta'$, the relations in the leading terms of the $1/N_c$ expansion read as follows (see table in [15]):

$$g^{(\text{glueball})}_{\pi^0\pi^0} : g^{(\text{glueball})}_{\eta\eta} : g^{(\text{glueball})}_{\eta\eta'} = 1 : (\cos^2\theta + \lambda\sin^2\theta) : (1-\lambda)\sin\theta\cos\theta. \quad (3)$$

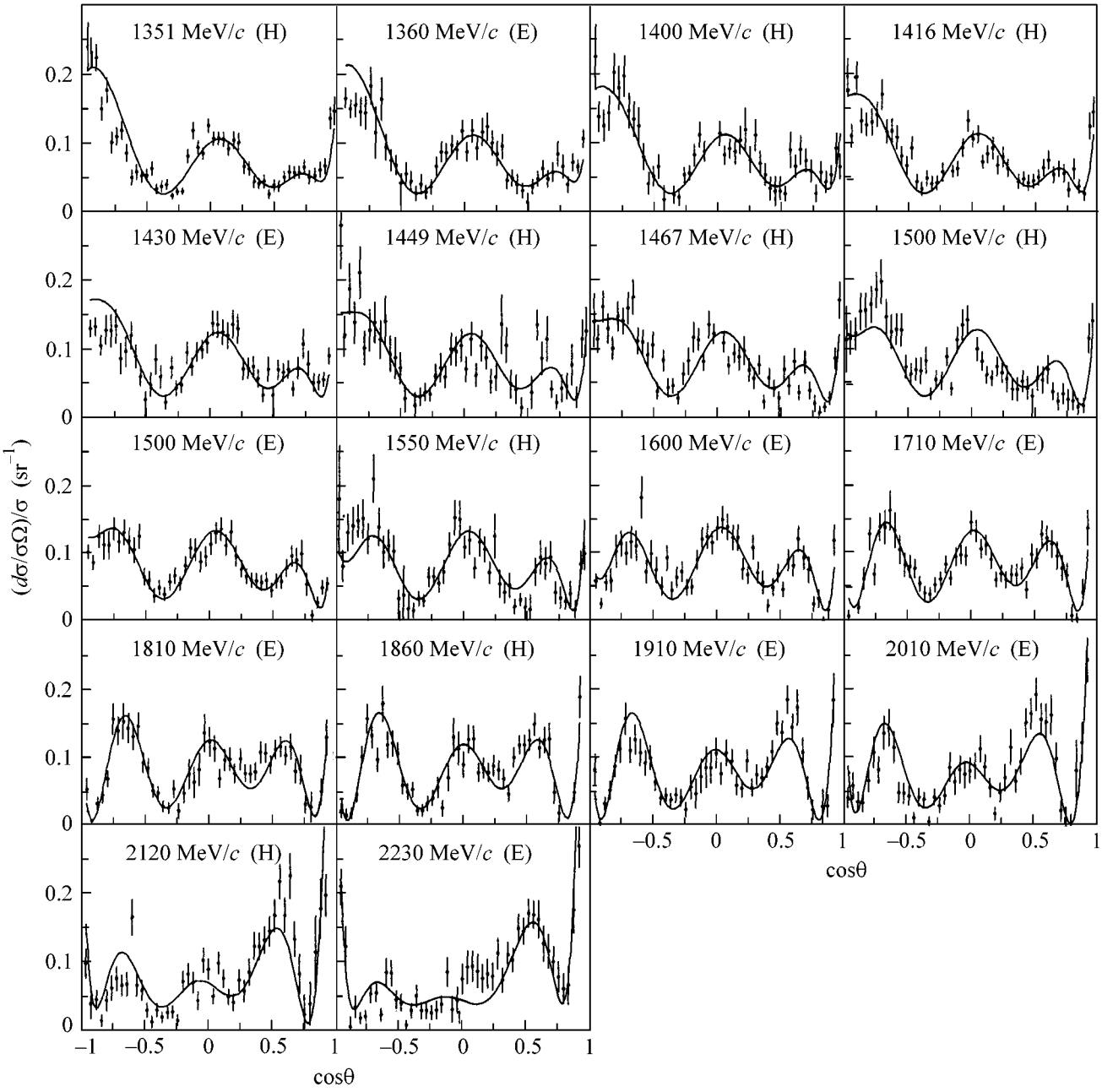

Fig. 3. Differential cross sections for the reaction $p\bar{p} \longrightarrow \pi^+\pi^-$ at proton momenta 1350–2230 MeV and their fit to the resonances of Eq. (1).

Here, θ is the mixing angle for η – η' mesons: $\eta = n\bar{n}\cos\theta - s\bar{s}\sin\theta$ and $\eta' = n\bar{n}\sin\theta + s\bar{s}\cos\theta$, where $n\bar{n} = (u\bar{u} + d\bar{d})/\sqrt{2}$. We neglect a possible admixture of the gluonium component in η and η' (according to [27], the gluonium admixture in η is less than 5%, and, in η', it is less than 20%). For the mixing angle θ, we use θ = 37°.

The suppression parameter λ determines the relative production probability of strange quarks by a gluon field: $u\bar{u} : d\bar{d} : s\bar{s} = 1 : 1 : \lambda$ with $0 \le \lambda \le 1$. The data

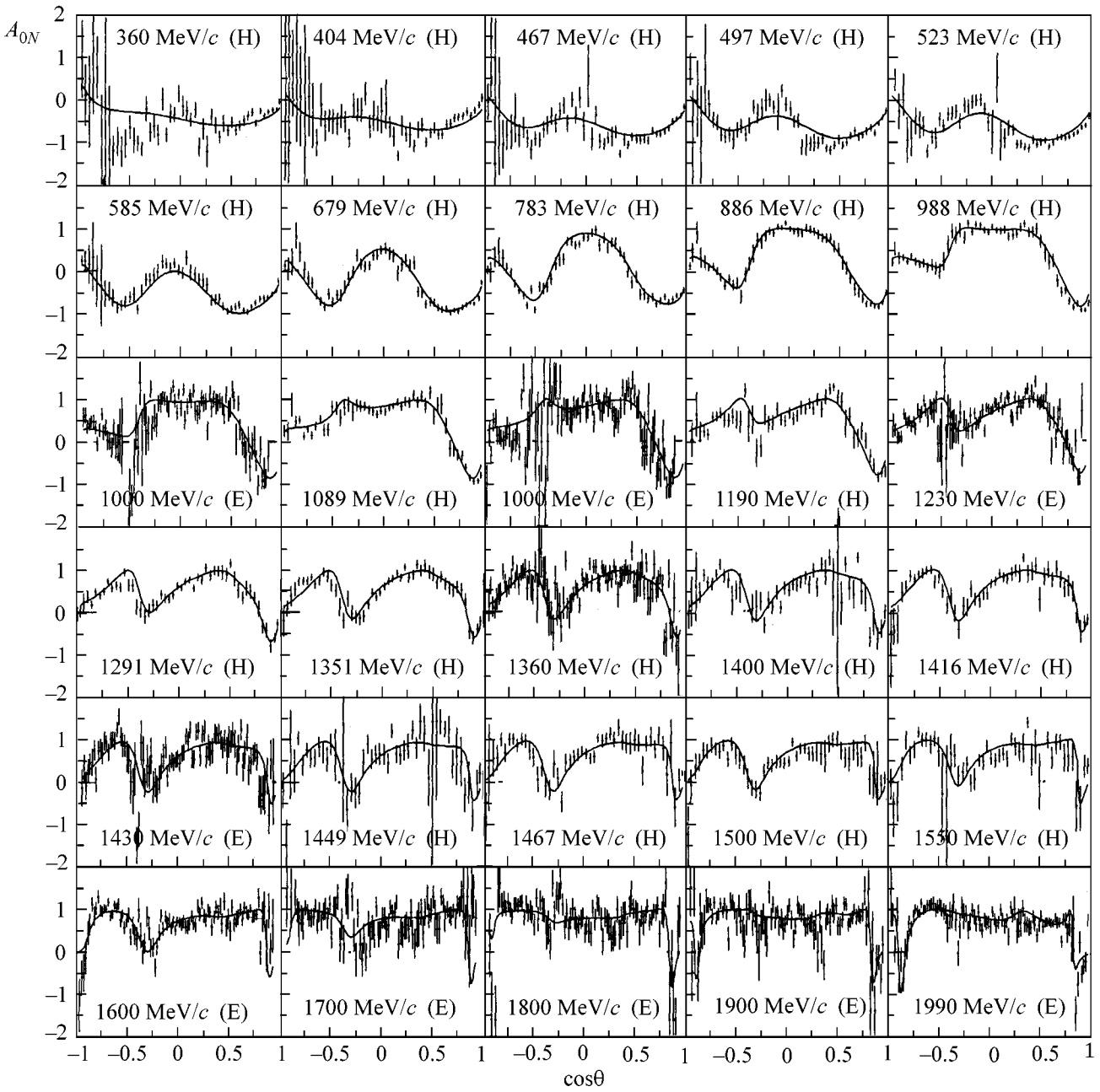

Fig. 4. Polarization in $p\bar{p} \longrightarrow \pi^+\pi^-$ and its fit to the resonances of Eq. (1).

provide us with the following values of this parameter: $\lambda \simeq 0.5$ [28] for central hadron production in hadron–hadron high-energy collisions, $\lambda = 0.5$–0.8 [29] for the decay of tensor mesons, and $\lambda = 0.5$–0.9 [30] for the decays of 0^{++} mesons.

For ($\lambda = 0.5$, $\theta = 37°$), Eq. (3) gives us $1 : 0.82 : 0.24$, and, for ($\lambda = 0.85$, $\theta = 37°$), correspondingly, $1 : 0.95 : 0.07$. Consequently, the relations between the coupling constants $g_{\pi^0\pi^0} : g_{\eta\eta} : g_{\eta\eta'}$ for the glueball are as follows:

$$2^{++}\text{glueball}\ \ g_{\pi^0\pi^0} : g_{\eta\eta} : g_{\eta\eta'} = 1 : (0.82\text{–}0.95) : (0.24\text{–}0.07). \quad (4)$$

We see from (2) that precisely the coupling constants of the broad $f_2(2000)$ resonance are inside the intervals:

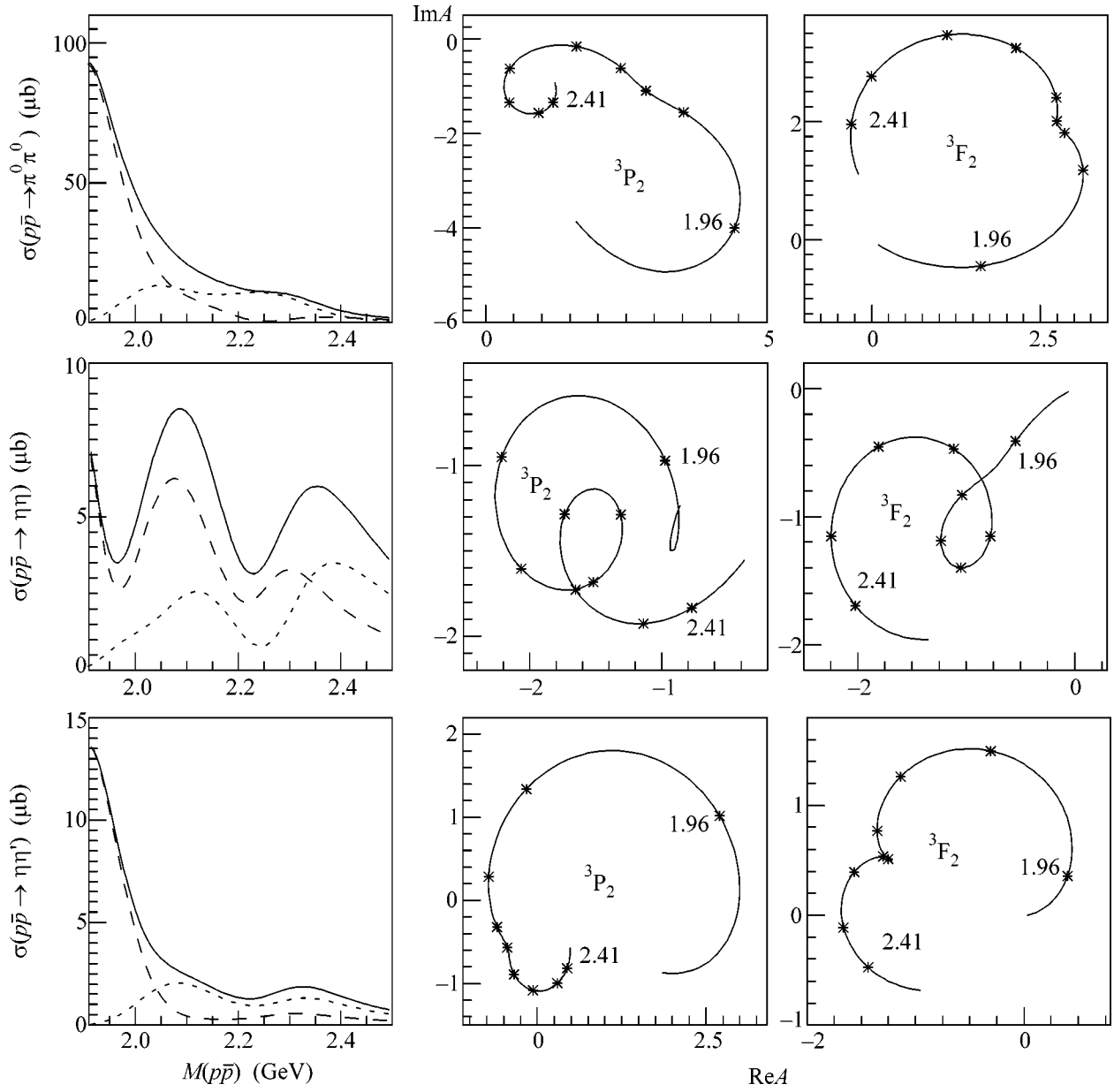

Fig. 5. Cross sections and Argand plots for $^3P_2$ and $^3F_2$ waves in the reaction $p\bar{p} \longrightarrow \pi^0\pi^0$, ηη, ηη'. The upper row refers to $p\bar{p} \longrightarrow \pi^0\pi^0$: we demonstrate the cross sections for $^3P_2$ and $^3F_2$ waves (dashed and dotted lines, correspondingly) and total (J = 2) cross section (solid line) as well as Argand plots for the $^3P_2$ and $^3F_2$ wave amplitudes at invariant masses M = 1.962, 2.050, 2.100, 2.150, 2.200, 2.260, 2.304, 2.360, and 2.410 GeV. The figures on the second and third rows refer to the reactions $p\bar{p} \longrightarrow \eta\eta$ and $p\bar{p} \longrightarrow \eta\eta'$.

$0.82 \le g_{\eta\eta}/g_{\pi^0\pi^0} \le 0.95$ and $0.24 \ge g_{\eta\eta'}/g_{\pi^0\pi^0} \ge 0.07$. Hence, it is just this resonance, which can be considered a tensor glueball, with λ being fixed in the interval $0.5 \le \lambda \le 0.7$.

Taking into account that there is no room for $f_2(2000)$ on the (n, M^2) trajectories [15], it becomes clear that this resonance is indeed the lowest tensor glueball.

We are grateful to A.V. Anisovich, D.V. Bugg, L.G. Dakhno, M.A. Matveev, and V.A. Nikonov for useful discussions. This work was supported by the Russian Foundation for Basic Research (project no. 04-02-17091).

REFERENCES

1. A. V. Anisovich *et al.*, Phys. Lett. B **491**, 47 (2000).

2. E. Eisenhandler *et al.*, Nucl. Phys. B **98**, 109 (1975); A. Hasan *et al.*, Nucl. Phys. B **378**, 3 (1992).
3. A. V. Anisovich, V. A. Nikonov, A. V. Sarantsev, and V. V. Sarantsev, in *Proceedings of PNPI XXX: Scientific Highlight, Theoretical Physics Division* (Gatchina, 2001), p. 58.
4. V. V. Anisovich, Usp. Fiz. Nauk **174**, 49 (2004) [Phys. Usp. **47**, 45 (2004)].
5. D. V. Bugg, Phys. Rep. **397**, 257 (2004).
6. G. M. Beladidze *et al.* (VES Collab.), Z. Phys. C **54**, 367 (1992).
7. D. M. Alde *et al.* (GAMS Collab.), Phys. Lett. B **241**, 600 (1990).
8. D. Barberis *et al.* (WA 102 Collab.), Phys. Lett. B **484**, 198 (2000).
9. D. M. Alde *et al.* (GAMS Collab.), Phys. Lett. B **276**, 375 (1992).
10. D. Barberis *et al.* (WA 102 Collab.), Phys. Lett. B **471**, 429 (2000).
11. S. Eidelman *et al.* (PDG), Phys. Lett. B **592**, 1 (2004).
12. D. Barberis *et al.* (WA 102 Collab.), Phys. Lett. B **471**, 440 (2000).
13. R. S. Longacre and S. J. Lindenbaum, Report BNL-72371-2004.
14. V. A. Schegelsky, A. V. Sarantsev, and V. A. Nikonov, *Phenomenological Investigation of the K_SK_S Final State in Two-Photon Collisions and Nonet Classification of Tensor Resonances* (2004), L3 Note 3001.
15. V. V. Anisovich, Pis'ma Zh. Éksp. Teor. Fiz. **80**, 845 (2004) [JETP Lett. **80**, 715 (2004)]; hep-ph/0412093.
16. A. B. Kaidalov and K. A. Ter-Martirosyan, Sov. J. Nucl. Phys. **39**, 979 (1984).
17. P. V. Landshoff, in *QCD: 20 Years Later*, Ed. by P. M. Zerwas and H. A. Kastrup (World Sci., Singapore, 1993).
18. L. G. Dakhno and V. A. Nikonov, Eur. Phys. J. A **5**, 209 (1999).
19. G. S. Bali, K. Schilling, A. Hulsebos, *et al.* (UK QCD Collab.), Phys. Lett. B **309**, 378 (1993); C. J. Morningstar and M. J. Peardon, Phys. Rev. D **60**, 034 509 (1999).
20. V. V. Anisovich, D. V. Bugg, and A. V. Sarantsev, Phys. Rev. D **58**, 111 503 (1998).
21. V. V. Anisovich, Yu. D. Prokoshkin, and A. V. Sarantsev, Phys. Lett. B **389**, 388 (1996); Z. Phys. A **357**, 123 (1997).
22. A. V. Anisovich, V. V. Anisovich, and A. V. Sarantsev, Phys. Lett. B **395**, 123 (1997); Z. Phys. A **359**, 173 (1997).
23. I. S. Shapiro, Nucl. Phys. A **122**, 645 (1968).
24. I. Yu. Kobzarev, N. N. Nikolaev, and L. B. Okun, Yad. Fiz. **10**, 864 (1969) [Sov. J. Nucl. Phys. **10**, 499 (1969)].
25. L. Stodolsky, Phys. Rev. D **1**, 2683 (1970).
26. G. 't Hooft, Nucl. Phys. B **72**, 461 (1974); G. Veneziano, Nucl. Phys. B **117**, 519 (1976).
27. V. V. Anisovich, D. V. Bugg, D. I. Melikhov, and V. A. Nikonov, Phys. Lett. B **404**, 166 (1997).
28. V. V. Anisovich, M. G. Huber, M. N. Kobrinsky, and B. Ch. Metsch, Phys. Rev. D **42**, 3045 (1990).
29. K. Peters and E. Klempt, Phys. Lett. B **352**, 467 (1995).
30. V. V. Anisovich and A. V. Sarantsev, Eur. Phys. J. A **16**, 229 (2003).

JETP Letters, Vol. 81, No. 9, 2005, pp. 424–426. Translated from Pis'ma v Zhurnal Éksperimental'noĭ i Teoreticheskoĭ Fiziki, Vol. 81, No. 9, 2005, pp. 538–540.

Magnetic Quantum Beating of Gamma Radiation on ^{181}Ta Nuclei

A. V. Mitin[1], V. Yu. Lyubimov[2], and É. K. Sadykov[2]

[1] *Kazan State Technological University, ul. Karla Marksa 68, Kazan, 420015 Tatarstan, Russia*

[2] *Kazan State University, ul. Kremlevskaya 18, Kazan, 420008 Tatarstan, Russia*

Received March 29, 2005

A frequency–time variant of gamma resonance spectroscopy is suggested with the use of quantum interference on Mössbauer transitions induced under the conditions of gamma magnetic resonance. Calculations are performed for the ^{181}Ta nucleus. It has been shown that the coherent dynamics of nuclear spins is essential for the formation of the time harmonics of the absorption spectrum. © *2005 Pleiades Publishing, Inc.*

PACS numbers: 61.18.Fs

Investigation of the effects of quantum interference in the gamma range is one of the urgent tasks of modern Mössbauer spectroscopy. These effects were previously sought by traditional (stationary) methods for measuring frequency spectra. At present, we focus on the frequency–time regime of measurements. The ^{181}Ta isotope is most convenient for realizing this method. Mössbauer experiments with the ^{181}Ta nucleus (6.2-keV transition) were carried out as early as in the 1970s [1–3]. However, unclear separation of Mössbauer spectral lines of the ^{181}Ta nucleus owing to a considerable (more than an order of magnitude) inhomogeneous broadening hampered the use of the advantage of this isotope, which is determined by a small spontaneous width $W_0 = 2\hbar/\tau = 0.0064$ mm/s. At the same time, features of gamma resonance spectroscopy of nonlinearly excited spin systems [4–6] were demonstrated with this isotope. In some cases, this spectroscopy allows for the separation of narrow lines with spontaneous width (e.g., by using the gamma magnetic resonance method [7, 8]). This method is based on the separation of spin packets whose superfine fields are in resonance with the rf magnetic field used in the regimes of scanning and frequency modulation [7–9].

In this work, we suggest a spectroscopy based on the use of harmonics arising in the absorption spectrum when gamma magnetic resonance is excited due to quantum magnetic beating associated with the interference of Rabi states. The possibility of their generation was analyzed in [10], and a detailed theory was developed more recently in [11]. At the same time, the frequency–time method was used in [12] to observe quantum beating of gamma radiation that are induced by ultrasonic Doppler modulation. In that work, the time harmonics of a spectrum was observed using a time–amplitude converter. Experiments on the induction of gamma magnetic resonance harmonics have not yet been carried out. Only observations of the magnetic modulation of gamma radiation for low frequencies are known [13–15]. Experiments on the detection of harmonics with a frequency of several tens of megahertz that are in resonance with the nuclear Larmor frequencies of the ^{57}Fe nucleus were not carried out, because the time–amplitude converter must trigger with subnanosecond accuracy in such experiments. At the same time, the ^{181}Ta nucleus can have Larmor frequencies of several megahertzs, which are acceptable for time experiments. Another motivation for this investigation is the determination of the significance of the interference between the Rabi states of the ground and excited isomer levels of a Mössbauer nucleus [11, 16].

The spectrum of harmonics will be analyzed using the results obtained in [11]. The intensity of the emission or absorption of gamma rays in a thin source or an absorber, respectively, is given by the expression

$$P = \pm f^{(s)}\tau\frac{2L+1}{2I_e+1}\mathrm{Re}\sum_{g_1, e_1} F$$

$$\times \sum_{p,\, p' = \pm 1} (pp')^{\varepsilon} e^{i(p-p')\Psi} d^L_{p,\, M-Q}(\Theta) d^L_{p,\, M}(\Theta) e^{i(\Omega t + \phi)} \hat{\chi} \quad (1)$$

$$\times \sum_{Q=-2L}^{2L} \frac{S^{(M)}_{g_1, e_1}(\beta_g, \beta_e) S^{(M-Q)}_{g_1, e_1}(\beta_g, \beta_e)\Gamma_{\exp}}{i[a_e e_1 - a_g g_1 + M\Omega - D] + \Gamma_{\exp}/2}.$$

Here,

$$S^{(M-Q)}_{g_1, e_1}(\beta_g, \beta_e)$$

$$= \sum_{g, e} d^{(I_g)}_{g_1 g}(\beta_g) C(I_g, L, I_e; g, M-Q, e) d^{(I_e)}_{e_1 e}(\beta_e). \quad (2)$$

$\Gamma_{\exp} = \Gamma^S + \Gamma^A$; $F = 1 + 2i\xi$, where ξ is the interference factor between a nuclear internal-conversion absorp-

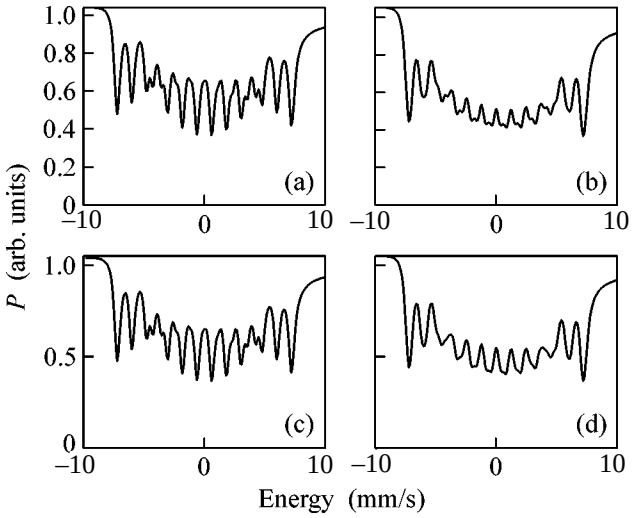

Fig. 1. Stationary spectrum of the ^{181}Ta nucleus for a constant field H_0 = 3.4 kOe (a) in the absence of a variable field and in the presence of an rf magnetic field with frequency Ω = (b) 3, (c) 4, and (d) 3 MHz and amplitude H_1 = (b) 180, (c) 150, and (d) 150 Oe.

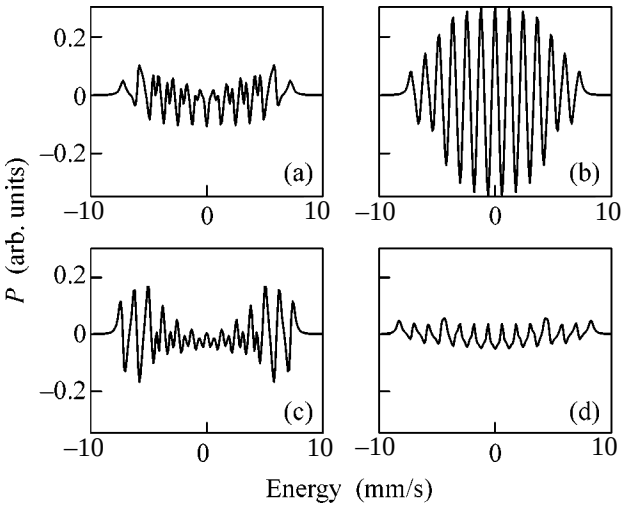

Fig. 2. Spectrum of the real part of the first-harmonic amplitude (P_1') for a constant field H_0 = 3.4 kOe and variable field H_1 = 150 Oe with frequency Ω = (a) ω_g = 1.7 MHz, (b) 2.3 MHz, (c) ω_e = 3 MHz, and (d) 4 MHz.

tion and photoelectric absorption (ξ = –0.08 for ^{181}Ta [17]); $\chi_{pp'}$ is the polarization density matrix; $\tau = \sigma_0 nzf^{(A)}$ is the effective width of the absorber; and $d(\ldots)$ are the Wigner functions. The effective angles β_r and a_r ($r = g$ or e) are determined by the equations

$$\begin{aligned} a_r \sin\beta_r &= w_{1r}/2, \\ a_r \cos\beta_r &= w_{0r} - \Omega, \end{aligned} \tag{3}$$

where D is the Doppler shift and ϵ = 0 or 1 for the electric or magnetic gamma transitions, respectively, whose quantum numbers for the ground and excited states are denoted by the subscripts g and e, respectively. The remaining notation is standard.

Calculations were performed for experimental data reported by Voĭtovetskiĭ *et al.* [16, 18]. For a thin source, the gamma magnetic resonance spectrum includes the zeroth, first, and second harmonics, and Eq. (1) is represented as

$$\begin{aligned} P &= P_{st} + P_1'\cos(\Omega t + \phi) + P_1''\sin(\Omega t + \phi) \\ &+ P_2'\cos(2\Omega t + \phi) + P_2''\sin(2\Omega t + \phi). \end{aligned} \tag{4}$$

Figure 1 shows the Mössbauer spectra calculated under the conditions of exciting gamma magnetic resonance. These spectra reproduce, at least, qualitatively, the absorption spectra obtained in [18]. This agreement corroborates the validity of the theory under consideration. We emphasize that the Mössbauer spectra shown in Figs. 1b and 1d for a frequency of 3 MHz that is in resonance with the Larmor frequency of the excited level are rather smeared and are not suitable for accurate measurements of the parameters of the material of an isotope matrix.

The intensities of spectral lines for a weak rf magnetic field are a power function of the rf magnetic field strength, with an exponent that is equal to the order of the harmonic, and the shape of the lines is characterized by the shape of curves determined by the same-order derivative of the Lorentz shape function with respect to the Doppler shift [19]. Hence, for the chosen values H_1 = 150 and 300 Oe, the intensities of the spectral lines of the second harmonic are much less than those of the first harmonic. However, as the rf magnetic field increases, the first harmonic is saturated much faster than the second harmonic [11].

The spectral structure of the lines of the first harmonic is more pronounced than in the static case. The Ω dependence of the first harmonic shows that the intensity of the spectral lines is maximal at a frequency of 2.3 MHz, which lies between the nuclear Larmor frequencies of the ground (1.7 MHz) and excited (3 MHz) states (see Fig. 2b). This behavior indicates the dominant role of quantum interference between the magnetic Rabi states of the isomer levels of the nucleus.

The sharp dependence of the shape of the first-harmonic line can be used to more accurately measure the spectral parameters. Figure 3 shows that the difference between the first-harmonic spectra when the constant magnetic field (H_1 = 150 kOe) changes by 2 and 5% is comparable to the intensity of the spectral lines. Moreover, the first harmonic spectra, as well as ultrasonic Doppler modulation, allow for precise measurement of the isomer shift [20].

This work shows that the accuracy of spectroscopic measurements can be improved by using additional time characteristics that arise when interference processes are induced. This improvement is expected to be

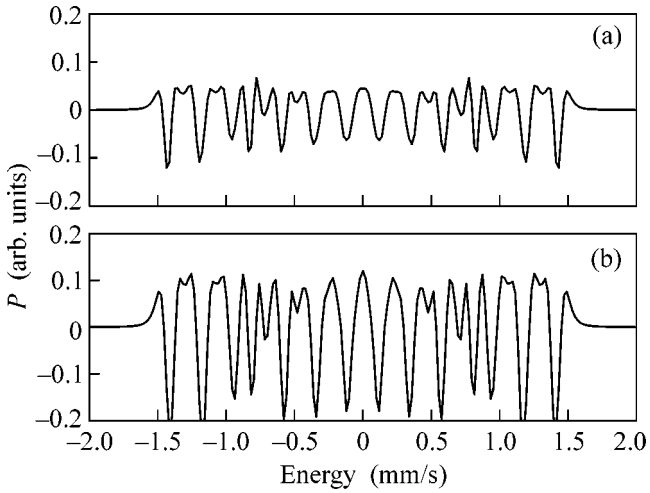

Fig. 3. Difference between the first harmonic spectra in the presence of a variable field H_1 = 150 Oe with frequency Ω = 3 MHz when the constant magnetic field H_0 = 3.4 kOe changes by (a) 2 and (b) 5%.

most pronounced for the ^{181}Ta nucleus, which is a promising isotope for developing gamma laser schemes [21].

This work was supported in part by the Russian Foundation for Basic Research (project no. 04-02-16939).

REFERENCES

1. A. H. Muir and F. Boem, Bull. Am. Phys. Soc. **4** (1959).
2. D. B. J. Salomon, PhD Thesis (1972), LBL-1276.
3. L. Kaindl, D. Salomon, and L. Wortmann, Preprint LBL-1631 (1973); Preprint LBL-1645 (1973).
4. E. F. Makarov and A. V. Mitin, Usp. Fiz. Nauk **120**, 55 (1976) [Sov. Phys. Usp. **19**, 741 (1976)].
5. A. V. Mitin, Izv. Ross. Akad. Nauk, Ser. Fiz. **62**, 395 (1998).
6. E. K. Sadykov, S. A. Alexeev, and L. L. Zakirov, in *Proceedings of First International Induced Gamma Emission Workshop, Predeal, Romania, 1997*, Ed. by I. I. Popescu and C. A. Ur (1999), p. 339.
7. A. V. Mitin, E. F. Makarov, and N. V. Polyakov, Zh. Éksp. Teor. Fiz. **90**, 1931 (1986) [Sov. Phys. JETP **63**, 1130 (1986)].
8. A. V. Mitin, Phys. Lett. **213**, 207 (1996).
9. A. V. Mitin, Opt. Spektrosk. **92**, 432 (2002) [Opt. Spectrosc. **92**, 389 (2002)].
10. A. V. Mitin, in *Proceedings of 5th International Conference on Mössbauer Spectroscopy, Bratislava, Czechoslovakia, 1973* (Praha, 1975), Part 3, p. 615.
11. A. V. Mitin, Phys. Lett. A **84**, 278 (1981).
12. L. J. Perlow, Phys. Rev. Lett. **40**, 896 (1978).
13. P. J. West and E. Matthias, Z. Phys. A **288**, 369 (1978).
14. E. Ikonen, P. Helistö, J. Hietaniemi, and T. Katila, Phys. Rev. Lett. **60**, 643 (1988).
15. M. Lippmaa, L. Tittonen, J. Linden, and T. Katila, Phys. Rev. B **52**, 10268 (1995).
16. V. K. Voĭtovetskiĭ, S. M. Cheremisin, A. Yu. Dudkin, and E. G. Ploskirev, Pis'ma Zh. Éksp. Teor. Fiz. **36**, 322 (1982) [JETP Lett. **36**, 393 (1982)].
17. L. T. Trammell and J. P. Hannon, Phys. Rev. **180**, 337 (1969).
18. V. K. Voitovetskii, S. H. Cheremisin, and S. B. Sazonov, Phys. Lett. A **83**, 81 (1981).
19. A. V. Mitin, Doctoral Dissertation in Mathematical Physics (Kazan, 1984).
20. J. E. Monahan and L. J. Perlow, Phys. Rev. A **20**, 1499 (1979).
21. A. V. Andreev, P. V. Volkov, V. M. Gordienko, *et al.*, Zh. Éksp. Teor. Fiz. **118**, 1343 (2000) [JETP **91**, 1163 (2000)].

Translated by R. Tyapaev

JETP Letters, Vol. 81, No. 9, 2005, pp. 427–431. Translated from Pis'ma v Zhurnal Éksperimental'noĭ i Teoreticheskoĭ Fiziki, Vol. 81, No. 9, 2005, pp. 541–545.

Neutron Diffraction at a Moving Grating as a Nonstationary Quantum Phenomenon

A. I. Frank[1], P. Geltenbort[2], G. V. Kulin[1], D. V. Kustov[1], V. G. Nosov[3], and A. N. Strepetov[3]

[1] *Frank Neutron Physics Laboratory, Joint Institute for Nuclear Research, Dubna, Moscow region, 141980 Russia*
e-mail: frank@nf.jinr.ru

[2] *Institute Laue Langevin, BP 156-38042 Grenoble Cedex 9, France*

[3] *Russian Research Centre Kurchatov Institute, pl. Akademika Kurchatova 1, Moscow, 123182 Russia*

Received April 4, 2005

The observation of the discrete energy spectrum in a new experiment on the diffraction of ultracold neutrons at a moving phase grating is reported. The results are in quantitative agreement with theoretical predictions and can be treated as additional evidence of the validity of the plane-wave representation of the initial neutron state.
© *2005 Pleiades Publishing, Inc.*

PACS numbers: 03.75.Be

Introduction. The diffraction of neutrons at diffraction gratings and other macroscopic objects has been repeatedly observed in experiments [1–11]. In addition to the demonstration of the validity of the basic predictions of quantum mechanics, these works promote the appearance of a new generation of neutron interferometers [12, 13]. More recently, it was shown that the well-known phenomenon of neutron diffraction can have surprising features in some cases. As was shown in [14], a grating moving across a beam of slow neutrons is a nonstationary quantum device that significantly changes the energy spectrum of neutrons incident on it. Ioffe [15] suggested the use of moving gratings in a neutron interferometer, which can considerably increase the sensitivity of the interferometer. The discrete spectrum arising when ultracold neutrons (UCNs) diffract at a moving grating was recently observed in an experiment reported in [16]. Soon after that, it was shown that the moving grating with a variable spatial period could serve as a quantum time lens for UCNs [17, 18]. In this paper, we report on the results of a new experiment on the diffraction of UCNs at the moving grating. This experiment already allows for quantitative comparison with theory.

Moving diffraction grating as a nonstationary quantum device. We briefly present the formulation and solution of the corresponding diffraction problem [14]. A plane wave $\Psi(z, t) = \exp[i(kz - \omega t)]$ is incident on a periodic structure—a diffraction grating that has the spatial period L, is situated in the XY plane, and moves along the Y axis with a velocity V. Solving the diffraction problem in the moving coordinate system where the grating is at rest, and passing then to the laboratory coordinate system, we obtain the wavefunction of the resulting state in the form

$$\Psi(z, y, t) = \sum_j a_j \exp[i(\sqrt{k^2 + 2k_V q_j - q_j^2}\, z + q_j y - (\omega + j\Omega)t)], \quad (1)$$

where

$$k_V = \frac{mV}{\hbar},\ \omega_V = \frac{mV^2}{2\hbar},\ q_j = \frac{2\pi}{L}j,\ \Omega = 2\pi T^{-1},$$
$$T = \frac{L}{V} \gg \omega^{-1},\quad a_j = \frac{1}{L}\int_0^L \theta(y)\exp(iq_j y)dy, \quad (2)$$

and $\theta(y)$ is a complex transmission function of one element of the grating. Diffraction leads to the appearance of the discrete spectrum

$$E_j = \hbar\omega_j,\quad \omega_j = \omega + j\Omega, \quad (3)$$

and the difference of the energy from the initial energy is attributed only to a change in the longitudinal z component of the wavenumber. Assuming that the spatial frequency of the grating is small, $L^{-1} \ll k$, and neglecting the third term in the radicand in Eq. (1), we obtain the following relation for the z components of the wave vectors:

$$\sqrt{k^2 + 2k_V q_j - q_j^2} \cong \sqrt{k^2 + \frac{2mV}{\hbar}q_j} = k\left(1 + j\frac{\Omega}{\omega}\right)^{1/2} = k_j. \quad (4)$$

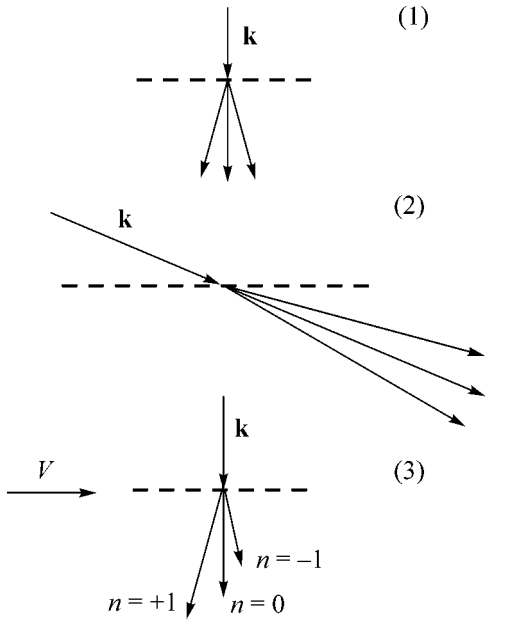

Fig. 1. Diffraction situations: (1) the immovable grating, (2) the coordinate system moving with the grating, and (3) the moving grating in the laboratory coordinate system.

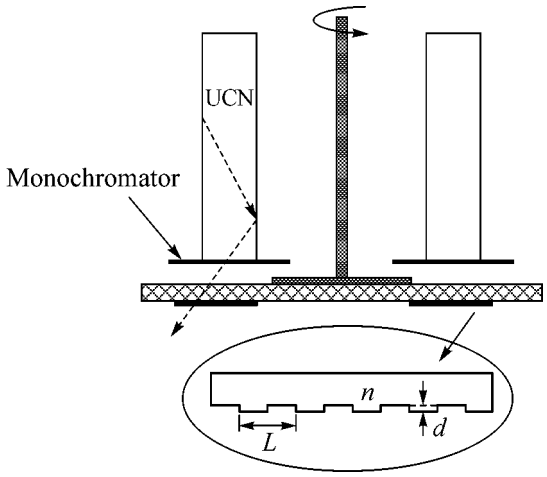

Fig. 2. Concept of the experiment. Neutrons pass through the rotating ring grating with radial grooves. The grating profile is shown in the lower panel.

Thus, for small diffraction angles,

$$\Psi(z, y, t) = \sum_j a_j \exp[i(k_j z + q_j y - \omega_j t)]. \quad (5)$$

Figure 1 illustrates the difference between the diffraction situations for the immovable and moving gratings.

Measurement of the neutron diffraction spectrum for the moving grating is carried out with the same spectrometer [19] as was used in the experiment reported in [16]. The basic spectrometric element of the instrument is a neutron interference filter (NIF) [9, 20–23], which is an analog of the Fabry–Perot interferometer. Figure 2 illustrates the concept of the experiment. Instead of a rectilinearly moving grating, we use a rotating grating prepared on the surface of a silicon disk 150 mm in diameter and 0.6 mm thick. On the periphery of a ring disk with an average diameter of 12 cm and width of 2 cm, radial grooves are made. The disk with the grating can be rotated about the vertical axis by a motor. Ultracold neutrons are incident on the grating, passing through a ring slit and an NIF monochromator. This monochromator passes neutrons with a narrow spectrum of vertical velocities ($\Delta v/v \approx 0.02$) with a maximum of 4.52 m/s, which corresponds to $E_z = m v_z^2/2 = 107$ neV. The angular period of the structure is equal to 3.325×10^{-4} rad. The width of a groove is equal to half the period. Owing to refraction in silicon, waves passing through different elements of the grating differ in phase. The corresponding phase difference is

$$\Delta\varphi = k(1-n)d, \quad (6)$$

where n is the index of refraction of silicon. The groove depth d was equal to 0.14 μm and is chosen such that the phase difference for 107-neV neutrons is $\Delta\varphi = \pi$. For the normal incidence of neutrons on the grating, the phase of the transmission function $\theta(y)$ changes stepwise by π over half the period. The Fourier coefficients corresponding to such a π modulation of the phase are

$$a_j = \frac{2}{i\pi \cdot j}, \quad j = 2s-1, \quad (7)$$

where s is an integer. We note that the line with the initial energy $\hbar\omega$ ($j = 0$) is absent in the resulting spectrum.

Neutrons that have passed through the grating enter a vertical mirror neutron guide. Moving downward along it, they are accelerated in the Earth's gravitational field, changing their energy by 1.025 neV per centimeter of the height. The second interference filter, serving as an analyzer, is placed in a special carriage inside the neutron guide. By varying the vertical position of the analyzer, one could scan the neutron spectrum by a comparatively narrow ($\Delta v/v \approx 0.02$) line of the analyzer. In order to compensate for the gravitational change in the UCN energy, the filter transmission maximum corresponds to an energy of 127 neV. Neutrons that have passed through the analyzer are detected by a detector. Strictly speaking, the spectrometer is sensitive to the vertical component of the wave vector rather than to the total energy of the neutron. However, this is a component that changes when the grating moves in the horizontal plane.

The count rate of the detector is measured as a function of the analyzer position. If the grating is at rest, the corresponding scanning curve is the convolution of the spectral functions of the monochromator $f(E)$ and ana-

lyzer $\eta(E)$. The scanning curve for the rotating grating has the form

$$F_2(\xi) = \sum_j |a_j|^2 F_1(\xi + j\hbar\Omega),$$
$$F_1(z) = \int f(E)\eta(E-z)dE, \quad (8)$$

where $\xi = mg\Delta H$, g is the gravitational acceleration, and ΔH is the distance between the filters.

Experimental results. Figure 3 shows the experimental scanning curves obtained for the grating rotation frequencies 7, 60, 80, and 99 Hz. These curves are approximated by the function

$$F_{\text{exp}}(\xi) = a + b\cdot\xi + A\sum_{j=-10}^{10} |a_j|^2 \exp\left[-\frac{(\xi - \xi_c - j\Delta)^2}{2\sigma^2}\right] \quad (9)$$

under the assumption that the scanning curve for the immovable grating is the sum of a linearly increasing background and a Gaussian with its center at ξ_c and a standard deviation σ.

The approximation functions are shown in Fig. 3 by solid lines. Figure 4 shows experimental data for the splitting parameter Δ. They lie on the straight line $\Delta = B\nu$, where ν is the grating rotation frequency. Comparing the slope $B_{\text{exp}} = (7.48 \pm 0.05) \times 10^{-2}$ cm s with the theoretical value $B_{\text{th}} = 4\pi^2\hbar(mg\alpha)^{-1} = 7.605 \times 10^{-2}$ cm s, where α is the angular period of the grating, we conclude that the experimental splitting of the spectrum agrees with the calculation within an accuracy of 2%. Small deviations can likely be attributed to methodical causes.

Fitting also provides estimates of the amplitudes A. Their values are given in Fig. 3. We emphasize that the scanning curve for a rotation frequency of 7 Hz must differ slightly from the curve for the immovable grating. On the contrary, this curve for a frequency of 99 Hz is the sum of only two Gaussians with the amplitudes $A|a_1|^2$, because the energy of neutrons corresponding to higher-order lines is beyond the measurement range. A comparison of the experimental A values for these two curves provides the degree of agreement between the amplitudes a_1 and their theoretical values. The relative intensity thus obtained for the first-order waves is $|a_1|^2_{\text{exp}} = 0.383(8)$. Calculation taking into account a weak edge effect caused by the oblique incidence of neutrons onto the moving grating [24] yields $|a_1|^2_{\text{th}} = 0.403$. The diffraction efficiency of the grating is five percent less than the theoretical estimate, because the grating profile is not ideal.

Widths of the energy peaks and the transverse coherence length of a free neutron. The above consideration was based on the commonly accepted plane-wave representation of the neutron wavefunction.

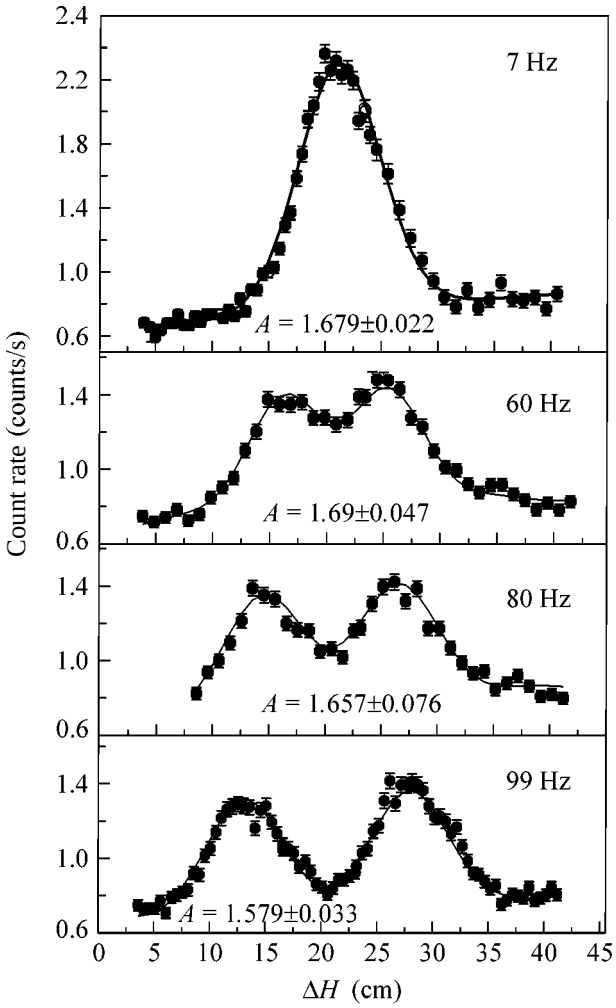

Fig. 3. Experimental scanning curves and corresponding approximation functions.

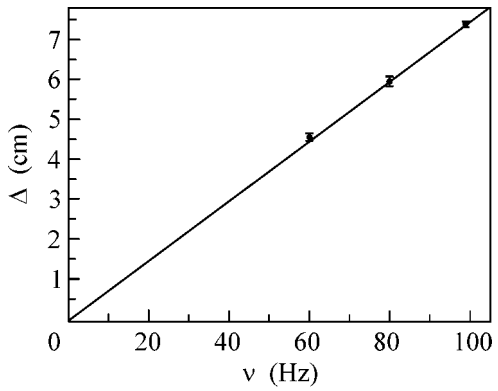

Fig. 4. Splitting parameter Δ vs. the grating rotation frequency.

Although any serious reason to doubt the validity of this representation is absent, its experimental verification is of interest. A finite transverse coherence length

of a neutron is likely possible only in nonlinear theory. The properties of the nonlinear Schrödinger equation have been studied in many works (see, e.g., [25, 26]), and certain predictions of nonlinear quantum theory have been verified in experiments [7, 27].

The assumption that the front of a wave incident on a grating is limited is equivalent to the concept of the limited linear dimension of the grating, and the corresponding problem is typical of diffraction theory (see, e.g., [28]). In this case, in each diffraction order j, the momentum transfer q_j, which is parallel to the grating plane, is characterized by a certain distribution function. Correspondingly, the energy spectrum from the moving grating is also smeared.

For definiteness, we consider the Gaussian distribution $p(y) = \exp(-y^2/2\zeta^2)$ for the wave-front intensity and take the width $l = 2\sqrt{2}\,\zeta$ of this distribution as the characteristic transverse coherence length. It is easy to show that the energy spectrum of the resulting state has the form

$$\Xi(E_z) = \frac{1}{\sqrt{\pi}\varepsilon}\sum_j |a_j|^2 \exp\left\{-\left[\frac{(E-E_n)^2}{2\varepsilon^2}\right]\right\}, \qquad (10)$$

where

$$\varepsilon = \frac{\hbar^2}{m}\frac{\sqrt{2}k_V}{\zeta}. \qquad (11)$$

This spectrum is the sum of the equidistant Gaussians with the relative intensity $|a_j|^2$ and standard deviation ε, which is proportional to the grating velocity. In view of the spectral measurements, we note that the spectrometer resolution function that has the standard deviation σ_0 is convolved now with spectrum (10) rather than with Dirac δ functions, and the standard deviation of this convolution is

$$\sigma = \sqrt{\sigma_0^2 + \varepsilon^2(V)}. \qquad (12)$$

Analysis of experimental data that is based on Eqs. (10)–(12) yields the estimate $\zeta > 2.5 \times 10^{-3}$ cm. Correspondingly, the transverse dimension of the coherent front is estimated as $l > 7 \times 10^{-3}$ cm.

Discussion and conclusions. Strictly speaking, the spectrometric experiment described above is not a diffraction experiment, because the initial width of the angular distribution of neutrons is several orders of magnitude larger than the diffraction angle. It is likely more correct to describe this experiment in terms of a periodic (phase in this case) modulation of the neutron wave rather than in terms of diffraction. This modulation occurs when a periodic structure moves rapidly across the wave propagation direction. In this case, the moving grating serves as a nonstationary quantum device similar to a quantum chopper or, more precisely, a modulator [29–34]. The analogy becomes more obvious if the spatial period L and grating velocity V in Eqs. (1), (2), and (5) for the wavefunction increase such that the modulation period $T = L/V$ remains constant. In the high velocity limit, Eq. (5) coincides with a formula describing a state formed by the modulator [33, 34].

The experimental data are in satisfactory agreement with the prediction of the theory based on the plane wave representation for the front of the initial wave. The minimum estimate, 7×10^{-3} cm, for the transverse coherence length is three orders of magnitude larger than the neutron wavelength.

We emphasize that the Gaussian shape of the spatial distribution of the initial-wave intensity was assumed only for simplicity and definiteness when calculating the transverse coherence length. A semiqualitative lower estimate obtained for it experimentally depends only slightly on the shape of the wave packet. At the same time, the Gaussian spatial distribution of the wavefunction of a particle (“Gausson”) appears in the model of nonlinear quantum mechanics with logarithmic inhomogeneity [25]. Experimental results were analyzed by the authors of [7] in order to verify this model. From their upper estimate for the nonlinear term in the Schrödinger equation, one can determine the minimum transverse size of the neutron Gausson. This model-dependent estimate is three times larger than the result of our work.

A considerably larger neutron coherence length, $l >$ 2 mm, was given in [9]. This result is also based on the absence of the broadening of the diffraction line. However, the estimate of those experimental data that is obtained by the above method taking Eq. (12) into account is comparable with our result in accuracy.

One of us (A.I.F.) is grateful to B.M. Bolotovskiĭ for stimulating discussions. This work was supported by INTAS, grant no. 00-00043.

REFERENCES

1. C. G. Shull, Phys. Rev. **179**, 752 (1969).
2. H. Kurz and H. Rauch, Z. Phys. **220**, 419 (1969).
3. H. Scheckenhofer and A. Steyerl, Phys. Rev. Lett. **39**, 1310 (1977).
4. A. G. Klein and G. I. Opat, Am. J. Phys. **45**, 295 (1977).
5. A. Graf, H. Rauch, and T. Ster, Atomkernenergie **33**, 298 (1979).
6. P. D. Kearney, A. G. Klein, G. I. Opat, and R. Gähler, Nature **287**, 313 (1980).
7. R. Gähler, A. G. Klein, and A. Zeilinger, Phys. Rev. A **23**, 1611 (1981).
8. A. G. Klein, P. D. Kearney, G. I. Opat, *et al.*, Phys. Rev. Lett. **46**, 959 (1981).
9. A. Steyerl, W. Drexel, S. S. Malik, and E. Gutsmiedl, Physica B (Amsterdam) **151**, 36 (1988).
10. A. Zeilinger, R. Gähler, C. G. Shull, and W. Mampe, Rev. Mod. Phys. **60**, 1067 (1988).
11. M. Tschernitz, R. Gähler, W. Mampe, *et al.*, Phys. Lett. A **164**, 365 (1992).

12. A. I. Ioffe, V. S. Zabiaykin, and G. M. Drabkin, Phys. Lett. A **111**, 373 (1985).
13. M. Gruber, K. Eder, A. Zeilinger, *et al.*, Phys. Lett. A **140**, 373 (1989).
14. A. I. Frank and V. G. Nosov, Phys. Lett. A **188**, 120 (1994).
15. A. I. Ioffe, in *Neutron Spin Echo Spectroscopy*, Ed. by F. Mezei, C. Pappas, and T. Gutbertlet (Springer, Berlin, 2003), p. 160.
16. A. I. Frank, S. N. Balashov, I. V. Bondarenko, *et al.*, Phys. Lett. A **311**, 6 (2003).
17. A. I. Frank, P. Geltenbort, G. V. Kulin, and A. N. Strepetov, Pis'ma Zh. Éksp. Teor. Fiz. **78**, 224 (2003) [JETP Lett. **78**, 188 (2003)].
18. S. N. Balashov, I. V. Bondarenko, A. I. Frank, *et al.*, Physica B (Amsterdam) **350**, 246 (2004).
19. I. V. Bondarenko, A. I. Frank, S. N. Balashov, *et al.*, Nucl. Instrum. Methods Phys. Res. A **440**, 591 (2000).
20. A. A. Seregin, Zh. Éksp. Teor. Fiz. **73**, 1634 (1977) [Sov. Phys. JETP **46**, 859 (1977)].
21. K.-A. Steinhauser, A. Steyerl, H. Schechenkofer, and S. S. Malik, Phys. Rev. Lett. **44**, 1306 (1980).
22. Yu. N. Pokotilovskiĭ, A. D. Stoĭka, and I. G. Shelkova, Prib. Tekh. Éksp., No. 1, 62 (1980).
23. I. V. Bondarenko, V. I. Bondarchuk, S. N. Balashov, *et al.*, Yad. Fiz. **62**, 775 (1999) [Phys. At. Nucl. **62**, 721 (1999)].
24. A. I. Frank, P. Geltenbort, G. V. Kulin, *et al.*, *Soobshch. Ob. Inst. Yad. Issled.* (Dubna), P3-2004-207 (2004).
25. I. Bialynicki-Birula and J. Mycielski, Ann. Phys. (N.Y.) **100**, 62 (1976); Phys. Scr. **20**, 539 (1979).
26. W. Lücke, in *Nonlinear, Deformed and Irreversible Quantum Systems*, Ed. by H.-D. Doebner, V. K. Dobrev, and P. Nattermann (World Sci., Singapore, 1995), p. 140.
27. C. G. Shull, D. K. Atwood, J. Arthur, and M. A. Horne, Phys. Rev. Lett. **44**, 765 (1980).
28. J. M. Cowley, *Diffraction Physics* (North-Holland, Amsterdam, 1975; Mir, Moscow, 1979).
29. M. Moshinsky, Phys. Rev. **88**, 625 (1952).
30. R. Gähler and R. Golub, Z. Phys. B **56**, 5 (1984).
31. J. Felber, R. Gähler, and R. Golub, Physica B (Amsterdam) **151**, 135 (1988).
32. J. Felber, G. Muller, R. Gähler, and R. Golub, Physica B (Amsterdam) **162**, 191 (1990).
33. V. G. Nosov and A. I. Frank, J. Mosc. Phys. Soc. **1**, 1 (1991).
34. A. I. Frank and V. G. Nosov, Yad. Fiz. **57**, 1029 (1994) [Phys. At. Nucl. **57**, 968 (1994)].

Translated by R. Tyapaev

JETP Letters, Vol. 81, No. 9, 2005, pp. 432–436. Translated from Pis'ma v Zhurnal Éksperimental'noĭ i Teoreticheskoĭ Fiziki, Vol. 81, No. 9, 2005, pp. 546–550.

Nucleon–Nucleon Correlations in the $(\gamma, \pi^- p)$ and $(\gamma, \pi^- pp)$ Reactions on the ^{12}C Nucleus

I. V. Glavanakov[1], Yu. F. Krechetov[1], O. K. Saĭgushkin[1], E. N. Shuvalov[1], and V. M. Bystritskiĭ[2]

[1] *Nuclear Physics Institute, Tomsk Polytechnic University, pr. Lenina 2a, Tomsk, 634050 Russia*
e-mail: krechet@npi.tpu.ru

[2] *Joint Institute for Nuclear Research, Dubna, Moscow region, 141980 Russia*

Received November 5, 2004; in final form, April 6, 2005

The photoproduction of negative pions on the carbon nucleus in the $(\gamma, \pi^- p)$ and $(\gamma, \pi^- pp)$ reactions has been studied experimentally. The measurements are interpreted using a model of the formation of an intermediate Δ nuclear state (Δ nucleus) that decays with the emission of a pion and a nucleon. © *2005 Pleiades Publishing, Inc.*

PACS numbers: 21.30.+y, 25.20.Lj

The $(e, e'p)$ reaction induced by high-energy electrons scattered on nuclei is a basic tool for studying the single-particle nuclear structure. The application of this reaction to analysis of nucleon–nucleon correlations appeared to be inefficient, because cross sections are small in a kinematic region where correlation effects are large, and it is difficult to identify reaction mechanisms associated with correlations of various natures.

In recent years, a more direct method has been widely used to acquire information on nucleon–nucleon correlations in nuclei. The existence of a correlated nucleon pair implies the possibility of the simultaneous knockout of both these nucleons. The study of nucleon–nucleon correlations in the $(e, e'pp)$ and $(e, e'np)$ reactions is promising, as was shown in a number of theoretical works (see references in [1]) and as was corroborated in experiments [2–4]. Nevertheless, further experimental investigations, including those with other particles initiating a reaction, are evidently necessary.

The $(\gamma, \pi N)$ reaction on nuclei for small energies and momenta transferred to the residual nucleus is similar in many respects to the $(e, e'p)$ reaction and is satisfactorily explained in the quasifree approximation. The most substantial feature of the $(\gamma, \pi N)$ reaction is a closer connection of pion photoproduction with nucleon resonances. Two experiments were carried out at the Tomsk synchrotron in order to analyze the cross section for the $(\gamma, \pi N)$ reaction on light nuclei in a kinematic region where manifestations of short-range nucleon–nucleon correlations could be expected. The cross section for the $(\gamma, \pi^0 p)$ reaction on a number of nuclei in the $\Delta(1232)$ region was measured in [5], and the cross section for the $^{12}C(\gamma, \pi^- p)$ reaction was measured in the second resonance region in a similar experiment [6]. The most interesting result of those works, which has not yet been finally interpreted, is the observation of a peak in the dependence of the reaction cross section on the proton emission angle in the region of large momentum transfers. This peak is absent in the experimental cross sections for the $(e, e'p)$ reaction.

In this work, in order to analyze the mechanism of pion–proton pair photoproduction for high momenta of the residual nucleus and to acquire information on nucleon–nucleon correlations in nuclei, we study the reactions

$$^{12}C(\gamma, \pi^- p), \quad (1)$$

$$^{12}C(\gamma, \pi^- pp) \quad (2)$$

in overlapping kinematic regions. The experiment was carried out in a bremsstrahlung beam from the Tomsk synchrotron at the maximum energy E_{max} = 500 MeV. The experimental setup included a channel for detecting a negative pion and two channels for detecting protons in coincidence with a pion in complanar geometry.

Pions with a mean momentum of 224 MeV/c were detected by a strongly focusing magnetic analyzer [7], which was placed at an angle of 76° with respect to the photon beam axis. The solid angle of the analyzer was equal to 3×10^{-3} sr, the momentum acceptance was equal to 24%, and the measurement accuracy for the pion momentum was ~1.4%.

Two proton channels are $(\Delta E, E)$ scintillation spectrometers. The first spectrometer detected protons in the energy range T_p = 30–140 MeV with an accuracy of 3–5 MeV. The angular acceptance was equal to 58°, the solid angle was equal to 0.16 sr, and the measurement accuracies for the polar and azimuth proton emission angles were equal to 2.5°–3° and 2°, respectively. The

methods for calibrating and monitoring the work of the first spectrometer are similar to those described in [8]. The second spectrometer was placed at an angle of 35° with respect to the photon beam axis in the half-plane of the pion channel and detected protons in the energy range 10–120 MeV. The solid angle of the second spectrometer was equal to 0.06 sr, and the polar and azimuth proton emission angles were measured with an accuracy of 2°.

The measured yield $d^4Y/dE_p d\Omega_p dE_\pi d\Omega_\pi$ of the $^{12}C(\gamma, \pi^- p)X$ reaction is related to the differential cross sections for the $^{12}C(\gamma, \pi^- p)^{11}C$ and $^{12}C(\gamma, \pi^- pp)^{10}B$ reactions by the respective relations

$$\frac{d^4Y}{dE_p d\Omega_p dE_\pi d\Omega_\pi} = \frac{d^3\sigma_{\pi p}(E_\gamma)}{dE_p d\Omega_p d\Omega_\pi} f(E_\gamma)\left|\frac{\partial E_\gamma}{\partial E_\pi}\right|,$$

$$\frac{d^4Y}{dE_p d\Omega_p dE_\pi d\Omega_\pi}$$

$$= \int dE_\gamma d\Omega_{p'} \frac{d^5\sigma_{\pi pp}(E_\gamma)}{dE_p d\Omega_p dE_\pi d\Omega_\pi d\Omega_{p'}} f(E_\gamma).$$

Here, E_γ and E_p are the photon energy and the total proton energy, respectively, and $f(E_\gamma)$ is the bremsstrahlung spectrum normalized as

$$\int f(E_\gamma) E_\gamma dE_\gamma = E_{\max}.$$

Figure 1a shows the differential yield of the $^{12}C(\gamma, \pi^- p)$ reaction as a function of the polar proton-emission angle θ_p. This yield is averaged over the range 60–140 MeV of the proton energy T_p. The dashed line in Fig. 1a is the theoretical yield of the $^{12}C(\gamma, \pi^- p)^{11}C$ reaction as calculated in the quasifree plane-wave approximation. In the kinematic region under consideration, as the polar proton-emission angle θ_p increases in the range 40°–140°, the mean momentum p_r of the residual ^{11}C nucleus in the ground state varies from 60 to 600 MeV/c. As is seen, when the angle θ_p increases to ~70° ($p_r \simeq 300$ MeV/c), the measured yield of the reaction decreases exponentially, in complete agreement with the calculation. However, with a further increase in θ_p, the behavior of the differential yield changes abruptly and a minimum is formed. The same qualitative angular dependence of the cross section was obtained in [5, 6]. A mechanism of formation of pion–proton pairs may be common for reactions on various nuclei and different energy ranges. It is natural to assume that an additional channel of the photoproduction of pions opens and that the residual nucleus disintegrates in this channel, such that two nucleons are free.

The substantial properties of the differential cross section for multiparticle nuclear reactions are satisfactorily reproduced by phase-space models (see, e.g., [9, 10]). The simplest model, which is shown by the dotted line in Fig. 1a and in which the amplitude of the

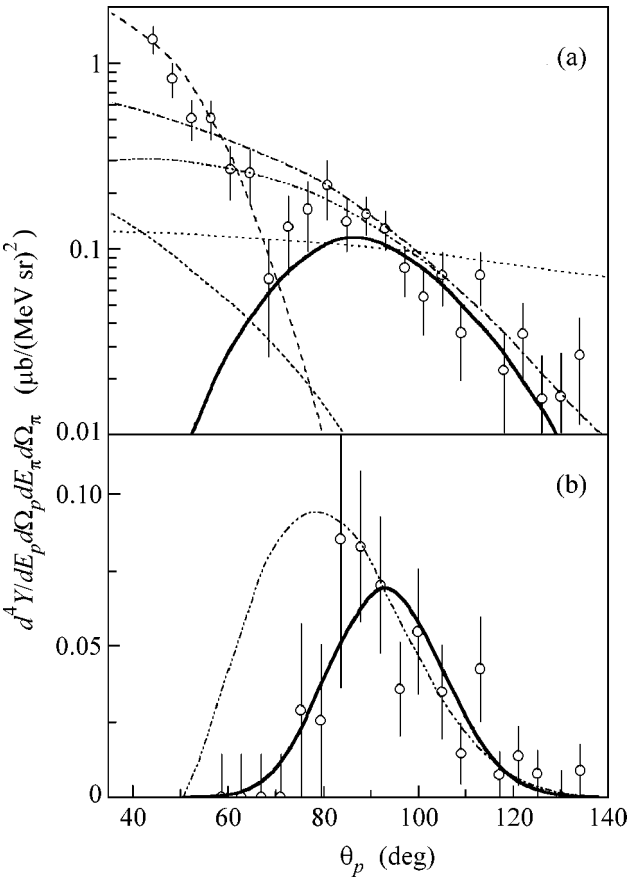

Fig. 1. Differential yield of the $^{12}C(\gamma, \pi^- p)$ reaction vs. the polar proton-emission angle for (a) $T_p > 60$ MeV and (b) $T_p > 60$ MeV and $p_p^* > 260$ MeV/c. Experimental points are obtained in this work, the dashed line is the quasifree yield of the $^{12}C(\gamma, \pi^- p)^{11}C$ reaction, the dotted line is the phase-space yield of the $^{12}C(\gamma, \pi^- pp)$ reaction, the short dashed line corresponds to the mechanism shown in Fig. 2b, the dash–dotted line with one (two) point corresponds to the mechanism shown in Fig. 2c excluding (including) the blocking of final states due to the Pauli exclusion principle, and the solid line corresponds to the mechanism shown in Fig. 2d.

$^{12}C(\gamma, \pi^- pp)$ reaction is constant over the entire range of its definition, cannot reproduce the angular dependence of the cross section. The diagram shown in Fig. 2a illustrates an apparently dominant reaction mechanism where a pion is produced due to the interaction of a photon with the neutron of a correlated *np* pair. The feature of this pion-production mechanism is a low momentum $\mathbf{p}_B$ of the residual ^{10}B nucleus and, therefore, a low total momentum $\mathbf{p}_{np} = -\mathbf{p}_B$ of the *np* pair.

In view of nucleon–nucleon correlations, another important quantity that characterizes the reaction mechanism is the relative momentum $\mathbf{p}_{\text{rel}} = (\mathbf{p}_2 - \mathbf{p}_n)/2$ of the particles in the *np* pair before interaction. Short-range correlations most strongly distort the wavefunc-

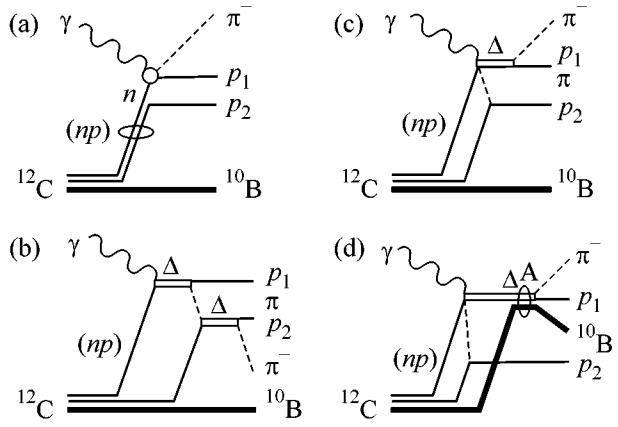

Fig. 2. Diagrams illustrating mechanisms of the $^{12}C(\gamma, \pi^- pp)^{10}B$ reaction.

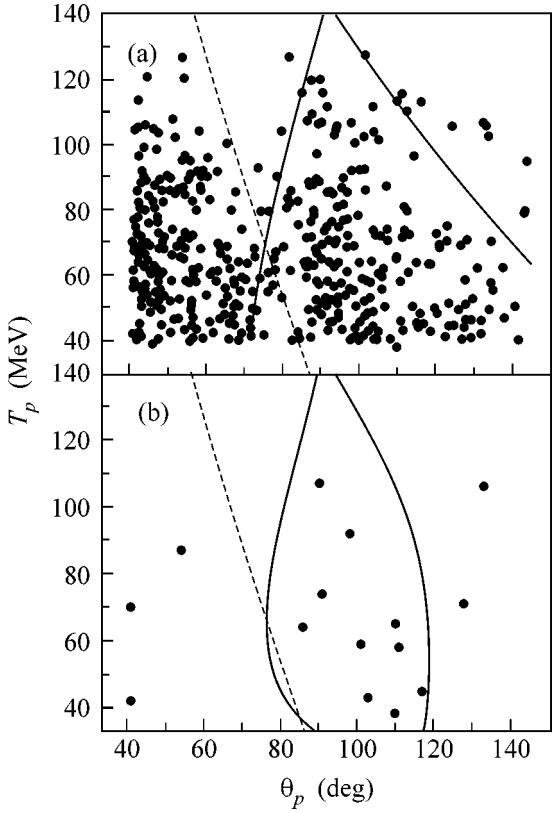

Fig. 3. Distribution of events over the polar emission angle θ_p of the proton and its energy T_p for the (a) $^{12}C(\gamma, \pi^- p)$ and (b) $^{12}C(\gamma, \pi^- pp)$ reactions.

tion of the relative motion of a pair of nucleons in the distance range corresponding to Fourier components with momenta exceeding ~400 MeV/*c*. Hence, the effect of correlations can be expected in a kinematic region where the momentum $\mathbf{p}_{\rm rel}$ is higher than this estimate.

The distribution of detected events over the kinetic energy T_p and the polar angle θ_p of the emission of the first proton is shown in Figs. 3a and 3b for reactions (1) and (2), respectively. The dashed line in Fig. 3a bounds the region of small θ_p angles, beyond which the differential yield of the quasifree production of pions is no more than 0.01 μb/(MeV sr)^2. For the available statistics, the probability of the $^{12}C(\gamma, \pi^- p)^{11}C$ reaction event to the right of this line is very low. The solid line in Fig. 3a is the boundary of the region where the momentum $\mathbf{p}_{np}$ of a correlated *np* pair is no more than the Fermi momentum and the relative momentum $\mathbf{p}_{\rm rel}$ is higher than 450 MeV/*c*. Similar boundaries in Fig. 3b are calculated with the additional inclusion of the acceptance of the second proton spectrometer. According to Fig. 3, for energies T_p higher than 80 MeV, bounded kinematic regions, as well as detected events, are almost completely separated. This separation indicates that events correspond to different mechanisms of the production of pions and corroborates the assumption that the $^{12}C(\gamma, \pi^- p)$ reaction events in Fig. 3a in the region of large proton-emission angles are attributable primarily to the two-nucleon knockout mechanism.

The kinematic region separated in Fig. 3 by the solid line is traditionally associated with nucleon–nucleon correlations in the nuclear ground state. Since mechanisms of the manifestation of short-range correlations in the reactions of quasifree electron scattering and pion photoproduction are similar to each other, their possible contribution to the $^{12}C(\gamma, \pi^- p)^{11}B$ reaction for large proton-emission angles must be two or three orders of magnitude less than that in the quasifree peak, which is much less than the measured value. The ratio of the cross sections measured for reactions with one and two protons also differs from the value expected on the basis of electron scattering data [11, 12]. This difference is explained by the difference between similar mechanisms of two-nucleon knockout for the pion photoproduction that are associated with two-particle exchange meson and isobar currents. The second cause of this difference is the contribution of additional mechanisms of the reaction that are associated with the specificity of particles involved in the reaction. One such mechanism is shown in Fig. 2b, where nucleon–nucleon correlation is attributed to the final state interaction, the propagation of a Δ isobar in the nucleus. The relative momenta $p_{\rm rel}^{(a)}$ and $p_{\rm rel}^{(b)}$ for the diagrams shown in Figs. 2a and 2b are related to each other as $\mathbf{p}_{\rm rel}^{(b)} = \mathbf{p}_{\rm rel}^{(a)} - 2\mathbf{q}$, where $\mathbf{q}$ is the momentum transfer in the pion rescattering. In the angular range $\theta_p = 40°$–$70°$, the mean value of the relative momentum $\mathbf{p}_{\rm rel}^{(b)}$ varies from 100 to 200 MeV/*c*, which does not contradict the independent-particle oscillator shell model. The yield of the

^{12}C (γ, $\pi^- pp$) reaction calculated by this model is shown by the short dashed line in Fig. 1a. The reaction amplitude included the wavefunction of the nucleon pair in the momentum representation and takes into account the mass distribution of the Δ isobar. The normalization was performed using the data on the ^{12}C (γ, $\pi^+ p$) reaction [8, 13], whose yield for low momenta of the residual nucleus is attributed to the final-state rescattering. As is seen, according to this model, the reaction yield is concentrated primarily in the range of small θ_p angles. Two-proton events in Fig. 3b to the left of the dashed line bounding the region of the quasi-free production of $\pi^- p$ pairs are possibly attributable to rescattering. However, it is impossible to explain the measurement data for large proton emission angles in the framework of this model.

The reaction mechanism that is represented by the diagram in Fig. 2c and in which two pions are formed, one of which is absorbed with the emission of a proton, was previously used in [14] to explain data on the photoproduction of single pions on the deuteron. The angular dependence of the yield according to this model is shown by the dashed–dotted line in Fig. 1a. The reaction amplitude is constructed similarly to the preceding model. The calculated yield well reproduces experimental data for large proton emission angles but overestimates the contribution of the two-nucleon reaction in the region of the quasi-free peak of the yield and does not reproduce the minimum in the angular dependence.

The yield minimum near $\theta_p \simeq 70°$ may result from the suppression of the reaction at small angles between the pion and proton scattering directions. If a detected pion–proton pair is a product of the decay of a Δ isobar, the strong angular correlation of the yield can be explained by mechanisms of the suppression of the formation of the isobar with a low mass or high momentum. One of possible suppression mechanisms is associated with the blocking of final states by the Pauli exclusion principle. The calculation that includes this factor and is shown by the dashed–double-dotted line in Fig. 1a does not significantly improve the agreement.

Another interpretation of the data is associated with the reaction mechanism represented by the diagram shown in Fig. 2d. Before the discussion of this model, we note that the second maximum in the reaction yield is observed for pion–proton scattering angles close to 180°. This maximum is located in the region where the total momentum of the pion–proton pair is minimal. Another remarkable feature of the reaction mechanism with the production of two pions is that a nucleon formed after the absorption of the pion can get a considerable part of the photon momentum. As a result, the Δ isobar is formed at rest with respect to the residual nucleus and is captured by the nucleus, with the formation of a short-lived bound state decaying with the emission of a pion and a proton.

The possibility of existing bound ΔN- and Δ-nuclear states was widely discussed in the 1970s [15–17]. Some works were stimulated by the results of the experiment in [18], where the ^{4}He(γ, $\pi^- p$) reaction was studied. Experimental data obtained in [18] for a residual-nucleus momentum of 200 MeV/c could not be explained in the quasi-free approximation. The theoretical estimates of the possibility of such states existing are contradictory [16, 17]. Since that time, conclusive experimental evidence of the existence or absence of such states has not been obtained. Our next model is based on the assumption that such states exist. The solid line in Fig. 1a is the calculation in the model represented by the diagram shown in Fig. 2d. The reaction amplitude includes, in addition to the wavefunction of the neutron–proton pair, the momentum wavefunction of the Δ isobar bound in the nucleus. We suppose that baryons bounded in the nucleus cannot significantly change the spatial state over the isobar lifetime. For this reason, we take the nucleon oscillatory wavefunction for the ^{12}C nucleus as the radial wavefunction of the isobar. As is seen, the model of the reaction proceeding through an intermediate Δ nuclear bound state well reproduces the angular dependence of the yield. Since the isobar momentum depends on the opening angle between the pion and proton, the angular dependence of the reaction yield presents the momentum distribution of the isobar in the nucleus with a maximum at an opening angle close to 180°, where the isobar momentum is minimal.

Figure 1b shows the angular dependence of the yield for events in which the proton momentum in the c.m.s. of the pion–proton pair exceeds 260 MeV/c. This is the region of the high-energy slope of the isobar mass distribution. As is seen, in complete agreement with the proposed model, the angular distribution narrows and its center of gravity is shifted towards larger θ_p angles. In this kinematic region, the energy of both protons from the ^{12}C(γ, $\pi^- pp$) reaction is sufficiently high. Hence, the blocking of final states by the Pauli exclusion principle is inefficient. Angular-distribution narrowing that differs from the prediction of the model described by the diagram in Fig. 2c is attributed to the suppression of the formation of the isobar with a high momentum due to the dynamics of the isobar in the nucleus. Such behavior of the angular distribution of the reaction yield is additional evidence of the adequacy of the model with the intermediate Δ-nuclear bound state.

The basic results of this work are as follows. The ^{12}C(γ, $\pi^- pp$) and ^{12}C(γ, $\pi^- p$) reactions have been experimentally studied. The irregularity in the angular dependence of the differential yield of pion–proton pairs for large proton-emission angles has been explained. This irregularity is attributed to reaction channels where the residual nucleus has disintegrated. Analysis of the data provides evidence of the existence of a Δ-nuclear bound state (Δ nucleus) that decays with the emission of a pion and a nucleon.

We are grateful to the staff of the Tomsk synchrotron for ensuring the required operation regime. This work was supported by the Russian Foundation for Basic Research (project no. 02-02-17866).

REFERENCES

1. D. N. Kadrev, M. V. Ivanov, A. N. Antonov, *et al.*, Phys. Rev. C **68**, 014617 (2003).
2. R. Starink *et al.*, Phys. Lett. B **474**, 33 (2000).
3. G. Rosken, in *Proceedings of Conference on Pespectives in Hadronic Physics* (World Sci., Singapore, 1998), p. 185; Prog. Part. Nucl. Phys. **44**, 99 (2000).
4. A. Niyazov and L. B. Wainstein (for the CLAS Collab., BAIONS 2002), in *Proceedings of the 9th International Conference on the Structure of Barions*, Ed. by C. E. Carlson and B. A. Mecking (World Sci., Singapore, 2003), p. 581.
5. V. N. Eponeshnikov and Yu. F. Krechetov, Pis'ma Zh. Éksp. Teor. Fiz. **29**, 442 (1979) [JETP Lett. **29**, 401 (1979)].
6. I. V. Glavanakov, Yu. F. Krechetov, A. V. Moiseenko, *et al.*, Yad. Fiz. **61**, 2175 (1998) [Phys. At. Nucl. **61**, 2064 (1998)].
7. S. V. Kolmogorova, Yu. F. Krechetov, and G. A. Saruev, Izv. Vyssh. Uchebn. Zaved., Fiz., No. 340-83, 9C (1983).
8. V. M. Bystritsky, A. I. Fix, I. V. Glavanakov, *et al.*, Nucl. Phys. A **705**, 55 (2003).
9. P. S. Anan'in, I. V. Glavanakov, and M. N. Gushtan, Izv. Vyssh. Uchebn. Zaved., Fiz. **9**, 51 (1989).
10. I. V. Glavanakov, Phys. At. Nucl. **63**, 2091 (2000).
11. K. G. Fissum *et al.*, Phys. Rev. C **70**, 034606 (2004).
12. J. Ryckebusch *et al.*, Nucl. Phys. A **624**, 581 (1997).
13. M. Liang, D. Branford, T. Davinson, *et al.*, Phys. Lett. B **411**, 244 (1997).
14. J. M. Laget, Phys. Rev. Lett. **41**, 89 (1978).
15. J. M. Laget, Preprint CEN Saclay, DPHN/HE (1973).
16. H. Arenhovel, Nucl. Phys. A **247**, 473 (1975).
17. V. B. Belyaev, K. Moller, and Y. A. Simonov, J. Phys. G **5**, 1057 (1979).
18. P. E. Argan, G. Audit, N. D. Botton, *et al.*, Phys. Rev. Lett. **29**, 1191 (1972).

Translated by R. Tyapaev

JETP Letters, Vol. 81, No. 9, 2005, pp. 437–441. Translated from Pis'ma v Zhurnal Éksperimental'noĭ i Teoreticheskoĭ Fiziki, Vol. 81, No. 9, 2005, pp. 551–555.

On the Mechanism of Noncoalescence in a Droplet Cluster

A. A. Fedorets

Tyumen State University, Tyumen, 625003 Russia
e-mail: fedorets_alex@utmn.ru

Received December 13, 2004; in final form, March 9, 2005

Experimental data are presented, from which it follows that the mechanism of noncoalescence in a cluster of drops is not attributable to the electrostatic charging and the presence of surfactants. The Stokes force acting upon drops of the cluster in a convective plume amounts to a fraction of a percent of the drop weight. New effects are described, which provide evidence for a fast proper rotation of drops in the cluster. Estimates show that this rotation is explained in terms of the hypothesis of a thermocapillary nature of the noncoalescence phenomenon. © *2005 Pleiades Publishing, Inc.*

PACS numbers: 44.25.+f, 47.55.Dz

Although investigations into droplet clusters [1, 2] are only just beginning, several directions can already be outlined in which the results are especially important and expected with considerable interest from the standpoint of both basic science and applications. First, each drop in such a cluster is a dissipative structure of a new type, and the whole cluster can be considered as a dissipative superstructure.[1] Second, the phenomena in droplet clusters provide a basis for the development of new methods for highly precise dosing of liquids [3] and imaging flows in liquids and gases [4]. Third, the processes in droplet clusters must be taken into consideration in solving some thermophysical, physicochemical, and other problems. Fourth, there is an interesting analogy: drops in a cluster, like atoms in a crystal, are arranged at a certain distance from each other, and a tendency to attraction arises when this distance increases, and to repulsion when it decreases. This behavior suggests that droplet clusters can be considered as model systems analogous to Bragg bubble crystals [5]. Successful developments in any of the above directions are impossible without a correct understanding of the nature of the observed phenomena, in particular, of the mechanism of noncoalescence of drops in a cluster.

The results presented below were obtained using an experimental setup analogous to that described previously [1], except that the clusters were induced in this study with the aid of a heating element embedded in the cuvette bottom (Fig. 1). Modification of the cuvette design was aimed at providing more convenient conditions for the microscopic examination of a droplet cluster. This was achieved by minimizing the amplitude of horizontal movements of the cluster and by decreasing the intensity of evaporation of the liquid layer. However, a rather unexpected consequence of this modification of the cuvette design was a qualitative change in the structure of a convective plume, namely, a toroidal vortex appeared around the heating element (Fig. 1). Experiments with the modified cuvette revealed new effects, which seem to offer a key to the uncovery of the mechanism of noncoalescence in a droplet cluster.

Theoretically, the stability of a droplet cluster with respect to coalescence can be related to several factors,

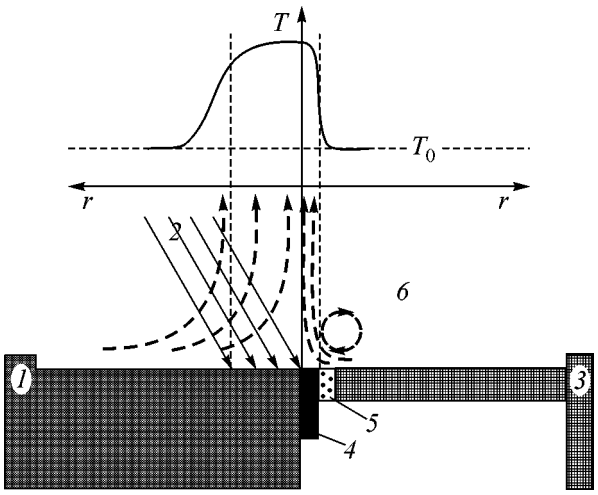

Fig. 1. Schematic diagrams showing the design and comparative characteristics of the (left side) original and (right side) modified experimental cuvettes (the solid curve T is the temperature profile; dashed arrows indicate the convective plume structure): (*1*) ebonite cuvette case; (*2*) beam of white light heating a 8×10-mm region on the substrate surface [1]; (*3*) duralumin cuvette case; (*4*) built-in heating element (nichrome wire wound on a copper rod 1 mm in diameter); (*5*) Teflon thermal insulation sleeve; (*6*) toroidal vortex.

[1] Drops are also stable outside the cluster, but a highly ordered cluster structure is an important manifestation of complicated interactions in such a system of drops.

0021-3640/05/8109-0437$26.00 © 2005 Pleiades Publishing, Inc.

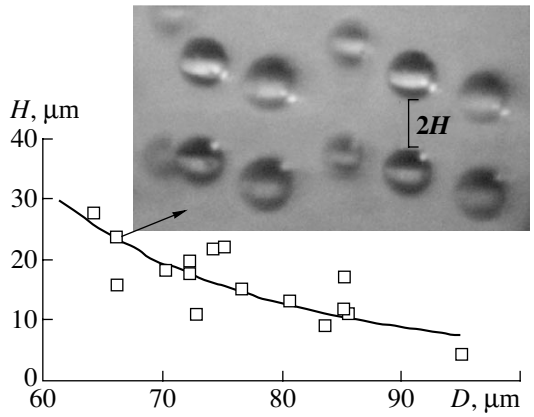

Fig. 2. Distance from the drop to the liquid surface versus the drop diameter. Data obtained from video images of the clusters monitored in the course of slow (quasi-stationary) heating of the water layer leading to the growth of droplet clusters.

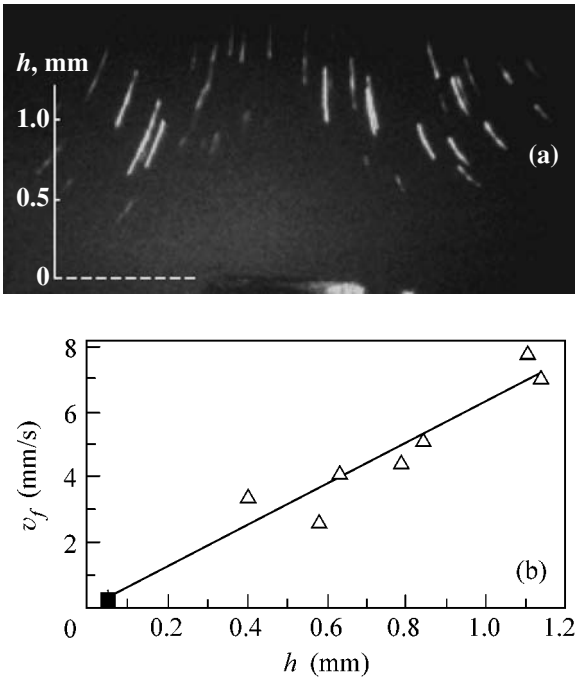

Fig. 3. (a) A photograph (exposure 1/20 s) showing the structure of flows in the convective plume imaged with the aid of a laser beam. (b) A plot summarizing the results of measurements of the flow velocity in the convective plume.

including (i) electrostatic charges, (ii) surfactants, (iii) aerodynamic effects due to flows in the convective plume, and (iv) thermocapillary flows in the drops [1]. This study was based on simple experiments that provided clear, unambiguously interpretable qualitative results. The calculations were only intended to estimate the effects by order of magnitude.

Electrostatic mechanism. The assumption concerning the possible charging of drops and a liquid pool surface was one of the first checked. For this purpose, clusters were induced above the surface of an electroconducting liquid (water) contained in a grounded all-metal cuvette. It was established that grounding did not influence the cluster. For this reason, the electrostatic mechanism of noncoalescence was already rejected in [1].

Surfactants. The question of the possible role of surfactants in the mechanism of noncoalescence was also posed in [1], but then it did not receive an unambiguous answer. The new data show evidence that surfactants cannot account for the noncoalescence. Indeed, the video images[2] of clusters observed using a microscope positioned in the horizontal plane clearly indicate (due to a mirror surface of the liquid) that the distance (H) from the bottom surface of the drop to the top surface of the liquid layer was comparable with the drop diameter (D) (Fig. 2). Therefore, the distance H is several orders of magnitude greater than the radius of action of intermolecular forces.

Stokes mechanism. As is known [1], the stability of a droplet cluster with respect to coalescence is directly determined by the convective plume. A drop entering into the typical cluster (Fig. 2: water, $R = 40$ μm; $\rho = 10^3$ kg/m^3) has a weight of

$$F_g = \frac{4}{3}\pi R^3 \rho g = 2.7 \times 10^{-9} \text{ N}. \quad (1)$$

This weight must be equilibrated by the counteracting Stokes force[3]

$$F_S = 6\pi\mu_g R v_f, \quad (2)$$

where μ_g and v_f are the dynamic viscosity and velocity, respectively, of a wet airflow streamlining the drop ($\mu_g \simeq 18.5 \times 10^{-6}$ Pa s) [6]. Upon substituting drop weight (1) into formula (2), we conclude that equilibrium is possible at $v_f = 190$ mm/s. Then, the question arises: what is the real plume flow velocity in the region of cluster localization?

Estimates can be based on several complementary sources of data:

(i) vapor flow velocity (measurements of the time required for the evaporation of a known volume of liquid showed that the vapor flow velocity in our experiments could not exceed 0.25 mm/s even under the

[2] One such image is presented in Fig. 2.

[3] Strictly specking, the drop weight has to be compared to the vertical component of the Stokes force. However, on the level of rough estimates (by order of magnitude) we can restrict our consideration to a simply measured characteristic such as the absolute flow velocity.

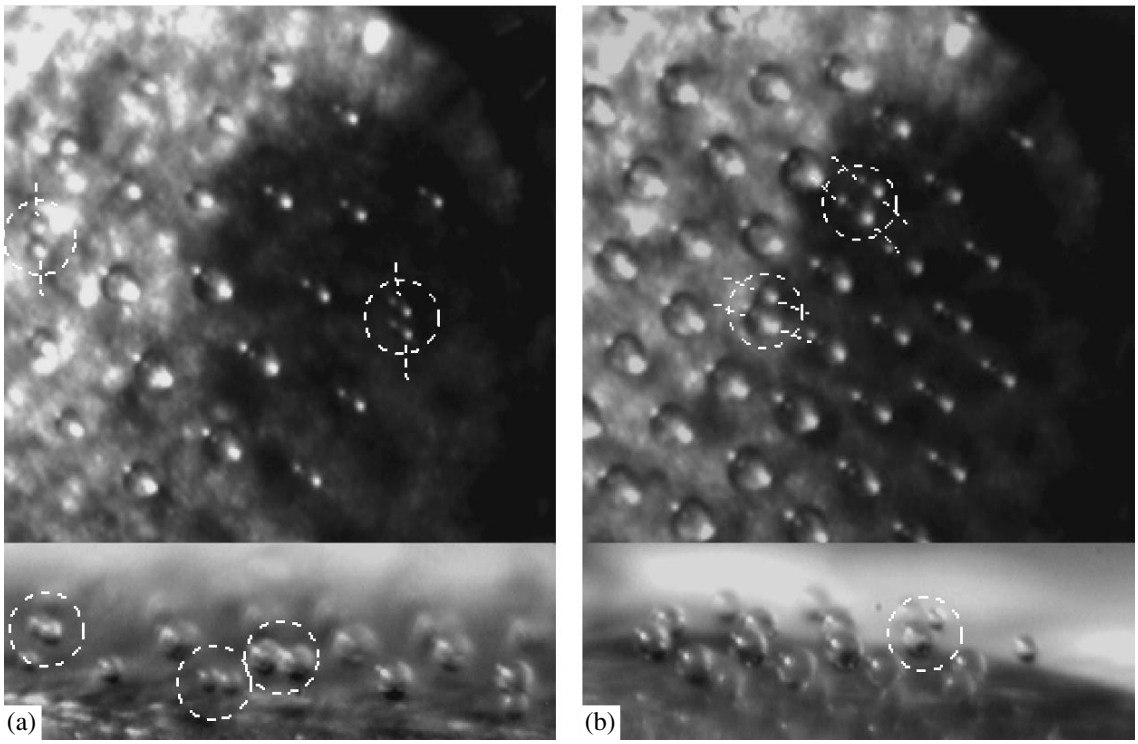

Fig. 4. Photographs of the tandem effects of the (a) first and (b) second kinds imaged with a microscope in the vertical and nearly horizontal positions. Envelopes indicate the drop tandems, and dashed lines show the axes of rotation.

favorable condition that evaporation proceeded only from the surface of the heating element);

(ii) horizontal motions of individual drops (their velocity reached 0.3 mm/s);

(iii) images of the convective plume velocity field (Fig. 3a).

A clear correlation between the data of independent v_f determinations (Fig. 3b) unambiguously indicates that the real velocity of airflows streamlining the cluster does not exceed 1 mm/s. In this case, the Stokes force amounts to a fraction of percent of drop weight (1).

More important evidence against the assumption of a predominating role of the Stokes mechanism of the noncoalescence is a clearly manifested "attachment" of the cluster to the liquid layer surface, which would be difficult to explain in the presence of a vertical gradient of the plume flow velocity. Indeed, if this were the case, a drop displaced upward (for any reason) would occur under the action of a Stokes force by far exceeding the drop weight. Such a drop must be unavoidably carried away by the convective plume.

Thermocapillary mechanism. Previously, a hypothesis was formulated [1] according to which drops in a cluster feature intense thermocapillary flows. These flows create individual protective shells of entrained gas around the drops. The thermocapillary mechanism of noncoalescence is well known in the case of relatively large drops of nonvolatile liquids [7, 8], but it is unclear whether it can be realized in microdrops of the clusters under consideration.

An answer to this question could be provided by observations of the internal liquid flows, but the very small dimensions of the drops studied (which were comparable with or smaller than the particles traditionally used for the flow imaging) and the impossibility of introducing imaging particles into the drops make such experiments extremely difficult.

Under such conditions, a breakthrough was provided by experiments with a modified cuvette, which revealed new (previously unobserved) phenomena manifested by tandem effects of the first and second kinds. A tandem effect of the first kind consists in that rotating drops approach each other in the toroidal vortex and combine to form tandems. Occurring in a cluster, such a tandem occupies a position in which the axis of rotation of the drops is perpendicular to centrifugal flows in the convective plume (Fig. 4a). The tandem lives for 10–12 s and then separates into two independent drops. A tandem effect of the second kind is observed when a drop ejected by the toroidal vortex "saddles" another drop in the cluster (Fig. 4b). Such tandems usually come into motion, whereby the "rider" drop is always shifted in the direction opposite to the direction of motion. The lifetime of a tandem of the second kind also does not exceed several seconds.

The tandem effects play a key role in solving the problem of noncoalescence, since their presence is evi-

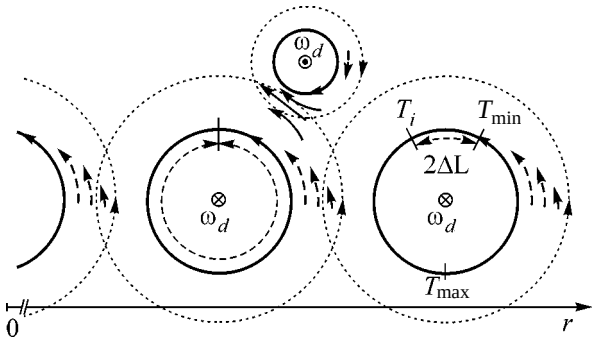

Fig. 5. Schematic diagram illustrating the kinematics of a droplet cluster and the development of thermocapillary forces (see text for explanation). Dotted circles indicate the shells of gas entrained by drops rotating with the angular velocity ω_d.

dence of a fast proper rotation of drops about radial perpendicular horizontal axes (Fig. 4). Taking into account conclusions (following from the Bernoulli equation) concerning the position and the direction of rotation (determined by the toroidal vortex, Fig. 1) of a "rider" drop in the tandem, it is possible to determine the direction of rotation of drops in the cluster (Fig. 5).

Let us try to explain the rotation of drops in a cluster in terms of the thermocapillary mechanism. Assuming that the temperature monotonically varies over the drop surface from maximum ($T_{\max}$) to minimum ($T_{\min}$) and taking into account the geometry of the convective plume, we can expect that the position of the point of minimum temperature will be shifted by a certain distance ΔL relative to the vertical axis of the drop (Fig. 5), while the point of maximum temperature occurs in the region where the drop surface is closest to the layer. Now, we can readily estimate the order of magnitude of the thermocapillary forces (F_{TC}) caused by this temperature distribution. Consider a point T_i spaced by ΔL from the vertical axis of the drop in the direction opposite to the direction toward $T_{\min}$ (Fig. 5). The temperature of the drop surface at this point falls in the interval $T_{\max} > T_i > T_{\min}$, and the resulting thermocapillary force is

$$\begin{aligned} F_{\mathrm{TC}} &= \sigma'_T(L-\Delta L)((T_{\max}-T_{\min})-(T_{\max}-T_i)) \\ &= \sigma' T(L-\Delta L)(T_i-T_{\min}), \end{aligned} \quad (3)$$

where σ'_T is the temperature coefficient of surface tension (for water, $\sigma'_T = 0.145$ mN/(m K) [9]) and L is the length of a circle with radius R.

Assuming that the difference $T_i - T_{\min}$ does not exceed 0.01 K and that $\Delta L = 0.1L$, we obtain, for the typical cluster ($R = 40$ μm), $F_{\mathrm{TC}} = 3.3 \times 10^{-10}$ N. This force is capable of imparting to the drop the angular acceleration[4]

$$\varepsilon_d = \frac{5}{2}\frac{F_{\mathrm{TC}}}{mR} = 7.6 \times 10^4 \text{ rad/s}^2. \quad (4)$$

A more difficult task is to calculate the angular velocity ω_d of the stationary rotation of the drop, since this would require a mathematical model taking into account processes both in the drops and in the surrounding gaseous medium. However, a threshold (but by no means limiting) ω_d value can be estimated from the following considerations. A half-period of the drop rotation (τ_d) must not exceed the characteristic time (τ_a) for the relaxation of temperature inhomogeneities by means of conductive heat transfer:

$$\tau_a \sim R^2/a. \quad (5)$$

For a typical water drop ($R = 40$ μm; thermal diffusivity, 1.615×10^{-7} m^2/s [10]), τ_d amounts to 10 ms, which corresponds to $\omega_d \sim 3.1 \times 10^2$ rad/s and a linear velocity of the drop surface (v_d) on the order of 12.6 mm/s. According to formula (4), this threshold velocity can be reached within 4 ms, which implies that the temperature fluctuation on the drop surface will unavoidably set it in motion.

The proper rotation of drops explains some apparently contradictory properties of droplet clusters, such as their "attachment" to the liquid layer surface observed simultaneously with stability with respect to coalescence. According to the Bernoulli equation, the proper rotation of drops creates a region of decreased pressure beneath, whereas the condition of sticking to the drop surface accounts for the conservation of a gaseous boundary layer preventing the drops from coalescence.

Progress in the development of methods for the imaging of clusters and image processing gives us hopes that the accuracy of measurements will soon increase to the level necessary for the direct observation of the drop rotation as manifested in the structure of clusters and, probably, in their deformation. Apparently, investigations into the statistically reliable structural features of droplet clusters may provide one of the main sources of experimental data necessary to confirm or reject the hypothesis concerning the thermocapillary mechanism of noncoalescence of a droplet cluster.

In conclusion, it should be noted that the thermocapillary hypothesis of noncoalescence might admit intriguing extrapolations. In particular, the drops in aerosols under certain conditions can be also expected to exhibit proper rotations of a thermocapillary nature.

I am grateful to A.N. Aksenov for technical assistance in preparation of the manuscript.

[4] The angular acceleration can be determined by considering the drop as a rigid ball with water density and mass m.

REFERENCES

1. A. A. Fedorets, Pis'ma Zh. Éksp. Teor. Fiz. **79**, 457 (2004) [JETP Lett. **79**, 372 (2004)].

2. A. A. Fedorets, *Book of Abstracts of International Marangoni Association Congress 2004* (Brussels, 2004), p. 20.
3. A. A. Fedorets, RU Inventor's Certificate No. 2004123030/28(024897) (2004).
4. A. A. Fedorets, RU Inventor's Certificate No. 2004123031/28(024898) (2004).
5. W. L. Bragg, J. Sci. Instrum. **19**, 148 (1942).
6. *Physical Quantities. Handbook*, Ed. by I. S. Grigor'ev and E. Z. Meĭlikhov (Énergoatomizdat, Moscow, 1991) [in Russian].
7. P. Dell'Aversana, J. R. Banavar, and J. Koplik, Phys. Fluids **8**, 15 (1996).
8. R. Monti, R. Savino, M. Lappa, and S. Tempesta, Phys. Fluids **10**, 2786 (1998).
9. *Surface Phenomena and Surface-Active Substances: Handbook*, Ed. by A. A. Abramzon and E. D. Shchukin (Khimiya, Leningrad, 1984) [in Russian].
10. S. L. Revkin and A. A. Aleksandrov, *Thermal Properties of Water and Water Vapor* (Énergiya, Moscow, 1980) [in Russian].

Translated by P. Pozdeev

JETP Letters, Vol. 81, No. 9, 2005, pp. 442–447. Translated from Pis'ma v Zhurnal Éksperimental'noĭ i Teoreticheskoĭ Fiziki, Vol. 81, No. 9, 2005, pp. 556–562.

Increase in Radiation Intensity in a Quasi-Spherical "Double Liner"/"Dynamic Hohlraum" System

V. P. Smirnov[1], S. V. Zakharov[1], and E. V. Grabovskiĭ[2]

[1] *Russian Research Center Kurchatov Institute, pl. Akademika Kurchatova 1, Moscow, 123182 Russia*
e-mail: zakharov@eppra.org

[2] *Troitsk Institute for Innovation and Thermonuclear Research, Troitsk, Moscow region, 142192 Russia*

Received March 18, 2005; in final form, March 31, 2005

A concept of the magnetic implosion of quasi-spherical liners, concentration of their kinetic energies, conversion of energy into thermal radiation, confinement of its energy in the cavity of an emitting plasma shell in the "double liner"/"dynamic hohlraum" system, and the irradiation of a spherical target is proposed for the physics of high energy densities and inertial confinement fusion. The radiation intensity on the target was shown to increase considerably due to capture of radiation in the process of converting the kinetic energy of the liner into radiation. The dynamics of the liners and the generation of radiation are simulated by the ZETA code using a physical model developed for a nonequilibrium plasma in a cylindrical geometry. The effect of the instability and inhomogeneity of the liners on confinement of radiation energy is estimated. © *2005 Pleiades Publishing, Inc.*

PACS numbers: 52.58.Lq, 52.59.Qy

1. Introduction. Magnetic implosion of plasma liners in powerful electric generators creates a dense high-temperature plasma of multiply charged ions and produces intense thermal radiation, which is useful for the physics of high-energy densities and inertial confinement fusion (ICF). In the concept that was proposed in [1] for the generation and confinement of thermal x-ray radiation in a "double liner" (DL), radiation is emitted due to the collision of an external cylindrical plasma liner with an internal liner. The internal liner can be hollow [1] or filled with a low-density material [2].

At high collision velocities of the liners ($V > 4 \times 10^7$ cm/s), the generation of radiation occurs primarily as a transformation of their kinetic energy into thermal energy through a strongly radiative shock wave. Due to the high optical density of the external liner, radiation is partially trapped inside the liners. As a result, the radiation intensity increases within the liner, where a target is placed [1]. Such a scheme of using plasma liners is also called "dynamic hohlraum" (DH) because of its property of confining radiation that is generated in the process of dynamic impact of liners [2].

This DL/DH concept is confirmed by the experimental results obtained on the Angara-5 generator [3–5] and Z-machine accelerator [6–8]. It was shown that intense thermal x-ray radiation is generated at the instant of the collision of liners, is confined inside them, and increases considerably due to trapping in the shell. It is necessary to mention the outstanding results that were obtained in experiments with DH at a current of 20 MA on the Z-machine [6]: the brightness temperature was higher than 215 eV, and the energy absorbed by the 1.7-mm spherical target was more than 20 kJ [7]. These results exceed the respective previous results of indirect laser-driven compression. The energy of absorbed radiation is insufficient for ignition of fusion. It is necessary to increase the kinetic energy of the liner so as to achieve a brightness temperature higher than 250 eV and a target illumination $\epsilon \sim 2.5$ MJ/cm^2 [1, 9] that are needed for ICF. A planned increase in the current up to 26 MA in the ZR-machine [10] has to double, in comparison with [6, 7], the kinetic energy of the liner and the target illumination. These parameters are still insufficient to ignite the thermonuclear target in the cylindrical layout of implosion. However, such energetics could be considered as preliminary for fast ignition by a laser with a relatively low power [9].

In our opinion, another way is the change from cylindrical to spherical implosion of the liners. This change will allow additional kinetic energy to be concentrated in the axial direction and a higher symmetry of the flux irradiating the target to be obtained. The magnetic field of the current that flows on the liners is determined by the distance from the axis of the system, i.e., by the cylindrical coordinate. The cylindrical symmetry of magnetic forces prevents the direct realization of spherical implosion. However, three-dimensional implosion that is close to spherical geometry can be realized by initially redistributing the substance in the liners. The direct spherical compression of the DT fuel by a magnetic field was considered earlier in [11]. This work is devoted to the study of the quasi-spherical implosion of the liners in the DL/DH scheme.

0021-3640/05/8109-0442$26.00

2. Implosion of liners and radiation confinement in the plasma. The DL scheme for generating and confining radiation [1, 3, 12] is based on the following main ideas. The external liner accumulates kinetic energy during implosion by magnetic pressure of the current that flows on the liner. When the velocity $V \sim 5 \times 10^7$ cm/s is reached, the external liner collides with the internal one and is squeezed together with a strong magnetic field that is nearly frozen in it. The pressure of the compressed magnetic field induces a strong shock wave in the substance of the internal liner. This wave generates intense thermal radiation that penetrates into the cavity inside the liner and illuminates a target. The external liner confines this radiation, preventing its escape outside. For effective screening, the external liner has to be made of a material with a large atomic number $Z \gg 1$. The internal liner should be made of a composition of light and heavy elements, so that it can generate intense radiation and simultaneously transit the thermal radiation of the shock wave into the interior [13]. Due to the transparency of the internal liner, the spectral structure of the radiation that is generated by the shock wave is determined by the spectrum of the radiating substance. This radiation is absorbed and thermalized and, acquiring a spectrum close to the Planck spectrum, fills the cavity inside the liner. Radiation is the main factor in both energy redistribution and formation of the state of the plasma layer during the process of liner collision.

The proposed scheme was theoretically considered in detail in [1, 12] and, as mentioned above, was tested experimentally for the case of cylindrical liners [3, 4, 6, 7]. Moreover, the change from the cylindrical to quasi-spherical implosion of liners can obviously give an additional gain in concentrating the kinetic energy of the liner and in confining the radiation energy. However, in the cylindrically symmetric magnetic field, the quasi-spherical implosion of the liner requires profiling the distribution of its mass.

We consider the stage of the magnetic acceleration of the liner in the approximation that the thickness of the shell (on the order of the skin depth [14]) is much less than its radius. Let the current $I(t)$ flow on this thin shell and create an azimuthal magnetic field $B_\varphi = 2I/cr$ near the surface of the shell. Here, r is the distance from a point on the shell to the axis of symmetry and c is the speed of light (the Gauss system of units is used). For spherical coordinates, where R is the radius and θ is the polar angle, $r = R\sin\theta$ (it is natural to assume azimuthal symmetry). In this case, the Lorentz force $\mathbf{j} \times \mathbf{B}$ is perpendicular to the surface of the shell. The radial component $\dot{R}$ of the shell velocity is described by the equation

$$m\ddot{R} = -\frac{I^2}{c^2 2\pi R^2 \sin^2\theta}, \tag{1}$$

where $m(\theta)$ is the mass of the liner per unit surface area. The implosion of the initially spherical liner further proceeds spherically if the angular dependence of the mass distribution in the liner has the form

$$m(\theta) \propto \sin^{-2}\theta. \tag{2}$$

For distribution (2), the implosion of the liner is self-similar, so the quantity $\mu = \text{const} = m4\pi R^2\sin^2\theta$ remains constant. In this case, Eq. (1) can be immediately solved for an arbitrary time dependence of the current $I(t)$. Assuming zero initial velocity, we obtain

$$\mu(R_0 - R)c^2 = 2\int_0^t\int_0^{t'} I^2(t')dt'dt, \tag{3}$$

where $R_0 = R_{t=0}$ is the initial radius of the liner. The kinetic-energy density per unit surface area of the liner is

$$\frac{1}{2}m\dot{R}^2 = \frac{\left(\int I^2 dt\right)^2}{c^4\mu\pi R^2\sin^2\theta}. \tag{4}$$

A comparison shows that, due to the axial cumulation in the quasi-spherical implosion under identical other conditions (current, compression ratio), this density is higher than the value for the cylindrical case [12] by the ratio of $(R_0 - R)/R$ to $\ln(R_0/R)$.

Let us consider the stage of collision between the external and internal liners. In the ideal case, where the external liner has a large optical depth and the internal liner is almost transparent, the effective temperature of radiation coincides with the plasma temperature, and the transfer of radiation energy flux density $\mathbf{F}$ from the internal liner through the external one can be described in the approximation of radiative heat transfer. Due to a relatively high rate of radiation transfer processes, we consider the quasi-stationary case, where the radiation flux through the external liner is constant:

$$\nabla\mathbf{F} = -\nabla\frac{4l}{3}(\sigma T^4) = 0. \tag{5}$$

Here, σ is the Stefan–Boltzmann constant and l is the Rosseland-averaged free path of photons The temperature dependence of this path for the tungsten plasma has the form $l \propto T^\eta$ with $\eta \sim 3.6$ in the range 175 eV $< T <$ 300 eV [12]. The plasma-density dependence of the Rosseland path in the approximation of local thermodynamic equilibrium (LTE) is close to the inversely proportional function $l \propto 1/\rho$. Passing to spherical variables, which are natural for the case under consideration, and taking into account the azimuthal symmetry

of the flux $\mathbf{F} = (F_R, 0, F_\theta)$, we obtain the following equation from equation of radiative heat transfer (5):

$$\frac{1}{R^2}\frac{\partial}{\partial R}R^2\frac{4l}{3}\frac{\partial}{\partial R}(\sigma T^4) + \frac{1}{R^2\sin\theta}\frac{\partial}{\partial\theta}\sin\theta\frac{4l}{3}\frac{\partial}{\partial\theta}(\sigma T^4) = 0. \quad (6)$$

After the substitution of the power dependence for the Rosseland path $l \propto T^\eta/\rho$ and $\Phi = T^{\eta+4}$, this equation becomes linear with respect to the function Φ and, for a density that is constant along the radius of the external liner (from $R = R_{in}$ to $R = R_{out}$) but inhomogeneous in the angle θ as $\rho \propto 1/\sin^2\theta$ according to mass distribution (2), has a solution in the form of hypergeometric polynomials. As a result, the expression for temperature, which is symmetric with respect to the equatorial plane, has the form

$$T = \left(\Phi_0(R) + \sum_{n=1}\Phi_n(R)\psi_n(\cos^2\theta)\right)^{1/(\eta+4)}. \quad (7)$$

Here, $\Psi_n(R)$ and $\psi_n(\cos^2\theta)$, are the nth harmonics of the solutions of the radial and angular parts of the equation after separation of variables, respectively; $\psi_n(x)$ is the hypergeometric polynomial; $\Phi_0(R)$ is the spherically symmetric component corresponding to the solution of the radial part of Eq. (6) in the equatorial plane for $\theta = \pi/2$, where the liner mass and, accordingly, the optical path are minimal for the case under consideration. The spherically symmetric part is dominant in distribution (7), and, since $\eta + 4 \gg 1$, the angular dependence of temperature distribution is weak. This property corresponds to the well-known fact that radiative heat transfer leads to strong isotropization of the radiative field in a cavity, and that the temperature is determined by the most optically thin part of the cavity wall. For this reason, we will ignore the anisotropy of the temperature distribution in our further estimations of the radiation temperature in the cavity of the liners. Then, the radial part of equation (6) for $\theta = \pi/2$ is

$$\frac{1}{R^2}\frac{\partial}{\partial R}R^2\Phi_0 = 0.$$

Its solution, which relates the radiation temperatures inside $[T_{in} = T(R_{in})]$ and outside $[T_{out} = T(R_{out})]$ the liner, can be written, by analogy with the cylindrical case [12], from the condition that the flux of the radiation energy on the outer boundary of the shell, at $R = R_{out}$, corresponds to the blackbody law, $F_R = \sigma T_e^4$:

$$\sigma T_{in}^4 = \sigma T_{out}^4\left(\frac{l_{out}}{l_{in}} + \alpha\frac{R_{out}}{R_{in}}\frac{\Delta R}{l_{in}}\right). \quad (8)$$

Here, $\Delta R = R_{out} - R_{in}$ is the thickness of the liner, $\alpha = 3(\eta + 4)/16$, and l_{in} and l_{out} are the Rosseland paths in the inner and outer layers of the external liner with temperatures T_{in} and T_{out}, respectively. From the condition of the conservation of energy flux, the temperature T_{out} is determined by the radiation power of the shock wave [1, 12] in the quasi-steady blackbody approximation:

$$\sigma T_{out}^4 \approx \frac{8}{3}\rho_{in}V^3\left(\frac{R_{in}}{R_{out}}\right)^2, \quad (9)$$

where ρ_{in} is the density of the internal liner. It is necessary to point out that the approximation of the radiative heat transfer is valid if $l_{in} \ll \Delta R$. Even in this case, as was shown in [12], the criteria of LTE are not well satisfied, and, generally speaking, numerical solution should be considered for the case of the absence of LTE. However, relation (8) between the temperatures is valid with satisfactory accuracy even in the cylindrical case [12, 15] if the temperature is thought of as the radiation temperature.

Comparison of Eqs. (8) and (9) with the respective expressions for the double cylindrical liner [12, 15] shows that the confinement of the radiation energy is more effective in the spherical case than in the cylindrical one. This is due to both the algebraic relation $\Delta R/R_{in} > \ln(R_{out}/R_{in})$ and the absence of the open ends of the liner, which must be closed with materials having high albedo for thermal x-ray radiation. Evaluation of solution (8) shows the gain in the flux illuminating the target due to trapping of radiation by the external liner [1]. The effect of radiation amplification increases with the optical thickness of the liner.

In the framework of this simple model, the change from cylindrical to spherical implosion is estimated to give a gain factor of four to five in the flux irradiating the target. This model disregards the implosion instability of the liner. However, as was demonstrated in the numerical calculations in [16], the quasi-spherical implosion is more sensitive to instability, because the liners are curved and the initial mass distribution over the angle θ is nonuniform. Though these two factors seem to compensate each other (the larger mass is placed at the smaller radius from the axis of symmetry) and, thus, the initial long-wave disturbances are eliminated, for shorter wave modes of the Rayleigh–Taylor instability, they create additional perturbations in comparison with the cylindrical case.

A computer simulation including the entire variety of the processes of magnetic implosion in the radiative liners is needed to estimate the effect of the plasma dynamics of the liners and to determine more accurate initial parameters of the liners and the power of the flux irradiating the target.

3. Dynamics of quasi-spherical implosion and generation of radiation. The radiative-magnetohydrodynamic code ZETA [17, 18] was used to simulate DL/DH with the parameters of an electric generator, which are close to the parameters of the ZR-machine. The ZETA code combines a two-dimensional two-tem-

perature (temperatures of electrons and ions) MHD model and the multigroup radiative transfer. Radiative transfer is described by the equations for spectral intensity I_ω in the quasi-stationary approximation: $(\mathbf{\Omega}\nabla)I_\omega = j_\omega - k_\omega I_\omega$. The opacity κ_ω and emissivity j_ω of the plasma, as well as the equation of state for the plasma, are calculated by the THERMOS code [19] in the mean-ion model, in which all possible levels and transitions are taken into account. The energy levels of ions, cross sections, and other quantities are calculated on the basis of the relativistic Hartree–Fock–Slater model.

After several preliminary calculations, the layout shown in Fig. 1 was chosen as the variant for analyzing the effect of implosion dynamics and generation of radiation. The external tungsten liner is located between the electrodes, which have the beam angle 90°, i.e., $45° < \theta < 135°$. To maintain a good electrical contact of the electrodes with the liner for $R < 0.6$ cm, the electrodes are inclined from the radial direction at an angle that is slightly less than the angle of thermal scattering of the internal liner after its collision with the external one. Accordingly, the distance between the electrodes is varied from 2.8 cm to 6 mm. To reduce the effect of instability, the nested double-shell external liner was chosen. The outer spherical shell has radius $R_{01} = 2$ cm and the mass per unit length at the equator $M_1 = 5.65$ mg/cm [the mass density per unit area of the shell $m(\pi/2) = 0.45$ mg/cm^2 or $\mu = 22.6$ mg]. The inner spherical shell has radius $R_{02} = 1$ cm with the mass per unit length at the equator $M_2 = 2.85$ mg/cm. The angular distribution of the mass of the shells corresponds to dependence $m(\theta) \propto \sin^{-2}\theta$ (2). We note that the simplified analytical model outlined above for the spherical implosion is easily generalized to the case of the presence of an intermediate shell if the perfectly inelastic collision of the shells is assumed (this assumption is valid due to the low thermal pressure and the fast diffusion of the magnetic field in the strongly radiating plasma [14, 18]) and if momentum conservation in the collision is used. The internal liner is spherical with radius $R_2 = 2.4$ mm, thickness 0.3 mm, and mass per unit length at the equator $M_1 = 10.6$ mg/cm. The angular distribution of the internal-liner mass corresponds to Eq. (2) in the angular range $45° < \theta < 135°$ and is constant beyond this range. The inner liner is made mainly of a material transparent to x-ray radiation (low-density plastic, in this variant) with an addition of 5–10% of tungsten. The outer part of the liner is made of tungsten to protect the inner liner from the intense thermal scattering induced by the radiation of the outer liner at the stage of implosion and to ensure a more effective conversion of the kinetic energy into radiation at the stage of collision. A spherical target should be placed in the center of the cavity of the internal liner (to simplify the simulation, the target is not introduced into the model, because it requires special consideration and a detailed computational grid).

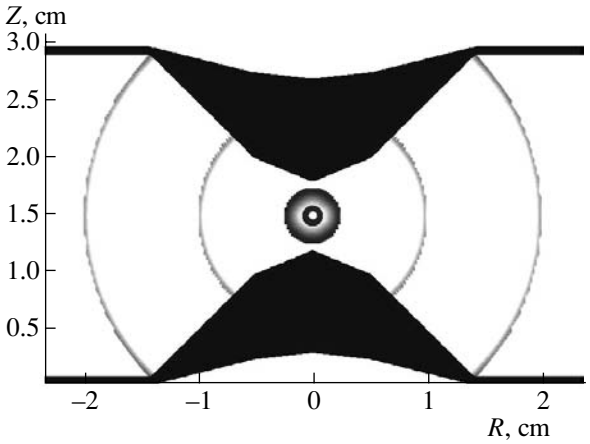

Fig. 1. Layout of the quasi-spherical DL/DH in the axial section view: the electrodes (at the bottom and top), the nested double-shell external liner, and the spherical internal liner with the target inside it.

Implosion dynamics in which the evolution of MHD instabilities is taken into account (to this end, random ±5% disturbances are imposed on the density and shape of the liners), the collision of the liners, and the generation and transfer of radiation are studied in the simulation. The main optimization parameters are the value and distribution of the energy density of thermal radiation in the central cavity of the liners. For simplicity, the target is not considered in the calculations. The evolution of the plasma density is represented in Fig. 2 at the four stages of the process: during implosion of the external shell (at the beginning of collision between the outer and inner liners of the external shell), before the collision of the liners, during the process of the collision, and before pinching of the DH. The pulse of current in the liners and the power of radiation are shown in Fig. 3 as functions of time. The current pulse starts with the 100th ns. Several peaks are observed in the curve of the radiation power. The first of them, with a height of 20 TW at 228 ns, coincides with the instant of collision between the outer and inner shells of the nested external liner. The shell has accumulated 0.8 MJ of kinetic energy to this time, and this result is in good agreement with the simple acceleration model given by Eq. (4). The second peak (75 TW) at 249 ns begins with the collision of the external and internal liners. The collision lasts 6–7 ns and the radiation power increases to 165 TW at 256 ns. At this instant, the formed DH collapses, producing the peak of radiation, and creates the pinch that generates the last peak of 320 TW at 261 ns.

In the process of the DH collapse, thermal radiation fills the volume of the liner, and its intensity increases, due to the effect of trapping, from 240 TW/cm^2 at 250 ns to 550 TW/cm^2 at 256 ns. The brightness temperatures of the radiation at these instants correspond to $T_{\text{in}}^{\text{rad}} \approx 220$ eV and $T_{\text{in}}^{\text{rad}} \approx 270$ eV, respectively. Then, during pinching, the emissivity increases to 1450 TW/cm^2

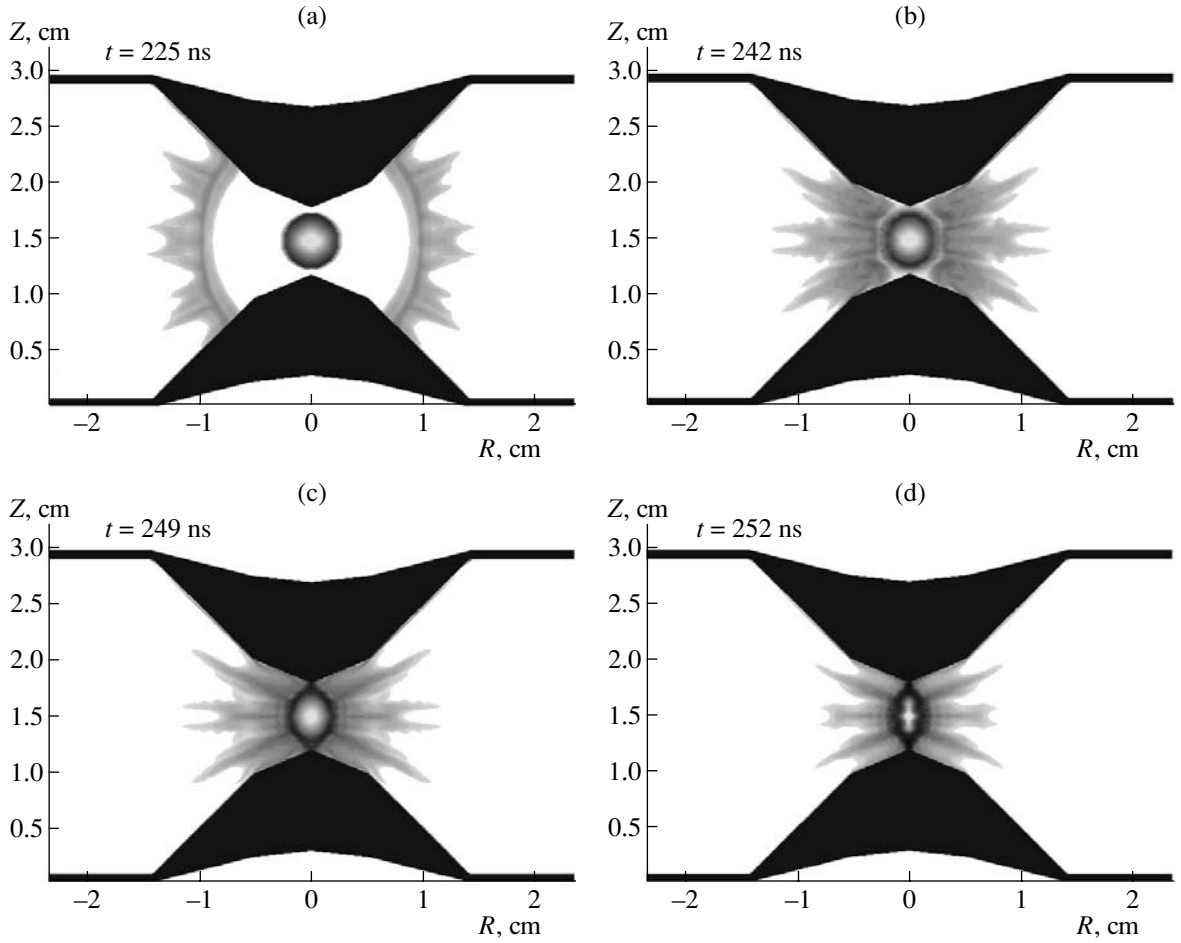

Fig. 2. Density evolution in the DL/DH: the axial section views at 225, 242, 249, and 252 ns. The target was not included in the calculation.

at 261 ns. In our opinion, extremely intense radiation just before pinching can also be used for irradiation of a well-formed target and for obtaining the effect sharpening. We also note that the earlier pinching of the plasma near the electrodes (between the electrodes and the internal liner) gives rise to additional radiation fluxes, which, becoming isotropic in plasma, also irradiate the target and affect it in the same manner as a double-end hohlraum [2].

The effect of instabilities arising during the implosion of the liners is seen in Fig. 2. In the process of implosion, the outer part of the plasma shell is not homogeneous, because the Rayleigh–Taylor MHD instability [18] deforms it. Nevertheless, the diffusion of the magnetic field and the radiative transfer flatten the distortion of the density. When the plasma of the outer shell is decelerated during the collision of the shells of the external liner, the distorted outer layers of the plasma enter into the bulk of the liner, concentrating the kinetic energy in spite of the losses of it in the collision and reducing the negative effect of instability on the efficiency of the energy conversion and confinement of radiation. It should be noted that, since the degree of compression is low and the short-wave modes are smoothed by diffusion, the initial random 5% disturbances were barely seen against developing regular inhomogeneities associated with both the initial spherical curvature of the liners and the distribution of their masses in the angle θ. Despite the distortion of the plasma layer affected by instability, radiative transfer smoothes the radiation distribution in the cavity of the DL/DH.

For more effective conversion, the substance of the liner should have the minimum Rosseland path at given temperature and density, as is seen from the estimate by Eq. (8). At high temperatures and for large Z, the line absorption takes place in the narrow bands of the spectrum, and there are transparent regions that are characterized by a long free path of photons and through which photons escape due to multiple reemission. Using heavy ($Z > 80$) and relatively light ($Z = 64, 67, \ldots$) elements as components of a mixture, one can close the transparent bands of the spectrum and minimize the Rosseland paths. The brightness temperature of the liner that is made of such a mixture can be increased by

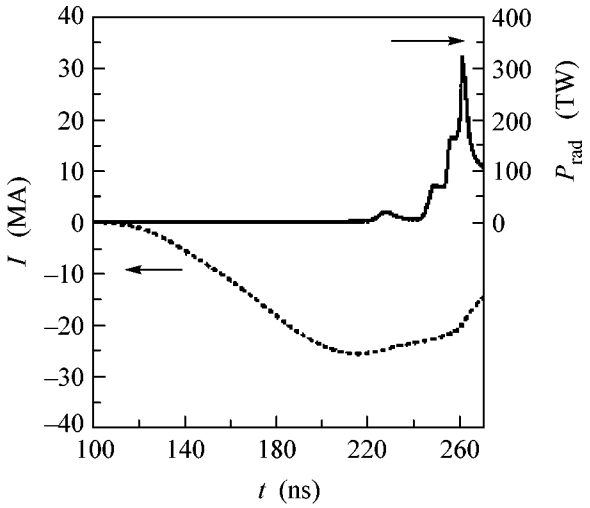

Fig. 3. Time dependence of the (dotted line) current pulse and (solid line) radiation power.

more than 20% [12]; i.e., the intensity of radiation can be more than doubled.

The above calculations show that, despite the instability of the liner implosion, the change to quasi-spherical geometry considerably increases the intensity of radiation inside the DL/DH, as compared with the cylindrical case for the same energies of the pulse generator. The regular behavior of the implosion instability allows for the possible future optimization of the distribution of the liner masses. The choice of the materials for the liners is also a potential way of improving the scheme.

We are grateful to our colleagues, Prof. V.G. Novikov and A.D. Solomyannaya, for the computations and tables of atomic data and to A.Yu. Krukovskiĭ and V.S. Zakharov for assisting in the development of the computer code and in the calculations.

REFERENCES

1. S. V. Zakharov, V. P. Smirnov, *et al.*, Preprint No. 4587/6, IAÉ (Inst. of Atomic Energy, Moscow, 1988).
2. M. K. Matzen, Phys. Plasmas **4**, 1519 (1997).
3. V. P. Smirnov, Plasma Phys. Controlled Fusion **33**, 1697 (1991).
4. V. P. Smirnov, S. V. Zakharov, E. V. Grabovski, *et al.*, in *Proceedings of the I.A.E.A. Drivers for ICF* (Paris, 1995).
5. E. V. Grabovskiĭ, O. Yu. Vorob'ev, K. S. Dyabilin, *et al.*, Zh. Éksp. Teor. Fiz. **109**, 827 (1996) [JETP **82**, 445 (1996)].
6. T. W. L. Sanford, R. W. Lemke, R. C. Mock, *et al.*, Phys. Plasmas **9**, 3573 (2002).
7. J. E. Bailey, S. A. Slutz, *et al.*, in *Proceedings of 14th International Conference on Beams 2002* (Albuquerque, USA, 2002).
8. G. C. Idzorek, R. E. Chrien, D. L. Peterson, *et al.*, in *Proceedings of 28th ICOPS 2001 and 13th IEEE International Pulsed Power Conference* (Las Vegas, 2001), p. 777.
9. A. A. Andreev, A. A. Levkovskii, K. Yu. Platonov, and S. V. Zakharov, in *Proceedings of 30th EPS Conference on Controlled Fusion and Plasma Physics* (St. Petersburg, 2003), P-3.59.
10. C. L. Olson *et al.*, in *Proceedings of 15th International Conference on Beams 2004* (St. Petersburg, 2004).
11. V. N. Mokhov, V. K. Chernyshev, V. B. Yakubov, *et al.*, Dokl. Akad. Nauk SSSR **248**, 352 (1979) [Sov. Phys. Dokl. **24**, 557 (1979)].
12. V. G. Novikov and S. V. Zakharov, J. Quant. Spectrosc. Radiat. Transf. **81**, 339 (2003).
13. S. V. Zakharov and V. G. Novikov, Bull. Am. Phys. Soc. **44** (7), 103 (1999).
14. S. F. Grigor'ev and S. V. Zakharov, Pis'ma Zh. Tekh. Fiz. **13**, 616 (1987) [Sov. Tech. Phys. Lett. **13**, 254 (1987)].
15. V. P. Smirnov, S. V. Zakharov, and V. G. Novikov, in *Proceedings of 15th International Conference on Beams 2004* (St. Petersburg, 2004).
16. V. I. Kosarev, A. I. Lobanov, K. V. Chukbar, and Yu. I. Shestakov, Vopr. At. Nauki Tekh., Ser.: Termoyad. Sint. **3**, 46 (1989).
17. S. V. Zakharov, V. G. Novikov, A. Yu. Krukovskii, *et al.*, *ZETA Code: Physical Models and Numerical Algorithms*, Report KIAM (Moscow, 1994), p. 11.
18. R. Benattar, S. V. Zakharov, A. F. Nikiforov, *et al.*, Phys. Plasmas **6**, 175 (1999).
19. A. F. Nikiforov, V. G. Novikov, and V. B. Uvarov, *Quantum-Statistic Models of High-Temperature Plasma* (Fizmatlit, Moscow, 2000) [in Russian].

Translated by R. Tyapaev

JETP Letters, Vol. 81, No. 9, 2005, pp. 448–451. Translated from Pis'ma v Zhurnal Éksperimental'noĭ i Teoreticheskoĭ Fiziki, Vol. 81, No. 9, 2005, pp. 563–567.

New Physical Concept of the Formation of Dust Crystals

V. N. Tsytovich

General Physics Institute, Russian Academy of Sciences, ul. Vavilova 38, Moscow, 119991 Russia
e-mail: tsytov@lpi.ru

Received March 16, 2005; in final form, April 6, 2005

A clear physical model is proposed for phase transitions in a dusty plasma. According to this model, the formation of plasma dust crystals is associated with the nonlinear effect of the collective attraction of dust particles. The nonlinear collective attraction between negatively charged dust particles corresponds to large charges of dust particles used in the available experiments. This concept provides a new physical model of crystallization that is attributable to the capture of dust particles in an attractive potential well rather than to the strong interaction between them. Calculation using this model yields the depth of the attractive potential well and the critical coupling constant in good agreement with the available experimental data. © *2005 Pleiades Publishing, Inc.*

PACS numbers: 52.27.Lw

1. A main mystery of plasma dust crystals discovered in experiments [1–7] is that the observed values of the critical coupling constant are inconsistent with any physical and theoretical estimates of this quantity. The critical coupling constant is the ratio of the mean energy of the Coulomb interaction between dust particles to the critical transition temperature $T_{d,\,cr}$ and is given by the expression $\Gamma_{cr} = (4\pi n_d/3)^{1/3} Z_d^2 e^2/T_{d,\,cr}$, where Z_d is the charge number of dust particles, $(3/4\pi n_d)^{1/3}$ is the mean distance between dust particles, and n_d is the concentration of dust particles. The Γ_{cr} values observed in experiments [1–3] for rf discharges at a pressure near 1 torr and in a dense plasma [4–7] are close to 10^3–10^4 and 3–10, respectively. At the same time, the only available numerical simulation of strong interaction for a so-called single-component plasma model [8] yields values of 150–170. Since the observed Γ_{cr} values are large, the common opinion is that the formation of dust crystals is possible in strongly interacting systems.

In this work, a new physical model is proposed, in which interaction is collective rather than strong and dust particles in phase transitions are localized in a shallow attractive potential well, which arises due primarily to the nonlinear screening of large charges of dust particles. The balance between nonlinear screening at short distances and collective attraction at large distances determines the mean interparticle distances corresponding to the values observed in the transition to the crystalline state. It is shown that this model explains most observations in both a low-density plasma [1–3, 7] and a dense plasma [4, 5] and yields Γ_{cr} values and interparticle distances that are very close to observable values. A certain role of strong interactions in this model is that they prevent the penetration of particles into the region of strong interactions. The main role in the formation of the crystalline state belongs to weak interactions beyond the region of strong interactions. These weak interactions for the available experiments are collective and include a relatively shallow attractive well, where dust particles can be localized when a dust crystal is formed. The strong character of the interactions is manifested in nonlinear screening for large charges of dust particles (Z_d values measured in the available crystallization experiments are $\approx 10^3$–10^4). This nonlinear screening physically means that the electrostatic potential ϕ at short distances around dust particles satisfies the strong-nonlinearity condition $|e\phi| \gg T_i$ (where T_i is the ion temperature in energy units) and that nonlinearity is expanded at distances much larger than the linear Debye screening radius $\lambda_{Di} = \sqrt{T_i/4\pi n_i e^2}$ (in most experiments, the ion temperature is much lower than the electron temperature, $\tau = T_i/T_e \approx 10^{-2} \ll 1$). At the same time, it is shown that the size of the nonlinear-screening region is less than the size at which collective attraction is manifested [9]. Therefore, the appearance of collective attraction whose range is larger than the nonlinear screening size is determined by the efficiency of nonlinear screening. As is shown in this work, nonlinear screening is very strong and determines the amplitude of collective attraction beyond the nonlinear-screening region. Such an effect corresponds to nonlinear collective attraction and has the same characteristic sizes as the previously discovered effect of linear collective attraction [9], but nonlinearity determines much stronger collective attraction than that observed in [9].

The nonlinearity of screening is governed by the parameter

$$\beta = \frac{z}{\tau}\frac{a}{\lambda_{Di}}; \quad z = \frac{Z_d e^2}{aT_e}, \tag{1}$$

0021-3640/05/8109-0448$26.00

where a is the radius of a dust particle and the dimensionless charge z of dust particles is always about 1 (according to the concept of the wake potential of dust particles, but it is equal to about 2–4 in experiments). For $\beta \sim 1$, the nonlinear radius is equal to the radius of linear screening. In experiments [1–3, 7] and [4, 5], β is about 50 and 2–5, respectively; i.e., nonlinearity is always strong, and the concept of linear screening cannot be used to interpret experiments. Radical change in the character of screening was discovered in [9, 10]. This change, so-called overscreening, is associated with collective effects and is manifested as the reversal of the sign of the polarization charge around dust particles. Thus, this behavior leads to the attraction between dust particles and to their pairing. In this work, we prove that nonlinear screening significantly increases collective attraction, which leads to the crystallization model explaining the critical values Γ_{cr} of the coupling constant that are observed in the available experiments.

2. It has long been known that large charges in a plasma are screened nonlinearly. Strong nonlinearity is most often considered in a model known as Gurevich's model [11], in which the ion polarization charge ρ_i is proportional to $\sqrt{\phi}$. A simple analytical expression that well approximates the solution of Poisson equations with a nonlinear potential [11] was proposed in [12]. For dust particles whose charge is equal to $-Z_d e$, this expression has the form

$$\phi(r) = -\frac{Z_d e^2}{r}\psi\left(\frac{r}{\lambda_{Di}}\right);$$
$$\psi(r) = \left(1 - \frac{r}{R}\right)^4; \quad R = 3.6\beta^{1/5}. \tag{2}$$

Beginning with the second of Eqs. (2), all distances r are measured in the linear Debye radius $\lambda_{Di} = \sqrt{T_i/4\pi n_i e^2}$ and R is the nonlinear screening radius measured in λ_{Di}.

According to Eqs. (2), the nonlinear screening radius for $\beta \gg 1$ is much larger than λ_{Di}. The result obtained in [12] is easily generalized for arbitrary nonlinearity $\rho_i \propto \phi^\nu$ with $0 < \nu < 1$:

$$\psi(r) = \left(1 - \frac{r}{R(\beta, \nu)}\right)^{\frac{2}{1-\nu}};$$
$$R(\beta, \nu) = d(\nu)\beta^{\frac{1-\nu}{3-\nu}}; \quad d(\nu) \approx (1.9 + 12\nu^3). \tag{3}$$

The coefficient $d(\nu)$ is given in the form of an approximate analytical expression obtained using numerical results [13] for the range $0.1 < \nu < 0.8$. The range of nonlinear screening increases with both β and ν. Expression (3) will be used below to obtain the amplitude of nonlinear collective attraction.

3. As was mentioned in [9], collective attraction arises because a constant source of ionization is required in order to ensure balance of energy and plasma particles in a system whose size is much larger than the mean free path of ions. This source produces additional electrons and ions between two interacting dust particles. These electrons quite easily leave the region between dust particles, whereas ions are decelerated due to friction on either dust or neutral atoms. Under the condition $\beta \gg 1$, which is satisfied in the available experiments, friction on neutral atoms dominates. Under the above conditions, screening at distances larger than the nonlinear screening radius can be described in the linear approach, in which, however, the plasma flux $\mathbf{\Phi}$ absorbed by dust particles is taken into account in addition to the electrostatic polarization field $\mathbf{E}$. Fields $\mathbf{E}$ and $\mathbf{\Phi}$ are related to each other, because a decrease in the polarization charge due to the flux to dust particles changes the polarization field $\mathbf{E}$, and the polarization changes fluxes and the field $\mathbf{\Phi}$. As a result, in the simplest case of linear screening, two exponents appear at large distances instead of one exponent (as in an ordinary plasma with Debye screening). As was shown in [7], for the most experimentally interesting case, where the ionization rate is proportional to the electron concentration, the index of the first exponential is real [$\psi \propto \exp(-\lambda_1 r)$], and the index of the second exponential is imaginary [i.e., this exponential is representable as $\psi \propto \cos(\lambda_2 r)$]. Therefore, a system of attractive wells appears:

$$\psi = A\exp(-\lambda_1 r) + B\cos(\lambda_2 r). \tag{4}$$

The relation between λ_1 and λ_2 is determined by the coupling constant k_0^2 of the two fields $\mathbf{E}$ and $\mathbf{\Phi}$ near interacting dust particles (see [9]). Here, we attribute this coupling constant to friction on neutral particles, because it dominates in the available experiments for $\beta \gg 1$. We also introduce the ionization factor α_{ion}, assuming that the number of electron–positron pairs created by the ionization source over the mean free path is equal to $\alpha_{ion} n_e/n_0$, where n_e is the local electron concentration and n_0 is the plasma concentration far from interacting particles. Such a relation represents the basic features of ionization in all experiments where dusty plasma crystals are observed. Moreover, the condition $\tau = T_i/T_e \ll 1$ for the electron and ion temperatures is satisfied in all experiments. In this case, calculations provide the following expressions for the coupling constant and coefficients λ_1 and λ_2:

$$k_0^2 = \frac{\alpha_{ion} z}{(1 + 2\sqrt{\pi}\alpha_{ion})(1 + z)}, \tag{5}$$

$$\lambda_1 = \sqrt{k_0^2 + 1 + \frac{\alpha_{ion} 2\sqrt{\pi}}{(1 + \alpha_{ion} 2\sqrt{\pi})(1 + z)}}, \tag{6}$$

$$\lambda_2 = \frac{k_0}{\lambda_1}\sqrt{\frac{\tau\alpha_{ion} 2\sqrt{\pi}}{1 + \alpha_{ion} 2\sqrt{\pi}}}. \tag{7}$$

In contrast to the expressions derived in [9], the coupling constant of two fields is determined by friction of ions on neutral particles rather than on dust. As was shown in [13], friction with dust decreases by two or three orders of magnitude as β increases from 1 to 100. Therefore, friction on neutral particles is responsible for the effect of collective attraction for $\beta \gg 1$ (expressions obtained in [9] well describe collective attraction for $\beta \ll 1$, when friction occurs primarily on dust). The nature of collective attraction does not change significantly when one friction force is exchanged for the other frictional force and remains the same as in [9]. The model is considerably simplified, because collective constants given by Eqs. (5)–(7) in the case under consideration are independent of the nonlinear parameter β governing nonlinear screening (3).

4. The amplitudes of nonlinear collective attraction, which is discussed in this work, are determined by nonlinear screening in the limit where nonlinear effects become weak and solution (3) is transformed into solution (4). The physical condition for such a transformation is the equality of the potential energy of the screened charge to the mean thermal energy of ions (for $\tau \ll 1$, nonlinearity is almost completely associated with the ion plasma component). In real calculations, the amplitudes A and B in Eq. (4) are obtained from the joining conditions for the potential and field at the distance $R(\beta, \nu)(1 - \Delta(\beta, \nu))$, where Δ is the solution of the transcendental equation

$$\frac{(\Delta(\beta, \nu))^{\left(\frac{2}{1-\nu}\right)}}{1 - \Delta(\beta, \nu)} = d(\nu)\beta^{-\frac{2}{3-\nu}}. \quad (8)$$

The quantity Δ characterizes the relative difference between the nonlinear radius R and the distance at which nonlinear screening is transformed into linear screening with characteristic form (4), which is determined by collective effects. Calculations show that the nonlinear screening radius $R(\beta, \nu)$ increases, for $\beta \approx 0.5$, from $2\lambda_{Di}$ to $5.5\lambda_{Di}$ when ν increases from 0.1 to 0.7 and increases with β, reaching $(7–11)\lambda_{Di}$ for $\beta = 100$. Numerically solving Eq. (8), we conclude that $R(\beta, \nu)(1 - \Delta(\beta, \nu))$ values are approximately identical for all ν values and are close to λ_{Di}, but they become different with an increase in β and lie in the range $(3.9–5.5) \times \lambda_{Di}$ for $\beta = 100$. The coefficients A and B obtained from the joining conditions for both the potential and the field determine both unknown constants and thereby completely determine the plasma flux to a dust particle. According to the corresponding results, in contrast to the case $\beta \ll 1$ [9], the coefficient B is negative over a wide region of the parameters; i.e., it describes attraction. Previously, in [9], attraction for the case $\beta \ll 1$ arose only because the $\cos(\lambda_2 r)$ term (whose coefficient is always positive) in Eq. (4) is sign-alternating. Thus, nonlinear screening substantially changes the character of attraction at large distances. For $\beta \gg 1$, according to the joining condition, the negative coefficient B maximal in absolute value reaches a value near –0.4 for small ν values near 0.1 and small $\beta \approx 1$. The negativity of the coefficient B means that the first maximum of the attractive potential can arise immediately over the nonlinear screening radius. However, with an increase in β, B values remaining negative decrease in absolute value, whereas the coefficient A always increases from 1 for $\beta \approx 1$ to about 10 for $\beta = 100$. This behavior means that, with an increase in β, the possibility of the appearance of the first potential well immediately over the nonlinear screening radius disappears at large β values, and the first potential well at large β values is determined by the alternating term containing a cosine in solution (4). The ratios of characteristic distances in Eq. (4) to the nonlinear screening radius are determined by the relations $R_1^{-1} = \lambda_1(1 - \Delta(\beta, \nu))$ and $R_2^{-1} = \lambda_2(1 - \Delta(\beta, \nu))$. According to calculations, both these quantities decrease as β increases: the exponential screening length divided by λ_{Di} decreases from a value of about 1 for $\beta \approx 1$ to 0.1 for $\beta = 100$, and R_2 decreases from a value of about 10 for $\beta \approx 1$ to a value of about 3 for $\beta = 100$. As a result, the position of the first minimum changes stepwise as β increases. Using these results, one can determine the first attractive minimum, its distance divided by the nonlinear radius R, and the attraction energy divided by $Z_d^2 e^2/R$. The distance of the first minimum changes stepwise as β increases, because the negativity of the coefficient B is compensated by the increasing coefficient A, and the first minimum appears only when $\cos(\lambda_2 r)$ is negative. For lower β values, the distance of the first potential minimum is quite close to R and the attraction potential energy is high and decreases as β increases. The jump in the position of the first minimum occurs at $\beta \approx 10$. The attraction potential energy is quite high before this jump and is equal to about –0.2 in dimensionless units [for $Z_d \approx 3 \times 10^3$, $R(1 - \Delta) \approx 3$], and it is equal to 10–30 eV after the jump. After the jump, the potential well depth first increases with β and then decreases. This depth is much less than the value before the jump and may be near the transition temperature to the crystalline state. The attraction-energy jump that occurs as β increases is of interest for interpretation of the simultaneous observation of different crystalline structures in different sections of a discharge in the early works devoted to dusty plasma crystals [2].

5. It is natural to attribute the appearance of crystals in the presence of potential minima to the localization of particles in these minima. In this case, the distances of potential minima are expected to be close to the interparticle distances in the crystal lattice. This is the case according to estimates.

The coupling constant $\Gamma_{cr} = (4\pi n_d/3)^{1/3} Z_d^2 e^2/T_{d,cr}$ is another measuring parameter. If particles are localized in the attractive potential well, we arrive at the simple relation (see also [14])

$$\Gamma_{cr} = \frac{1}{\psi_{min}(\beta, \nu)}, \quad (9)$$

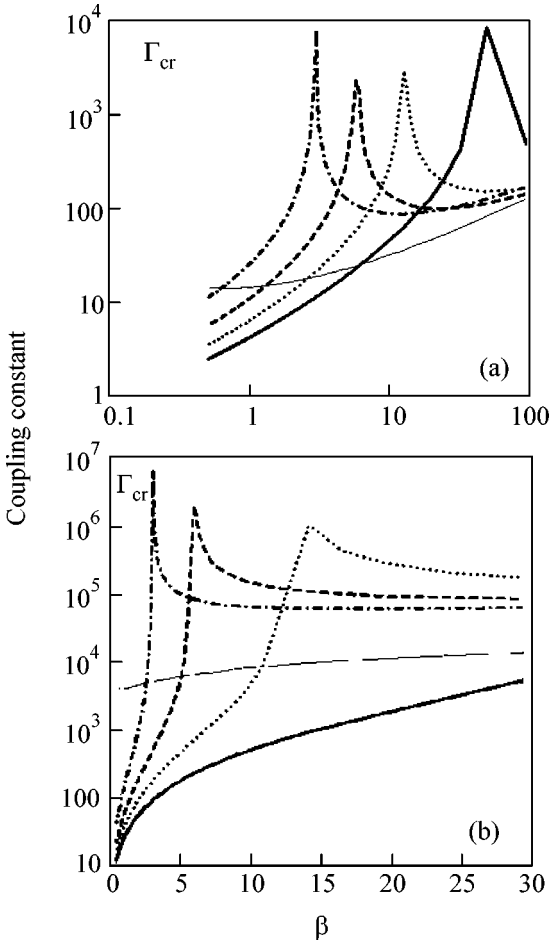

Fig. 1. Coupling constant Γ_{cr} calculated with $a/\lambda_{in} = 0.3$ vs. the nonlinear parameter β for $\tau = T_i/T_e$ = (a) 0.1 and (b) 0.03 and for the nonlinearity degree of the screened potential ν = (thick solid line) 0.1, (dotted line) 0.3, (dashed line) 0.5, (dash–dotted line) 0.7, and (thin solid line) 0.9 (close to Yukawa screening). The peak of Γ_{cr} appears because the first potential minimum, which is attributed to nonlinear screening at small distances, disappears and the potential minimum at large distances appears due to the alternating sign of the collective interaction. As is seen, as ν increases, the peaks are shifted towards larger β values and the maximum for $\tau = 0.1$ and 0.03 disappears at ν = 0.9 and 0.7, respectively.

where $\psi_{min}(\beta, \nu)$ is the screening factor at the potential-well minimum. Explicit Γ_{cr} values that can be compared to experiments have not yet been obtained. Figure 1 shows $\Gamma_{cr}(\beta, \nu)$ calculated as a function of β for various ν values. The appearance of sharp peaks corresponds to the disappearance of the first potential minimum or the disappearance of interaction, which must always occur when repulsion is changed to attraction. The peaks in Γ_{cr} are shifted towards larger β values as ν increases or τ decreases. For $\tau = 0.01$, peaks disappear for any ν values. The results presented in the figure completely explain large Γ_{cr} values observed in most experiments with the transition to a crystalline state [1–3, 7] in rf discharges and relatively small Γ_{cr} values 4–10 in experiments at high pressures [4, 5]. The calculated positions of the potential minima correspond to the observed interparticle distances after the transition to the crystalline state.

The clear physical model of crystallization that is proposed in this work will provide considerably deeper insight into the new state of matter discovered in experiments in which plasma crystals are observed. Moreover, this model can be used to predict new physical phenomena and new states that could be observed in future experiments.

In the framework of the above model, three basic conditions are required for plasma crystallization:

(i) Systems must be open with substantially variable charge and collective interaction.

(ii) Screening of dust charges must be substantially nonlinear.

(iii) Sizes of a system must be much larger than the mean free path of ions with respect to absorption on dust particles.

These conditions are satisfied in most of the available experiments.

REFERENCES

1. H. Thomas, G. Morfill, V. Demmel, and J. Goree, Phys. Rev. Lett. **73**, 652 (1994).
2. J. H. Chu and I. Lin, Physica A (Amsterdam) **205**, 183 (1994).
3. Y. Hayashi and K. Tachibana, Jpn. J. Appl. Phys. **33**, L804 (1994).
4. V. Fortov, A. Nefedov, O. F. Petrov, *et al.*, Phys. Lett. A **219**, 89 (1996).
5. V. E. Fortov, A. P. Nefedov, O. F. Petrov, *et al.*, Pis'ma Zh. Éksp. Teor. Fiz. **63**, 176 (1996) [JETP Lett. **63**, 187 (1996)].
6. V. E. Fortov, A. P. Nefedov, V. M. Torchinskiĭ, *et al.*, Pis'ma Zh. Éksp. Teor. Fiz. **64**, 86 (1996) [JETP Lett. **64**, 92 (1996)].
7. V. E. Fortov, A. P. Nefedov, O. F. Petrov, *et al.*, Phys. Rev. E **54**, R2236 (1996).
8. S. Ichimaru and S. Ogata, in *Proceedings of the Yamada Conference XXI on Strongly Coupled Plasma Physics* (1990), p. 101.
9. V. N. Tsytovich, Pis'ma Zh. Éksp. Teor. Fiz. **78**, 1283 (2003) [JETP Lett. **78**, 763 (2003)].
10. V. N. Tsytovich and G. E. Morfill, Fiz. Plazmy **28**, 195 (2002) [Plasma Phys. Rep. **28**, 171 (2002)].
11. Y. Al'pert, A. Gurevich, and L. Pitaevsky, *Space Physics with Artificial Satellites* (Nauka, Moscow, 1964; Consultant Bureau, New York, 1965).
12. V. N. Tsytovich, N. Gusein-zade, and G. E. Morfill, IEEE Trans. Plasma Sci. **32**, 637 (2004).
13. V. N. Tsytovich, U. de Angelis, A. V. Ivlev, *et al.*, submitted to Phys. Plasmas.
14. V. N. Tsytovich and G. Morfill, Plasma Phys. Controlled Fusion **48**, B527 (2004).

Translated by R. Tyapaev

JETP Letters, Vol. 81, No. 9, 2005, pp. 452–457. Translated from Pis'ma v Zhurnal Éksperimental'noĭ i Teoreticheskoĭ Fiziki, Vol. 81, No. 9, 2005, pp. 568–573.

Optical and Magneto-Optical Studies of a Multiferroic $GaFeO_3$ with a High Curie Temperature

A. M. Kalashnikova[1], R. V. Pisarev[1], L. N. Bezmaternykh[2], V. L. Temerov[2], A. Kirilyuk[3], and Th. Rasing[3]

[1] *Ioffe Physicotechnical Institute, Russian Academy of Sciences, Politekhnicheskaya ul. 26, St. Petersburg, 194021 Russia*
e-mail: kalashnikova@mail.ioffe.ru

[2] *Kirenskiĭ Institute of Physics, Siberian Division, Russian Academy of Sciences, Akademgorodok, Krasnoyarsk, 660036 Russia*

[3] *IMM, Radboud University of Nijmegen, 6525 ED Nijmegen, The Netherlands*

Received March 21, 2005

Single crystals of a noncentrosymmetric orthorhombic pyroelectric ferrimagnet $Ga_{2-x}Fe_xO_3$ with a Curie temperature within 260–345 K have been grown by the flux method. It has been found that the electrical properties of the single crystals varied over a broad range from 10^5 to 10^{13} Ω cm depending on the presence of transition-metal oxide impurities. The dispersion relations for all three principal dielectric functions of orthorhombic $GaFeO_3$ have been determined in the range 0.7–5.4 eV by spectroscopic ellipsometry. The spectra of the dielectric functions of the orthorhombic $Ga_{2-x}Fe_xO_3$ crystals are compared with the spectra of the trigonal crystals. The Faraday effect and second-harmonic generation are studied, and the law of the transition to the paramagnetic state has been determined. The crystallographic and magnetic contributions to the second-harmonic generation are analyzed. © *2005 Pleiades Publishing, Inc.*

PACS numbers: 42.65.Ky, 75.50.Gg, 78.20.–e

Materials and multiphase heterostructures characterized by several coexisting order parameters are referred to as multiferroics [1] and have been known since the 1960s [2, 3]. Although they demonstrate interesting physical phenomena such as magnetoelectric and piezomagnetic effects, attempts at designing devices based on these effects proved to be unsuccessful because of the small values of their cross susceptibilities between different order parameters. However, some works have recently reported about "giant" cross susceptibilities in multiferroics [2–5]. This would open up real possibilities for the practical use of these materials in magneto- and optoelectronics. At present, the inquiries into multiferroics are based, on the one hand, on a more advanced technological base and, on the other, on the possibility of theoretical and *ab initio* predictions of materials and structures with predetermined physical properties. It is also worth noting that, since early works on multiferroics, the physical methods of investigation have become much more elaborated, so that there is a real possibility to study phenomena that were inaccessible and even unknown 30–40 years ago. As an example, we mention the spectroscopic studies of optical harmonic generation in multiferroics [6].

In this work, we report optical and magneto-optical properties of a multiferroic $Ga_{2-x}Fe_xO_3$ [7] that is an interesting object for physical study and can become a basis for new promising materials because of its high transition temperature to the paramagnetic state and, as a consequence, because the electric and magnetic order parameters interact in it at room temperature. The specific feature of this material is that, depending on the value of x, its crystal structure and physical properties change. Of the greatest interest are the compositions with concentration $0.7 \le x \le 1.4$, which crystallize in the noncentrosymmetric pyroelectric $Pc2_1n$ structure [8] with the spontaneous polarization directed along the y axis. Such materials are ferrimagnets (magnetic space group $Pc\underline{2}_1n$) [9, 10] with the ferrimagnetic moment directed along the z axis. The Curie temperature T_C significantly depends not only on the concentration of magnetic iron ions Fe^{3+}, increasing with x, but also on the preparation technique [9–11]. For instance, the Curie temperature of the single crystals grown by the "flux" method is considerably higher than for crystals grown by the floating zone method.

To prepare single crystals with the highest T_C, we applied the flux method. To reduce the possible variations in the basic composition of the grown single crystals, we chose fluxes based on sodium tetramolybdate 90 wt % (Na_2O + $4MoO_3$) + 10 wt % $Ga_{0.5}Fe_{1.5}O_3$. In this case, the iron distribution coefficient between the crystal and the flux is close to unity. Depending on the growth temperature and the additions of bivalent (Co, Ni, Cu, Zn) or trivalent (Cr, Sc, La) metal oxides, T_C of the grown crystals varied in the range from 260 to 345 K. An unexpected fact was that, upon the introduction of bivalent metal oxides into the flux, the electrical

resistivity increased from 10^6–10^7 to 10^{13} Ω cm. Upon the introduction of titanium dioxide (TiO_2), the resistivity decreased to 10^5 Ω cm. The impurities of trivalent metal oxides showed no effect.

The structure of prepared single crystals was monitored by the x-ray method, and the obtained unit-cell parameters were in agreement with the literature data [8, 11]. The fact that the crystal structure is noncentrosymmetric was also confirmed by analyzing the temperature dependences of the damping of elastic vibrations excited by the electrical (sample inside capacitor) and magnetic (sample inside coil) methods in polished spheres with a diameter of 1–2 mm [12]. Figure 1 shows the temperature dependences obtained for the relative amplitudes of piezoelectric (A^{piezo}) and magnetic (A^{mag}) signals, for the reciprocal Q factor Q^{-1} of the piezoelectric signal, the logarithm of resistance log$R$, and the frequency f of the elastic oscillations of one of the samples obtained from the flux with additions of cobalt oxide (Co/Fe = 6 at. %).The magnetic signal disappears in the region of T_C, while the amplitude of the piezoelectric signal rapidly decreases at temperatures above 400 K. The disappearance of the piezoelectric signal is accompanied by the deterioration of the Q factor of elastic vibrations.

We now discuss the optical properties. The linear polarization $P_i(\omega)$ in the electric field $E_j(\omega)$ of the light wave can be written in the form

$$P_i(\omega) = [\alpha_{ij}^{(i)}(\omega) + i\beta_{ij}^{(c)}(\omega) + \gamma_{ijk}^{(c)}(\omega)k_k(\omega)]E_j(\omega), \quad (1)$$

where the tensors $\hat{\alpha}^{(i)}$, $\hat{\beta}^{(c)}$, and $\hat{\gamma}^{(c)}$ describe the optical and magneto-optical susceptibilities and the linear magneto-optical spatial dispersion, respectively. The superscripts (i) and (c) indicate that the tensor is invariant or noninvariant under time reversal, respectively [13]. For the magnetic point group $m'2'm$, the $\alpha_{xx}^{(i)} \neq \alpha_{yy}^{(i)} \neq \alpha_{zz}^{(i)}$ and $\beta_{xy}^{(c)} \neq \beta_{yx}^{(c)}$ components are nonzero. The result that the $\hat{\alpha}^{(i)}$ has three independent tensor components is quite obvious for a biaxial crystal. The fact that $\beta_{xy}^{(c)} \neq \beta_{yx}^{(c)}$ indicates that the spontaneous magneto-optical effect should be observed for the light propagation along the z axis, along which the ferrimagnetic moment is aligned. However, in contrast to the Faraday effect in isotropic media, where the natural waves are circularly polarized, the natural waves propagating along the z axis in orthorhombic crystals are polarized elliptically below T_C. Note that the magnetic symmetry allows for the magnetoelectric effect with the tensor components of the $xy \neq yx$ type, which was observed in [14] and interpreted as the manifestation of the toroidal momentum. The possibility of new nonreciprocal optical effects in $GaFeO_3$ was pointed out in [15]. The observation of the optical magnetoelectric effect was reported in [16].

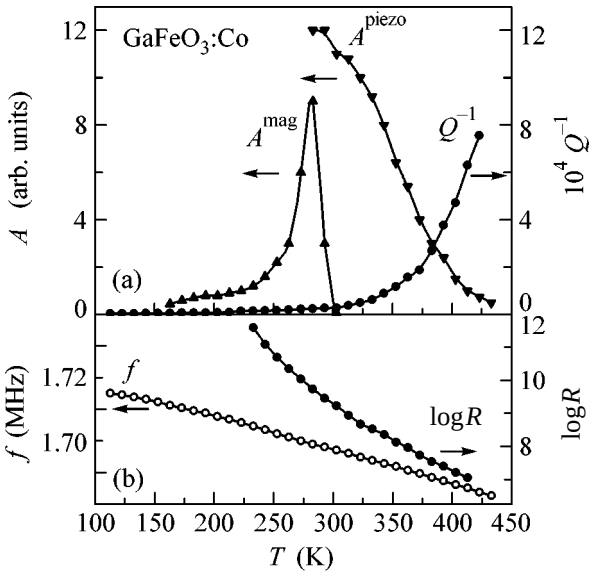

Fig. 1. Temperature dependences of the (a) relative amplitudes of piezoelectric A^{piezo} and magnetic A^{mag} signals, the reciprocal Q factor Q^{-1} of the piezoelectric signal, and (b) logarithm of resistance log$R$ and frequency f of elastic vibrations in the $GaFeO_3$ single crystal prepared from a melt with additions of cobalt oxide.

The expression for the nonlinear polarization $P_i(2\omega)$ can be written in the form

$$P_i(2\omega) = [\chi_{ijk}^{(i)}(\omega) + i\chi_{ijk}^{(c)}(\omega)]E_j(\omega)E_k(\omega), \quad (2)$$

where the tensors $\hat{\chi}^{(i)}$ and $\hat{\chi}^{(c)}$ account for the optical second harmonic generation of the crystalline and magnetic nature, respectively. These tensors have nonzero components of the type [11, 13, 17]

$$\chi_{ijk}^{(i)}\begin{cases} a = yxx, b = yyy, c = yzz, \\ d = xxy = xyx, e = zzy = zyz; \end{cases} \quad (3)$$

$$\chi_{ijk}^{(c)}\begin{cases} A = xxx, B = xyy, C = xzz, \\ D = yyx = yxy, E = zzx = zxz. \end{cases} \quad (4)$$

Note that the occurrence of the magnetic second-harmonic components directly follows from the noncentrosymmetry of the crystal structure. The tensor $\hat{\chi}^{(c)}$ has only odd components in the x indices and is identical to the tensor of the piezomagnetic effect [13], which is probably responsible for the appearance of the magnetic acoustic signal A^{mag} (Fig. 1).

In the general case, the linear and nonlinear properties of transition-metal oxides in the optical range are determined by the electronic transitions in magnetic ions in the crystal field, by the charge-transfer transition, and by interband transitions. In order to reveal the main features of the electronic structure of the multiferroic $Ga_{2-x}Fe_xO_3$, we carried out an ellipsometric study in the range 0.7–5.4 eV for several differently oriented

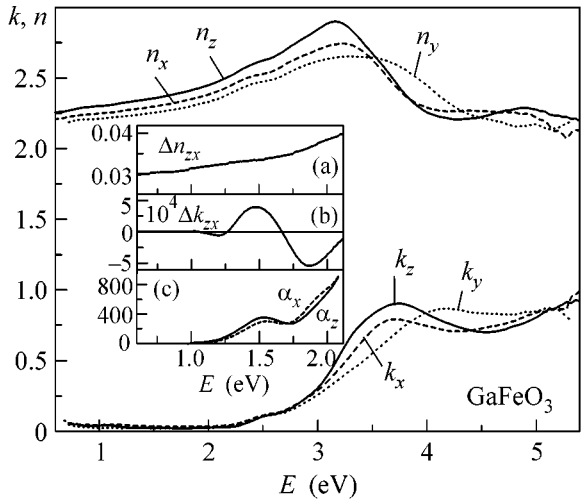

Fig. 2. Absorption coefficients k and refractive indices n vs. the photon energy E for three principal light polarizations. Inset: the spectral dependences of (a) birefringence $\Delta n_{zx} = n_z - n_x$, (b) dichroism $\Delta k_{zx} = k_z - k_x$, as calculated from transmission ellipsometry, and (c) absorption.

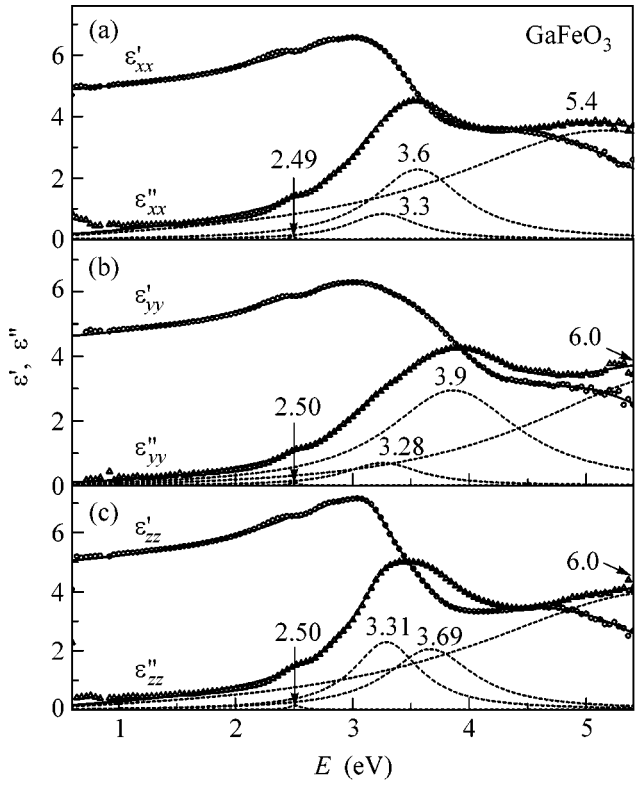

Fig. 3. (Points) Spectral dependences of the dielectric functions ε' and ε" of $GaFeO_3$ for three principal polarizations and (dotted lines) their decomposition into main oscillators. Numerals indicate the positions of the main transitions in electron volts.

$GaFeO_3$ samples. This allowed us to determine the dielectric functions $\varepsilon = \varepsilon' - i\varepsilon''$ for the three principal axes of the orthorhombic crystal (Figs. 2, 3). Figure 2 shows the spectra of the absorption coefficients k_i and refractive indices n_i. Two maxima are clearly seen in the region of weak absorption (inset in Fig. 2). They are typical for the majority of trivalent iron oxides and can reliably be assigned to the localized transitions from the ground $^6A_1$ state to the $^4T_1$ (~1.5 eV) and $^4T_2$ (~2.0 eV) levels [18]. The feature near 1.25 eV is likely due to the splitting of the $^4T_1$ level by the trigonal component arising in the crystal field as a result of displacement of the Fe^{3+} ions along the polar axis y [16]. The feature in the region of 2.5 eV was assigned to the $^6A_1 \longrightarrow {}^4A_1, {}^4E$ transition.

The dielectric functions ε' and ε" and their decomposition in several oscillators are shown in Fig. 3 for the three principal directions. The decomposition is performed in the Lorentz model according to the formula

$$\varepsilon = \varepsilon_0 + bE + \sum \frac{f_j}{E_j^2 - E^2 - iE\gamma_j}, \qquad (5)$$

where the term bE is introduced to take into account the transitions occurring at energies higher than the energy range under study. With the object of revealing trends in the variations of dielectric functions of the $Ga_{2-x}Fe_xO_3$ system with changes in the gallium/iron ratio, the ellipsometric study was carried out for single crystals of the composition $Ga_{0.25}Fe_{1.75}O_3$ that crystallize in the trigonal structure of the α-Fe_2O_3 hematite type. The dielectric functions of this uniaxial material and their decomposition in the main oscillators for two principal light polarizations are shown in Figs. 4b and 4c. The comparison of these results with the dielectric functions for $GaFeO_3$ (Fig. 3) allows the following conclusions to be drawn.

(i) The spectral decomposition for $Ga_{0.25}Fe_{1.75}O_3$ gives a more structured pattern than for $GaFeO_3$. This result is understandable because the iron ions in trigonal $Ga_{0.25}Fe_{1.75}O_3$ are situated in the equivalent crystallographic positions, while, in the orthorhombic $GaFeO_3$, they occupy three nonequivalent octahedral positions [8]. The results of calculation of the electronic structure of the iron ion in the octahedral cluster of oxygen ions in the cubic-field approximation [19] are presented in Fig. 4a.

(ii) An increase in the concentration of iron ions results in a noticeable low-energy shift of the main absorption maximum and an increase in its intensity. In $Ga_{0.25}Fe_{1.75}O_3$, the main maximum is situated near 3.0 eV and has intensity $\varepsilon'' \sim 6.2$ ($E \parallel z$) and 8.2 ($E \perp z$), whereas the main maximum in $GaFeO_3$ is positioned at 3.6 eV ($E \parallel x, z$) and 3.9 eV ($E \perp y$) and has intensity $\varepsilon'' \sim 4.5$–5.

(iii) Noteworthy also is a considerable increase in the intensity of localized $^6A_1 \longrightarrow {}^4A_1, {}^4E$ transitions

near 2.5 eV in $Ga_{0.25}Fe_{1.75}O_3$. This is caused by the strengthening of mixing of the 3*d*-states with the allowed electric-dipole charge-transfer transitions because of their high intensity and proximity to the localized transitions.

The study of spontaneous optical rotation was carried out on a plate 60-μm thick whose normal was directed along the *y* axis. The wave vector was perpendicular to the *x* axis and made an angle $\alpha \sim 20°$ with the *y* axis (the direction of the light beam in the sample was ~10°), and the magnetizing field was directed along the *z* axis. Due to birefringence, the rotation of the polarization plane observed in this geometry is not the true Faraday effect that is determined by the $\beta_{xy} \neq \beta_{yx}$ components. The temperature dependences of the residual rotation angle θ_F of the polarization plane are shown in Fig. 5. The effect disappears at $T \simeq 260$ K, which we identify as the Curie temperature of the sample. The hysteresis loops for θ_F for several temperatures are presented in the inset in Fig. 5.

The second-optical-harmonic generation, which is related to the crystallographic and magnetic contributions by formula (2), was studied on the same sample and in the same geometry as for the Faraday effect. Earlier, the second-harmonic generation was studied only for $GaFeO_3$ crystals prepared by the floating zone method and having $T_C \sim 200$ K [17, 20]. A change in the magnetic contribution to the second-harmonic generation is clearly seen from the temperature dependence of the magnetic contrast $\dfrac{I^{2\omega}(+H) - I^{2\omega}(-H)}{I^{2\omega}(+H) + I^{2\omega}(-H)}$ of the second-harmonic signal (Fig. 5). One can see that the temperature dependences of the linear rotation of the polarization plane and the nonlinear magnetic contrast obey the power law $(1 - T/260.0(4))^{0.37(4)}$; i.e., this sample undergoes transition to the paramagnetic state at $T_C \simeq$ 260 K. The azimuthal dependences for a photon energy of ~1.54 eV are shown in Fig. 6 for the opposite field directions $\pm H \parallel z$ and two polarizations of the second harmonic. Using Eq. (2) and Eqs. (3) and (4) for the tensor components of nonlinear susceptibility and performing appropriate coordinate transformations [21], we arrive at expressions describing the dependences of the second-harmonic intensities on the azimuth φ of pump polarization:

$$I_{\parallel x}^{2\omega} \propto \left|A\cos^2\varphi + (B\sin^2\alpha + C\cos^2\alpha)\sin^2\varphi + d\sin 2\varphi\sin\alpha\right|^2; \quad (6)$$

$$I_{\perp x}^{2\omega} \propto \left|[a\cos^2\varphi + (b\sin^2\alpha + c\cos^2\alpha)\sin^2\varphi + D\sin 2\varphi\sin\alpha]\sin\alpha + [e\sin^2\varphi\sin 2\alpha + E\sin 2\varphi\cos\alpha]\cos\alpha\right|^2. \quad (7)$$

The results of calculations by formulas (6) and (7) are shown in Fig. 6 by hatched regions. When calculating,

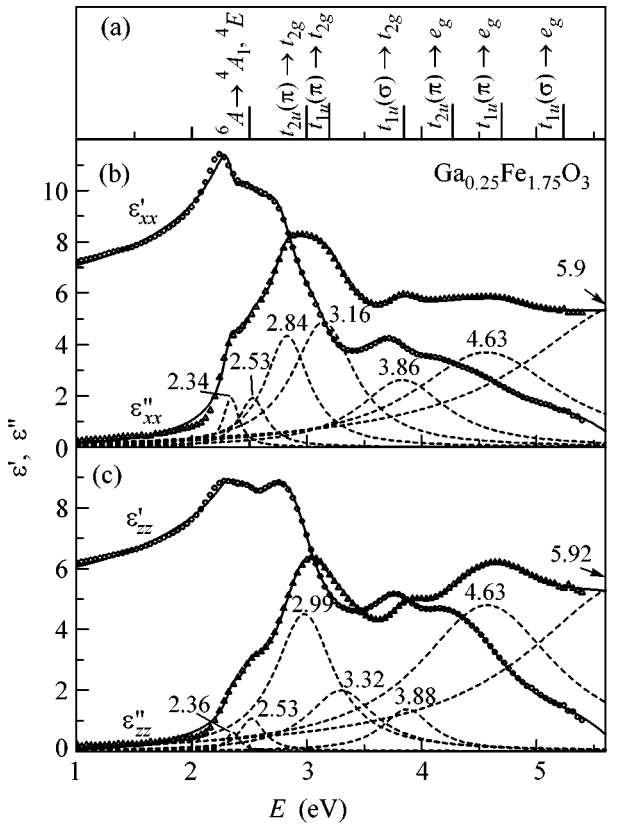

Fig. 4. (a) Main transitions in iron oxides calculated in the cubic-field approximation [19] and (b), (c) (points) spectra of the dielectric functions ε' and ε" of the uniaxial crystal $Ga_{0.25}Fe_{1.75}O_3$ and (dotted lines) their decomposition into main oscillators for the principal light polarizations.

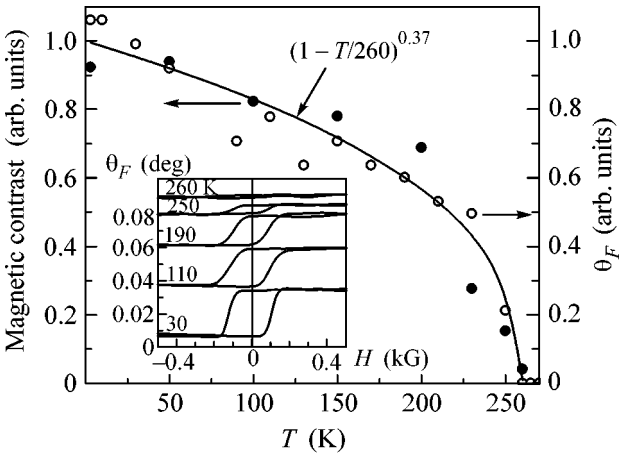

Fig. 5. Temperature dependences of (open circles) the rotation θ of the polarization plane and (closed circles) the magnetic contrast of the second harmonic. The solid line is the function $(1 - T/260.0(6))^{0.37(4)}$. Inset: the field dependences of the rotation of the polarization plane for several temperatures.

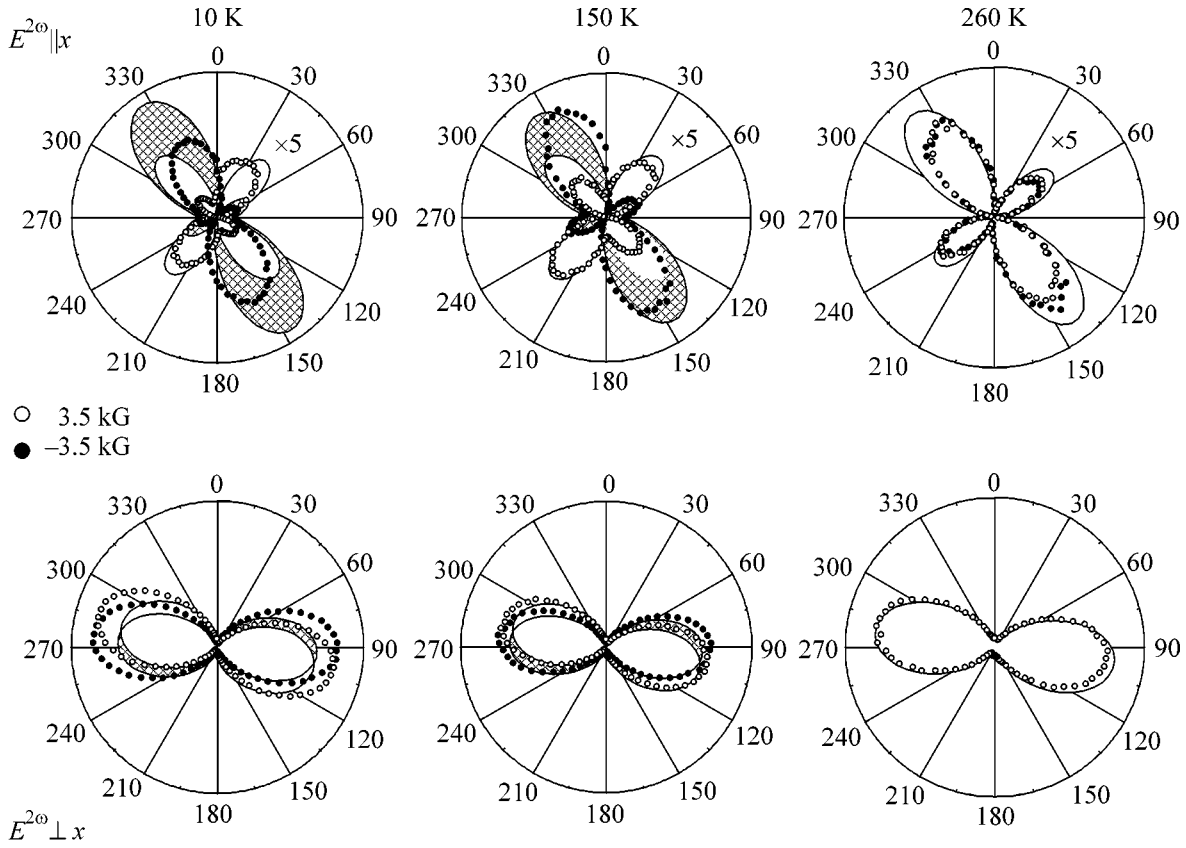

Fig. 6. Azimuthal dependences of second-harmonic intensities for the $E^{2\omega} \parallel x$ and $E^{2\omega} \perp x$ polarizations in a field $\pm H \parallel z$ for several temperatures. The solid lines are calculations by formulas (6) and (7).

we took into account a small misorientation of the crystal axes about the laboratory coordinate systems. We attribute the discrepancy between the experimental and calculated dependences to the disregard of the influence of strong birefringence.

In summary, the optical and magneto-optical properties of a noncentrosymmetric orthorhombic orthoferrite $GaFeO_3$ that has T_C in the range 260–345 K and is grown by the flux method have been studied in this work. The dielectric functions for the three principal crystallographic axes have been obtained over a broad spectral range. The comparison of these spectra with the spectra of trigonal $Ga_{0.25}Fe_{1.75}O_3$ has shown that an increase in the concentration of the Fe^{3+} ions gives rise to the low-energy shift of the fundamental absorption edge. Since the iron ions in orthorhombic $GaFeO_3$ occupy three nonequivalent crystallographic positions, the pattern of charge-transfer transitions is more pronounced in trigonal $Ga_{0.25}Fe_{1.75}O_3$, where Fe^{3+} ions occupy only equivalent positions. The study of the magneto-optical Faraday effect and second-harmonic generation in a magnetic field allows for the determination of the transition law to the paramagnetic state for $GaFeO_3$.

We are grateful to A.V. Kimel, V.V. Pavlov, and P.A. Usachev for stimulating discussions. This work was supported by the Russian Foundation for Basic Research and the European Program DYNAMICS.

REFERENCES

1. K. Aizu, Phys. Rev. B **2**, 754 (1970).
2. G. A. Smolenskiĭ and I. E. Chupis, Usp. Fiz. Nauk **137**, 415 (1982) [Sov. Phys. Usp. **25**, 475 (1982)].
3. H. Schmid, in *Introduction to Complex Mediums for Optics and Electromagnetics*, Ed. by W. S. Weigloger and A. Lakhtakia (SPIE Press, Bellingham, 2003), pp. 167–195.
4. T. Kimura, T. Goto, H. Shintani, *et al.*, Nature **429**, 392 (2004).
5. J. Wang, J. B. Neaton, H. Zheng, *et al.*, Science **299**, 1719 (2003).
6. M. Fiebig, V. V. Pavlov, and R. V. Pisarev, J. Opt. Soc. Am. B **22**, 96 (2005).
7. J. P. Remeika, J. Appl. Phys. **31**, 263S (1960).
8. S. C. Abrahams, J. M. Reddy, and J. L. Bernstein, J. Chem. Phys. **42**, 3957 (1965).
9. R. B. Frankel, N. A. Blum, S. Foner, *et al.*, Phys. Rev. Lett. **15**, 958 (1965).

10. B. F. Levin, C. H. Nowlin, and R. V. Jones, Phys. Rev. **174**, 571 (1968).
11. T. Arima, D. Higashiyama, Y. Kaneko, *et al.*, Phys. Rev. B **70**, 064426 (2004).
12. R. G. LeCraw and R. L. Comstock, in *Physical Acoustics. Principles and Methods*, Ed. by W. P. Mason (Academic, New York, 1965; Mir, Moscow, 1968), Vol. 3, Part B.
13. R. R. Birss, *Symmetry and Magnetism* (North-Holland, Amsterdam, 1966).
14. Yu. F. Popov, A. M. Kadomtseva, G. P. Vorob'ev, *et al.*, Zh. Éksp. Teor. Fiz. **114**, 263 (1998) [JETP **87**, 146 (1998)].
15. A. K. Zvezdin, Kratk. Soobshch. Fiz., No. 6, 35 (2000).
16. J. H. Jung, M. Matsubara, T. Arima, *et al.*, Phys. Rev. Lett. **93**, 037403 (2004).
17. K. Eguchi, Y. Tanabe, T. Ogawa, *et al.*, J. Opt. Soc. Am. B **22**, 128 (2005).
18. R. V. Pisarev, Fiz. Tverd. Tela (Leningrad) **7**, 207 (1965) [Sov. Phys. Solid State **7**, 158 (1965)].
19. A. I. Likhtenshteĭn, A. S. Moskvin, and V. A. Gubanov, Fiz. Tverd. Tela (Leningrad) **24**, 3596 (1982) [Sov. Phys. Solid State **24**, 2049 (1982)].
20. Y. Ogawa, Y. Kaneko, J. P. He, *et al.*, Phys. Rev. Lett. **92**, 047401 (2004).
21. V. N. Gridnev, V. V. Pavlov, R. V. Pisarev, *et al.*, Phys. Rev. B **63**, 184407 (2001).

Translated by V. Sakun

JETP Letters, Vol. 81, No. 9, 2005, pp. 458–461. Translated from Pis'ma v Zhurnal Éksperimental'noĭ i Teoreticheskoĭ Fiziki, Vol. 81, No. 9, 2005, pp. 574–577.

Scattering Involving LO Phonons in Tunneling to the 2D Electron System of a Delta Layer

I. N. Kotel'nikov* and S. E. Dizhur

Institute of Radio Engineering and Electronics, Russian Academy of Sciences, ul. Mokhovaya 17/7, Moscow, 125009 Russia

** e-mail: igor@mail.cplire.ru*

Received March 24, 2005

Tunneling to both one and two or three subbands of the 2D electron system of a delta-doped layer is observed in Al/δ-GaAs structures. The energy positions of 2D subbands in one sample are varied due to the diamagnetic shift or persistent tunneling photoconductivity. The change of the sign of a step in tunneling conductivity is observed at the threshold of the emission of an LO phonon when a successive subband is involved in tunneling. An increase in conductivity (positive step) is observed for inelastic intrasubband electron–phonon scattering. A decrease in conductivity (negative step) is observed when the ordinary processes of inelastic tunneling are supplemented by intersubband transitions of electrons that have tunneled in 2D electron systems with the emission of an LO phonon. © *2005 Pleiades Publishing, Inc.*

PACS numbers: 73.20.Mf, 73.20.At, 73.40.Gk

Recent experiments show that the interaction between electrons and LO phonons in GaAs 2D electron systems leads to appreciable intersubband polaron effects. In optical experiments on AlGaAs/GaAs structures with two quantum wells separated by a barrier transparent for tunneling [1, 2], bound electron–LO-phonon modes involving intersubband transitions were observed. The presence of these modes was indicated by the effect of "anticrossing" of terms that was found in [2]. Pinning and anticrossing, which are characteristic of an intersubband polaron, were previously observed for 2D levels in the quantum well of the delta layer in the tunneling spectra of the Al/δ-GaAs structure [3]. The LO-phonon lines detected in these structures for bias $U = \pm\varepsilon_{LO}/e$, where $\varepsilon_{LO} = 36.5$ meV is the LO-phonon energy in GaAs, changed noticeably when tuning intersubband energies near the polaron resonance [4]. It was also shown that, as the filling of levels in the 2D electron system of the delta layer increases, a new type of phonon lines is manifested [5] due to a decrease in the tunneling conductivity when reaching the emission threshold for an LO phonon.

Intersubband interaction involving LO phonons was considered as the most probable cause of the appearance of the new type of lines [5]. It remained unclear which parameters of the spectrum of the 3D electron system determine this appearance. The enhancement predicted in [6] for plasmon–phonon modes due to the closeness of intersubband energies in δ-GaAs to ε_{LO} can also affect the shape of the phonon line. In this work, we try to determine a mechanism of electron–phonon interaction that is responsible for a decrease in conductivity over the threshold of LO-phonon emission when tunneling to the 2D electron system.

We study Al/δ-GaAs structures manufactured by molecular beam epitaxy at the Institute of Radio Engineering and Electronics, Russian Academy of Sciences [3]. The distance between the Al/GaAs interface and the δ-doping (Si) layer is equal to about 20 nm. The tunneling spectra of the Al/δ-GaAs transitions are measured at a temperature of 4.2 K. The U dependence of the logarithmic derivative $S = d\ln\sigma/dU$ of the tunneling conductivity $\sigma = dI/dU$ is used as the tunneling spectrum. This choice provides a common scale for the tunneling characteristics of transitions with different σ values. We take three samples (*1*, *2*, and *3*), in which an electron tunneling to the 2D electron system for $U = -36.5$ mV can enter one subband and two or three subbands. In this case, the Fermi level $E_{F\,m}$ of the metal is higher than the Fermi level $E_{F\delta}$ in the delta layer by ε_{LO}. The energies $E_{iF} = E_i - E_{F\delta}$ of the three lower subbands for these samples as measured from $E_{F\delta}$ can be determined [3] from the tunneling spectra shown in Fig. 1. As is known, the tunneling conductivity from 3D to 2D states is proportional to the density of states in the 2D electron system, and the positions of smooth minima in curves $S(U) = d\ln\sigma/dU$ correspond to the subband energies in the delta layer [3]. At a temperature of 4.2 K, the energies of the first three levels are $E_{0F} = -19$, –21, and –61 meV; $E_{1F} = 36$, 18, and –7.5 meV; and $E_{2F} = 76$, 44, and 28 meV for samples *1*, *2*, and *3*, respectively (see Fig. 1).

In order to determine the background curve and to separate the optical phonon lines from the tunneling spectra, we use the polynomial approximation of the

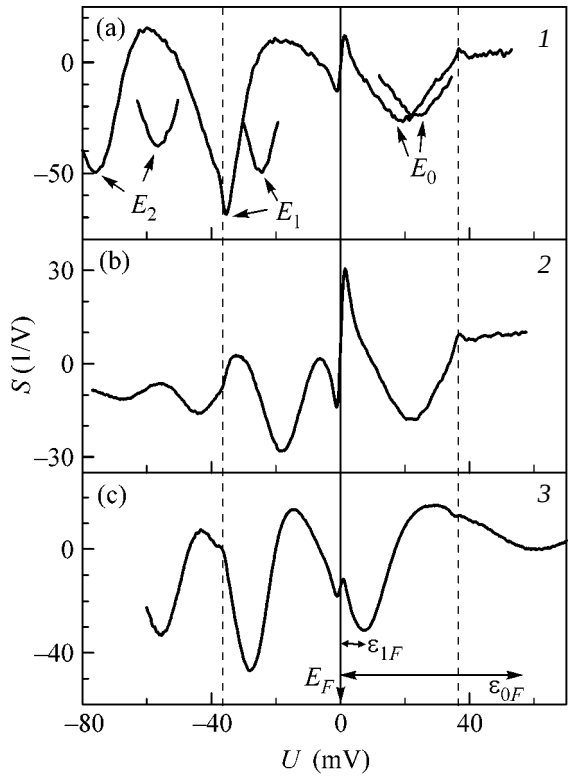

Fig. 1. Tunneling spectra $S = d\ln\sigma/dU$ for three Al/δ-GaAs samples. $U < 0$ corresponds to tunneling to the δ layer. The arrows show the positions of two-dimensional subbands in the tunneling spectra. Thin lines in panel (a) correspond to the positions of subbands after the illumination of sample *1* by the radiation of an GaAs light diode to the saturation of the effect of persistent tunneling photoconductivity. The dashed vertical straight lines indicate the bias $|U| = 36.5$ mV, which corresponds to the threshold of the LO-phonon emission in tunneling.

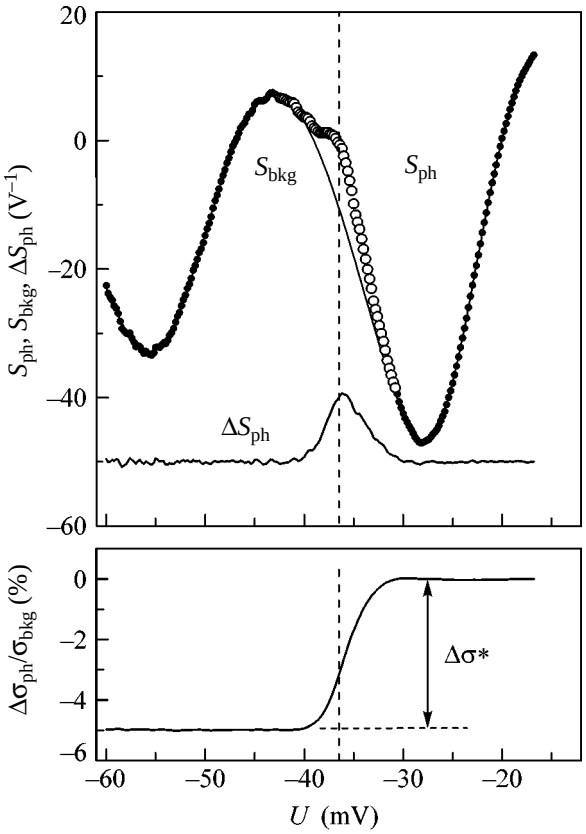

Fig. 2. Separation of the phonon line from the tunneling spectrum of sample *3* shown in Fig. 1c. Open circles indicate the range that is excluded from the $S_{ph}(U)$ curve when determining the background $S_{bkg}(U)$. The lower panel shows the relative tunneling conductivity $\Delta\sigma_{ph}/\sigma_{bkg}(U)$ obtained by integrating the phonon line $\Delta\sigma_{ph}(U) = S_{ph} - S_{bkg}$ with respect to U. The negative step $\Delta\sigma^*$ in the tunneling conductivity is also shown.

spectrum S_{ph} near the phonon singularity (Fig. 2). The part of the $S_{ph}(U)$ curve that contains the singularity (displacement range ±6 mV from the center of the line for $U = -36.5$ mV) is excluded from the approximation range. Then, the background curve S_{bkg} is obtained by the least-squares method, as is shown in Fig. 2. The alternative cubic spline determination of S_{bkg} that was proposed in [7] was shown to provide close results. The phonon line ΔS_{ph} is separated by the difference $\Delta S_{ph} = S_{ph} - S_{bkg} = d(\ln\sigma_{ph} - \ln\sigma_{bkg})/dU$. Assuming that the tunneling conductivity $\sigma_{ph} = \Delta\sigma_{ph} + \sigma_{bkg}$, where $\Delta\sigma_{ph} \ll \sigma_{bkg}$, is change induced in conductivity by the electron–phonon interaction, we obtain $\Delta S_{ph} \simeq d(\Delta\sigma_{ph}/\sigma_{bkg})/dU$. Hence, the integration of ΔS_{ph} with respect to dU yields the relative change $\Delta\sigma_{ph}/\sigma_{bkg}$ in the tunneling conductivity near the phonon line (lower line in Fig. 2).

The phonon line for sample *3* in Fig. 2 corresponds to unusual processes of electron–phonon interaction in tunneling, because conductivity decreases at the threshold $|eU| = \varepsilon_{LO}$ [5]. This behavior corresponds to a negative step in the U dependence of $\Delta\sigma_{ph}/\sigma_{bkg}$ (see Fig. 2, where $\Delta\sigma^* < 0$ is the step value). As is known (see, e.g., [8]), inelastic processes with the emission of an LO phonon lead to an increase in conductivity above the threshold, and $\Delta\sigma^* > 0$ in this case. Such lines were observed in samples *1* and *2* (see Fig. 1). In what follows, we will be interested in the dependence of the step height $\Delta\sigma^*$ in the tunneling conductivity on the position of the bottom of the subband closest to the energy $E_{F\delta} + \varepsilon_{LO}$. We will show that the change in the sign of $\Delta\sigma^*$ can be observed in a sample by varying the positions of 2D subbands by external actions.

As was shown in [9], the energy positions of 2D subbands in the delta layer can be changed due to the effect of persistent tunneling photoconductivity (PTPC). After illumination of the sample by the photodiode (for time t), unoccupied levels ($E_i - E_{F\delta} > 0$) are concentrated near the ground state. In particular, according to Fig. 1, the bottom of the subband E_{1F} is located at a distance ε_{LO} from $E_{F\delta}$, i.e., at the threshold

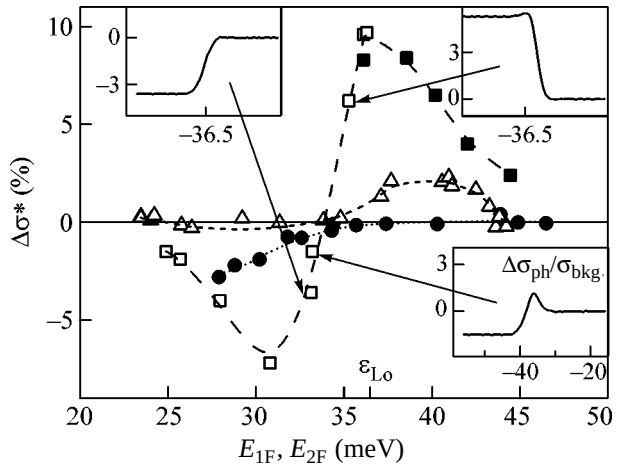

Fig. 3. Step height $\Delta\sigma^*$ in tunneling conductivity vs. the energy E_{iF}. The squares are $\Delta\sigma^*(E_{1F})$ for sample *1*. The insets show the $\Delta\sigma_{ph}/\sigma_{bkg}(U)$ dependences at the characteristic points of the $\Delta\sigma^*(E_{1F})$ curve for this sample. The triangles are $\Delta\sigma^*(E_{2F})$ for sample *2*. In both samples, the positions of the subbands are varied due to the light-diode illumination (persistent tunneling conductivity regime). The closed circles (squares) correspond to sample *3* (*1*), where E_{2F} (E_{1F}) increases due to the diamagnetic shift in the magnetic field $B_{\|}$.

of the phonon emission, and the tunneling current for $U = -36.5$ mV is determined primarily by current to the subband E_0. After illumination to saturation of the PTPC effect, $E_{1F}(t)$ decreases below the threshold to 22 meV (see Fig. 1) and electrons tunnel from the metal to two subbands of the 2D electron system.

The dependence of $\Delta\sigma^*$ on $E_{1F}(t)$ for sample *1* is shown in Fig. 3. It is seen that the step in conductivity becomes negative when $E_{1F}(t)$ decreases below the emission threshold for an optical phonon. The same, but weaker, effect is observed in sample *2* for the subband E_2, where $E_{2F}(t = 0) > \varepsilon_{LO}$. A similar dependence of $\Delta\sigma^*$ on $E_{2F}(t)$ for sample *2* is also shown in Fig. 3. In this case, for $E_{2F}(t) < \varepsilon_{LO}$, electrons tunnel to three subbands of the 2D electron system. However, E_{iF} at which the step sign changes is close to ε_{LO} for both samples. The subband E_2 in sample *3* is located below the threshold (see Fig. 1c), and here $\Delta\sigma^*$ is negative. The presence of the magnetic field $B_{\|}$ parallel to the delta layer leads to the displacement (due to the diamagnetic shift) of the level E_2 towards higher energies. When $E_{2F}(B_{\|})$ increases to ε_{LO}, the step height $\Delta\sigma^*$ decreases to zero (see Fig. 3).

The above results show that the new phonon line with $\Delta\sigma^* < 0$ appears in the tunneling spectrum of the Al/δ-GaAs structure when a successive subband of the 2D electron system—E_1 for sample *1* or E_2 for samples *2* and *3*—is involved in the tunneling process. In this case, electrons in the 2D electron system can pass from this subband to unoccupied states above the Fermi level of the lower subband, with the emission of an LO phonon. This is the subband E_0 for the first two samples, because the intersubband distance in sample *2* is $E_{21} < \varepsilon_{LO}$. In sample *3*, transitions can occur to both E_0 and E_1, which is below the Fermi level for $B_{\|} = 0$.

The sign change observed in the conductivity step can be explained in the model proposed in [10]. In this model, the electron–phonon interaction is described by the electron self-energy $\Sigma = \Sigma_R + i\Sigma_I$. The real part Σ_R of this function is the energy that the electron gains in the process of interaction with a phonon, and the imaginary part Σ_I is related to the electron–phonon scattering frequency. As was shown in [10], Σ_I makes a step contribution to the tunneling conductivity (for $|eU| = \varepsilon_{LO}$).

If electron–phonon interaction is localized in one of the electrodes of the tunnel junction (in the 2D electron system in our case), the Σ_I contribution is a decreasing (negative) step in conductivity ($\Delta\sigma^* < 0$). In [10], such behavior was attributed to an increase in reflectivity from the electrode–barrier interface, when the electron tunnels to a dissipative medium. The dissipative medium is the 2D electron system: the electron that has tunneled to, e.g., the E_1 subband can emit a phonon and pass to the lower subband E_0. If the interaction region includes the tunneling barrier (the GaAs layer between the metal and delta layer), the Σ_I contribution corresponds to an increasing step in conductivity ($\Delta\sigma^* > 0$). This case corresponds to the opening of a new (inelastic) channel for electron tunneling to the 2D electron system.

In the simplest case, that of the electron tunneling to one subband E_0 for $eU = -\varepsilon_{LO}$, only intrasubband inelastic scattering with the emission of an LO phonon is possible. These processes can occur in both the tunneling barrier and the 2D electron system (see Fig. 4a). Therefore, the contribution $\Delta\sigma_{intra}$ from inelastic electron–phonon scattering to the tunneling conductivity must correspond to a positive step. In this case, $\Delta\sigma_{ph}/\sigma_{bkg}$ can be written as $\Delta\sigma_{intra}/\sigma_{bkg}$, where $\Delta\sigma_{intra} > 0$. When the second subband E_1 (E_1–$E_0 > \varepsilon_{LO}$) is involved in the tunneling charge transfer (see Fig. 4b), the contribution $\Delta\sigma_{inter} < 0$ from intersubband transitions E_{01} in the 2D electron system is added to conductivity. In this case, relative conductivity is determined by both contributions: $\Delta\sigma_{ph}/\sigma_{bkg} = (\Delta\sigma_{intra} + \Delta\sigma_{inter})/\sigma_{bkg}$. When $|\Delta\sigma_{inter}|$ becomes larger than $\Delta\sigma_{intra}$, $\Delta\sigma^*$ becomes negative, which is the case in experiment (see the curve for sample *1* in Fig. 3).

In conclusion, we emphasize that the observation of the change of the step sign in the tunneling conductivity at the threshold of the LO-phonon emission was possible due to a high intersubband energy ($E_{01} > \varepsilon_{LO}$) for the occupied and unoccupied levels in the delta layer. This effect is most pronounced for the transition from tunneling to one subband to tunneling to two subbands of the 2D electron system (sample *1* in Figs. 1a and 3). In

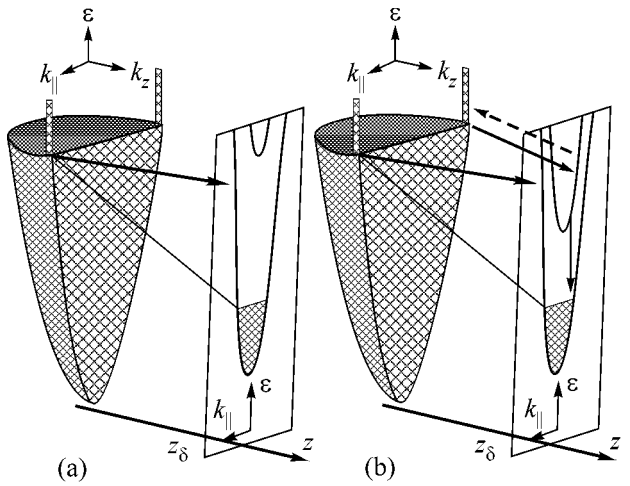

Fig. 4. Scheme of tunneling to (a) one and (b) two subbands of the 2D electron system. In the latter case, intersubband transitions to the 2D electron system with the emission of an LO phonon are added to intrasubband inelastic processes involving LO phonons.

addition, as is seen in the $\Delta\sigma^*(E_{2F})$ curves in Fig. 3, $\Delta\sigma_{intra}$ and $\Delta\sigma_{inter}$ apparently depend on the spectral parameters and screening effects in the 2D electron system. Quantitative comparison with the model requires calculation of intrasubband and intersubband contributions to the phonon line shape. Unfortunately, such calculations have not yet been performed for the 2D electron system. However, the change of the step sign in tunneling conductivity that is found in this work corroborates the electron–phonon interaction model of tunneling to the 2D electron system. We emphasize that, in addition to the Σ_I contribution, a peak must be observed in $\Delta\sigma_{ph}/\sigma_{bkg}(U)$ at $eU = -\varepsilon_{LO}$. This peak is associated with the logarithmic singularity in the real part Σ_R of the self-energy [8, 10] and is clearly seen in Fig. 3 when the conductivity step height decreases almost to zero (see the lower right inset in Fig. 3).

We are grateful to S.N. Artemenko, V.A. Volkov, and A.Ya. Shul'man for stimulating discussions, to Yu.V. Fedorov and A.S. Bugaev for preparing samples, and to N.A. Mordovets and E.M. Dizhur for assistance in measurements and data processing. This work was supported in part by the Russian Foundation for Basic Research and the Branch of General Physics and Astronomy, Russian Academy of Sciences (programs of fundamental research).

REFERENCES

1. H. C. Liu, I. W. Cheung, A. J. SpringThorpe, *et al.*, Appl. Phys. Lett. **78**, 3580 (2001).
2. H. C. Liu, C. Y. Song, Z. R. Wasilewski, *et al.*, Phys. Rev. Lett. **90**, 077402 (2003).
3. I. N. Kotel'nikov, V. A. Kokin, Yu. V. Fedorov, *et al.*, Pis'ma Zh. Éksp. Teor. Fiz. **71**, 564 (2000) [JETP Lett. **71**, 387 (2000)].
4. S. E. Dizhur, I. N. Kotel'nikov, and F. V. Shtrom, in *Proceedings of 26th International Conference on the Physics of Semiconductors, Edinburgh, Scotland, UK* (2002); Inst. Phys. Conf. Ser. **171**, 158 (2002).
5. I. N. Kotel'nikov and S. E. Dizhur, in *Proceedings of 12th International Symposium on Nanostructures, St. Petersburg, Russia, 2004* (Ioffe Physicotechnical Inst., St. Petersburg, 2004), p. 366.
6. G.-Q. Hai, N. Studart, and G. E. Marques, Phys. Rev. B **55**, 1554 (1997).
7. E. M. Dizhur, A. N. Voronovskiĭ, A. V. Fedorov, *et al.*, JETP Lett. **80**, 433 (2004).
8. E. L. Wolf, *Principles of Electron Tunneling Spectroscopy* (Oxford Univ. Press, Oxford, 1985; Naukova Dumka, Kiev, 1990).
9. S. E. Dizhur, I. N. Kotel'nikov, V. A. Kokin, and F. V. Shtrom, Phys. Low-Dimens. Semicond. Struct. **11/12**, 233 (2001).
10. J. A. Appelbaum and W. F. Brinkman, Phys. Rev. B **2**, 907 (1970).

Translated by R. Tyapaev

JETP Letters, Vol. 81, No. 9, 2005, pp. 462–466. Translated from Pis'ma v Zhurnal Éksperimental'noĭ i Teoreticheskoĭ Fiziki, Vol. 81, No. 9, 2005, pp. 578–582.

Observation of Commensurability Oscillations of Thermopower in an Antidot Lattice

A. G. Pogosov, M. V. Budantsev, R. A. Lavrov, A. E. Plotnikov, A. K. Bakarov, and A. I. Toropov

Institute of Semiconductor Physics, Siberian Division, Russian Academy of Sciences, Novosibirsk, 630090 Russia
e-mail: pogosov@isp.nsc.ru

Received March 24, 2005

Commensurability oscillations of thermopower in a square antidot lattice are observed. The oscillations are attributed to the geometrical resonances of the classical electron motion in a magnetic field and are much more pronounced than the corresponding magnetoresistance oscillations. The off-diagonal component of the thermopower tensor (the Nernst–Ettingshausen effect) changes sign at resonances. Additional measurements of magnetoresistance verify the correctness of the method used for thermopower measurements and provide information on the temperature distribution in the sample. © *2005 Pleiades Publishing, Inc.*

PACS numbers: 73.23.Ad, 73.50.Jt, 73.50.Lw

A periodic lattice of artificial circular scatterers (antidots) in a two-dimensional (2D) electron gas with a high mobility of charge carriers is an example of the solid-state electron Sinai billiards. The classical motion of electrons in such billiards can be considered ballistic and described in terms of the dynamical chaos theory. The commensurability oscillations of magnetoresistance, which are experimentally observed in antidot lattices in magnetic fields when the cyclotron radius of an electron is commensurable with the lattice period or some other characteristic size of the lattice (geometrical resonances) [1–3], reflect the fundamental property of dynamical chaos, namely, the presence of stability regions in the phase space [3–5]. The presence of stable regular trajectories of electrons also leads to some other effects observed in experiments and related to semiclassical electron transport, such as the nonlocal [6] and nonlinear [7] effects. The classical chaos also manifests itself in the phenomena caused by quantum interference, for example, the weak localization [8] and the Aharonov–Bohm effect [9, 10]. These observations called for a revision of the theories describing the quantum corrections to conductivity in systems with dynamical chaos [11].

Until the present time, the transport properties of electron billiards were mainly studied on the basis of magnetoresistance measurements, whereas the other kinetic coefficient, namely, the thermopower, was given much less attention. However, the thermopower, being related to the derivative of conductivity with respect to energy, gives additional information on the transport phenomena in such systems and also reveals some new aspects of dynamical chaos that cannot be detected by magnetoresistance measurements. This was successfully demonstrated in the recent study of mesoscopic fluctuations of thermopower in an open (with a conductance $\gg e^2/h$) antidot lattice [12]. In closed systems (with a conductance $\sim e^2/h$), the thermopower was studied for quantum point contacts [13], quantum dots [14], and nanostructures with a Coulomb blockade [15, 16]. One of the recent papers [17] considers the thermopower of a high-mobility 2D electron gas in weak magnetic fields. In our previous paper [18], we studied the thermopower of a multiprobe ballistic conductor in the form of a caterpillar-like Sinai billiard with the use of the Landauer–Büttiker formalism generalized to the case of thermomagnetic phenomena.

In the present paper, we report on an experimental study of the diffusion thermopower in a two-dimensional square lattice of antidots. The lattice was fabricated on the basis of a 2D electron gas with electron density $N_s = (2–5) \times 10^{11}$ cm^{-2} and mobility $\mu = (5–7) \times 10^5$ cm^2/V s in a GaAs/AlGaAs heterojunction by electron lithography and subsequent plasma etching. The lattice, which had a period $d = 0.9$ μm and an antidot radius $a = 0.2–0.3$ μm, covered a Hall bar with the dimensions $L \times W = 9 \times 6$ μm^2.

To measure the thermopower, we used the heating current method: a heater in the form of a conducting channel 12 μm in length and 2 μm in width was adjacent to the Hall bar (see the inset in Fig. 1), and a heating current of frequency f was passed through it. In such a system, the Joule heat generated by the alternating current locally raises the temperature of the electron gas (the electron–electron collision time is much smaller than electron–phonon collision time), and an electron temperature gradient oscillating with a frequency of $2f$ occurs along the sample. Hence, the voltage drop measured at this frequency is proportional to

the thermopower of the antidot lattice. This method measures the diffusion component of the thermopower (without the phonon drag contribution), because only the electron temperature increases while the temperature of the phonon subsystem remains virtually unchanged [19].

In this study, we investigate both diagonal and off-diagonal (the Nernst–Ettingshausen effect) components of the thermopower tensor. For additional magnetoresistance measurements, we used the same Hall bar.

The experimental dependences of magnetoresistance and thermopower measured for a sample with electron density $N_1 = 3.4 \times 10^{11}$ cm^{-2} at $T = 1.7$ K are shown in Fig. 1. The curve representing ρ_{xx} exhibits a commensurability peak at $B \approx 0.21$ T, which is accompanied by a small feature in ρ_{xy}. The peak corresponds to the main commensurability condition $2R_c \approx d$, where R_c is the cyclotron radius. In weaker magnetic fields $B <$ 0.1 T, one more peak is observed: this peak is related to the electron trajectories in the channel that are broken by a magnetic field [4, 6, 20]. Both components of the thermopower tensor $\hat{S}$ also exhibit commensurability oscillations, which are more pronounced than the corresponding features of magnetoresistance. The strongest anomalies (with a change of sign) are observed in S_{xy} in magnetic fields corresponding to the peaks of ρ_{xx}.

It is well known that the thermopower is related to the derivative of conductivity (resistivity) with respect to energy according to the Mott relation, which can be represented in the form

$$\hat{S} = \frac{\pi^2 k^2 T}{3e}\hat{\rho}\frac{d\hat{\rho}^{-1}}{dE}, \quad (1)$$

where k is the Boltzmann constant, e is the elementary charge, $\hat{\rho}$ is the resistivity tensor, and the derivative is taken at the Fermi energy. In its turn, the derivative of resistivity with respect to energy can be expressed through the derivative with respect to magnetic field, as in [18]. Indeed, in the general form, the resistivity can be obtained from the Kubo formula [21]:

$$\sigma_{\alpha\beta} = e^2\nu\int_0^\infty e^{-t/\tau}\langle v_\alpha(t)v_\beta(0)\rangle dt. \quad (2)$$

Here, τ is the relaxation time in the system without antidots and ν is the two-dimensional density of states. In the presence of the antidot lattice with radius a and period d, we obtain the following parametric formula for the resistivity:

$$\rho_{\alpha\beta} = \frac{h}{e^2}\frac{1}{k_F d}F_{\alpha\beta}\left(\frac{R_c}{d}, \frac{a}{d}, \frac{l}{d}\right), \quad (3)$$

where $F_{\alpha\beta}$ is a dimensionless function, l is the mean free path due to residual impurities, and k_F is the Fermi wave vector. Taking into account that l does not depend on energy and assuming that a also does not depend on energy (the hard wall model), we can represent the derivative of resistivity with respect to energy as

$$\frac{d\hat{\rho}}{dE} = \frac{\partial\hat{\rho}}{\partial R_c}\frac{\partial R_c}{\partial E} + \frac{\partial\hat{\rho}}{\partial k_F}\frac{\partial k_F}{\partial E} = -\frac{1}{2E_F}\left(\frac{\partial\hat{\rho}}{\partial B}B + \hat{\rho}\right). \quad (4)$$

Substituting Eq. (4) into Eq. (1), we obtain

$$\hat{S} = \frac{\pi^2}{6}\frac{k}{e}\frac{kT}{E_F}\frac{d\ln(\hat{\rho}B)}{d\ln B}. \quad (5)$$

This expression allows us to compare the experimentally measured thermopower with the thermopower calculated from the experimental magnetic-field dependence of the resistivity tensor. The comparison is displayed in Fig. 2, where the dotted line represents the dependence calculated from the measured $\rho_{xx}(B)$ and $\rho_{xy}(B)$ using Eq. (5). In the case of $S_{xx}(B)$, the measured and calculated values of the thermopower in the vicinity of the main commensurability peak qualitatively coincide. In the case of the off-diagonal component S_{xy} of the thermopower tensor, the calculated and measured dependences prove to be qualitatively different. This means that the hard wall model is inapplicable in the case under consideration. A possible origin of the discrepancy may be the dependence of the antidot radius on energy because of the energy dependence of the thickness of the depletion layer forming the antidot

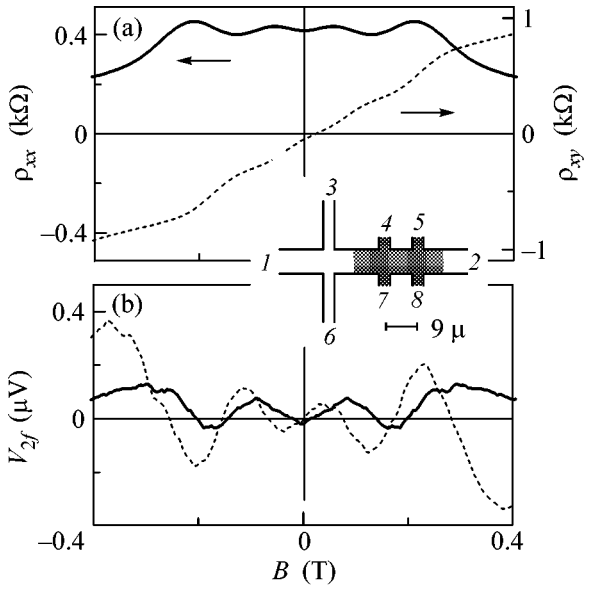

Fig. 1. (a) Magnetic-field dependence of the (solid line) diagonal and (dotted line) off-diagonal components of the magnetoresistance tensor (the bias current is $I_{12} = 0.1$ μA and $f = 7$ Hz). (b) Magnetic-field dependence of (solid line) the longitudinal thermopower measured between probes *7* and *8* and (dotted line) the transverse thermopower measured between probes *4* and *7* at a frequency of $2f$ (the heating current is $I_{36} = 1$ μA and $f = 7$ Hz). The inset shows the geometry of the experimental sample.

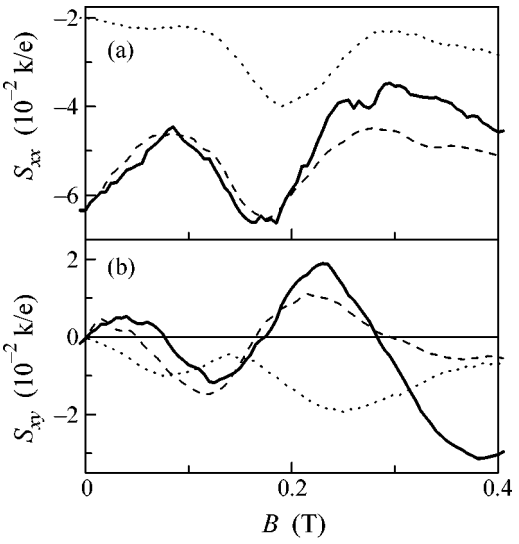

Fig. 2. (a) Diagonal and (b) off-diagonal components of the thermopower tensor (solid line) obtained from direct measurements, (dashed line) calculated using Eq. (1) from the magnetoresistance tensors $\hat{\rho}_1$ and $\hat{\rho}_2$ that were measured for two states of the sample with close electron density values, and (dotted line) calculated using Eq. (5) from the derivative of $\hat{\rho}(B)$ with respect to magnetic field.

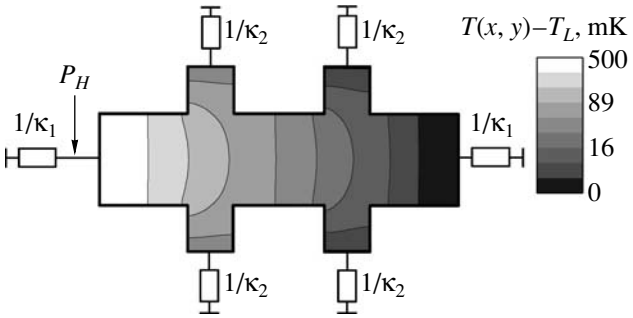

Fig. 3. Equivalent thermal circuit and the temperature distribution (on a logarithmic scale) in the sample region occupied by antidots at $B = 0$ with a heating current applied to the sample. The difference $T(x, y) - T_L$ decreases from 500 mK near the heater (probes *3*–*6*, see the inset in Fig. 1) to 6 mK (probe *2*); $P_H = 2 \times 10^{-10}$ W; the thermal conductivities of the unmodulated 2D electron gas conductors, κ_1 and κ_2, are equivalent to conductances 60 and 200 Ω, respectively.

boundary. Strictly speaking, the aforementioned discrepancy may also be related to the method of thermopower measurement or the applicability of the Mott relation to the case under study. To exclude these possibilities, we performed additional independent measurements of the derivative of conductivity with respect to energy in order to compare them with the thermopower dependences. We measured the resistivity tensors ($\hat{\rho}_1$, $\hat{\rho}_2$) for two states of the sample with slightly different electron concentrations N_1 and N_2 ($N_2 = 1.1N_1$), which were obtained by illuminating the sample with an LED. Then, the thermopower was calculated by Eq. (1), where the derivative of $\hat{\rho}$ with respect to energy was expressed through the derivative with respect to electron density: $d\hat{\rho}(B)/dE \approx \nu[\hat{\rho}_2(B) - \hat{\rho}_1(B)]/[N_2 - N_1]$. The magnetic-field dependences of the diagonal $S^N_{xx}(B)$ and off-diagonal $S^N_{xy}(B)$ components of the thermopower tensor calculated in this way are shown in Fig. 2 (the dotted lines). One can see that they agree well with the measured thermopower for both components of the thermopower tensor. This result confirms the correctness of the experimental method used for thermopower measurements and the validity of the Mott relation in the case under study.

The dependences $S^N_{xx}(B)$ and $S^N_{xy}(B)$ obtained by us carry important information on the temperature distribution in the sample, which is necessary for converting the measured thermal stresses to thermopower units. The important parameters of this distribution are the temperature difference between probes *7* and *8* (see the inset in Fig. 1); ΔT_{78}, which determines the scale for S_x; and the average temperature gradient on the line connecting probes *4* and *7*, $\nabla_x T|_{47}$, which determines the scale for S_{xy}: $V_{47}(B) = S_{xy}(B)W\nabla_x T|_{47}$. The resulting values of these parameters, $\Delta T_{78} = 30$ mK and $\nabla_x T|_{47} = 20$ mK/μm, corresponding to the dependences $S_{xx}(B)$ and $S_{xy}(B)$ in Fig. 2, were chosen for the best agreement with the curves $S^N_{xx}(B)$ and $S^N_{xy}(B)$. At the same time, the temperature distribution in the sample, $T(x, y)$, can be obtained from the solution to the heat conduction equation $\Delta T(x, y) = (T(x, y) - T_L)/L_T^2$, where L_T is the temperature relaxation length describing the energy transfer to the phonon system. To determine this length, we experimentally measured the thermopower between probes *5* and *8*, which are farther from the heater than probes *4* and *7*. The measurements showed that $V_{58}(B) \approx 0.2V_{47}(B)$. This means that $\nabla_x T|_{58} \approx 0.2\nabla_x T|_{47}$. The latter relation was used as an additional condition for the numerical solution of the heat conduction equation. The results of these calculations are shown in Fig. 3 together with the boundary conditions used in the calculations. The value obtained for L_T is 11 μm, and the parameters of interest are $\nabla_x T|_{47} = 27$ mK/μm and $\Delta T_{78} = 26$ mK. These values are close to the aforementioned scaling coefficients that bring the curves $S_{xx}(B)$ and $S_{xy}(B)$ into best agreement with the curves $S^N_{xx}(B)$ and $S^N_{xy}(B)$ (Fig. 2). It should be noted that the length L_T can be independently obtained theoretically from the

equation $N_s dP/dT_e = \kappa/L_T^2$, where $P = \dot{Q}(T_e) - \dot{Q}(T_L)$ is the total power transferred from electrons to phonons. As was shown theoretically, for $T_e \lesssim 2$ K, $\dot{Q}$ is determined by the screened piezoelectric interaction, which yields $\dot{Q} \propto T^5$ [22]. The presence of anisotropy in the phonon dispersion law [23] leads to the formula $\dot{Q} \approx 270 T^5 N_S^{-3/2}$ (where T is measured in Kelvin, and N_S, in 10^{11} cm^{-2} units). A similar $\dot{Q}(T_e)$ dependence was experimentally obtained for the 2D electron gas in a GaAs/AlGaAs heterojunction, and it was shown that the T^5 behavior persists up to temperatures of 3 K and higher [24]. The corresponding calculations for our case estimate the temperature relaxation length as $L_T \approx 10$ μm, which agrees well with the experimental estimates of L_T.

The main problem that arises in interpreting the magnetotransport anomalies in systems with dynamical chaos consists in revealing the stable electron trajectories responsible for the observed features. This problem is usually solved by numerical simulation. A direct calculation of kinetic coefficients by averaging the contributions of all types of trajectories does not solve the problem. Therefore, a sequential interpretation requires a separate theoretical consideration, which, for the case of magnetoresistance, can be found in, e.g., [4]. We restrict our consideration to the contribution of stable runaway electron trajectories responsible for the magnetoresistance anomalies [3] to the thermopower features.

As is known, in a disordered conductor at low temperatures, the thermopower is small, because, in the presence of a temperature gradient, the quasielectrons (above the Fermi level) and the quasiholes (under the Fermi level) move in the same direction and the charges carried by them virtually cancel each other. In systems with dynamical chaos, in addition to the chaotic motion of charge carriers, stable trajectories with anomalous diffusion coefficients are present. In the hard wall model, electrons are considered as particles moving over arcs of cyclotron radius R_c in the intervals between elastic collisions with the antidot boundaries. Figure 4 shows the results of the numerical simulation based on this model with Eqs. (2), (1), and (4), which illustrate the fraction of stable runaway trajectories and their contribution to the thermoelectric coefficients. It should be noted that it is not quite correct to consider the contribution of trajectories to the thermopower, because, according to Eq. (1), the contribution of a group of trajectories to the thermopower tensor is nonadditive, unlike the case of the thermoelectric tensor $\hat{\epsilon} = \hat{\sigma}\hat{S}$. From Fig. 4, one can see that the fraction of these trajectories is maximum at a certain magnetic field (point B in Fig. 4a) corresponding to the resonant cyclotron radius R_c^*. In this case, both quasielectrons and quasiholes move over stable runaway trajectories and have anomalously high but close mobility values. As a result, their contribution $\delta\epsilon_{xx}$ to the diagonal component of the thermoelectric tensor is small (Fig. 4b), as in the case of a disordered conductor. However, somewhat off the resonance (point A in Fig. 4b), only quasiholes, whose energy and, hence, cyclotron radius are smaller, move along the runaway trajectories, whereas quasielectrons leave the resonance region and perform a chaotic motion. Thus, the mobility of quasiholes proves to be much higher than that of quasielectrons, and the total charge transferred by the carriers proves to be positive, which gives rise to a maximum of $\delta\epsilon_{xx}$ at point A in Fig. 4b. When the deviation from the resonance is in the direction of higher magnetic fields (point C), only quasielectrons remain in the resonance region, while quasiholes perform a chaotic motion, which leads to a negative value of $\delta\epsilon_{xx}$. As one can see from Fig. 4c, $\delta\epsilon_{xy}$ exhibits a more complex behavior as a function of magnetic field. For a closer investigation of the role of different types of trajectories in magnetotransport anomalies of thermopower, a separate theoretical investigation of thermopower in systems with dynamical chaos is necessary. Nevertheless, the above consideration allows us to conclude that the anomalies observed in the thermopower may be caused by the violation of the quasielectron–quasihole symmetry near the geometrical resonances.

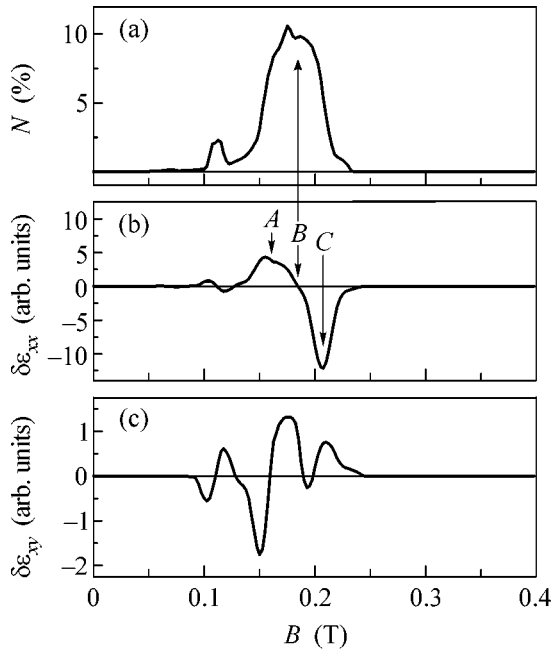

Fig. 4. Results of the numerical simulation of the magnetic-field dependences of (a) the fraction and (b, c) the contributions of the runaway and close-to-runaway trajectories to the (b) diagonal and (c) off-diagonal components of the thermopower tensor.

Thus, we experimentally studied the diffusion component of thermopower in a square lattice of antidots.

We found that both components of the thermopower tensor exhibit commensurability oscillations that are much more pronounced than the corresponding oscillations of magnetoresistance. The oscillations are strongest in the off-diagonal component of the thermopower tensor S_{xy}, where they are accompanied by a change in sign of the thermopower near the resonances. On the basis of the Kubo and Mott formulas in the framework of the hard wall model of antidots, we determined the relation between the thermopower tensor and the derivative of the resistivity tensor with respect to magnetic field. The resulting expression qualitatively describes the behavior of the diagonal component of the thermopower tensor S_{xx}, whereas, in the case of S_{xy}, it disagrees with the experiment. A possible origin of this disagreement is the energy dependence of the thickness of the depletion layer forming the antidot boundary. A comparative analysis of thermopower and magnetoresistance measurements allowed us to determine the parameters characterizing the temperature distribution in the sample and also to verify the correctness of the method of thermopower measurements and the validity of the Mott relation for the case under study.

This work was supported by the Russian Foundation for Basic Research, project nos. 04-02-16894 and 05-02-17200-a. The work of M.V.B. was supported by INTAS, grant no. YSF 03-55-639, and by the Foundation in Support of Russian Science.

REFERENCES

1. K. Ensslin and P. M. Petroff, Phys. Rev. B **41**, 12307 (1990).
2. D. Weiss, M. L. Roukes, A. Menschig, *et al.*, Phys. Rev. Lett. **66**, 2790 (1991).
3. É. M. Baskin, G. M. Gusev, Z. D. Kvon, *et al.*, Pis'ma Zh. Éksp. Teor. Fiz. **55**, 649 (1992) [JETP Lett. **55**, 678 (1992)].
4. É. M. Baskin, A. G. Pogosov, and M. V. Éntin, Zh. Éksp. Teor. Fiz. **110**, 2061 (1996) [JETP **83**, 1135 (1996)].
5. R. Fleischmann, T. Geisel, and R. Ketzmerick, Phys. Rev. Lett. **68**, 1367 (1992).
6. M. V. Budantsev, Z. D. Kvon, A. G. Pogosov, *et al.*, JETP Lett. **63**, 347 (1996).
7. G. M. Gusev, Z. D. Kvon, A. G. Pogosov, and M. M. Voronin, JETP Lett. **65**, 248 (1997).
8. G. M. Gusev, Z. D. Kvon, and A. G. Pogosov, Zh. Éksp. Teor. Fiz. **110**, 696 (1996) [JETP **83**, 375 (1996)].
9. G. M. Gusev, Z. D. Kvon, L. V. Litvin, *et al.*, Pis'ma Zh. Éksp. Teor. Fiz. **55**, 129 (1992) [JETP Lett. **55**, 123 (1992)].
10. R. Schuster, K. Ensslin, D. Wharam, *et al.*, Phys. Rev. B **49**, 8510 (1994).
11. L. Aleiner and I. Larkin, Phys. Rev. B **54**, 14423 (1996).
12. M. V. Budantsev, R. A. Lavrov, A. G. Pogosov, *et al.*, Pis'ma Zh. Éksp. Teor. Fiz. **79**, 201 (2004) [JETP Lett. **79**, 166 (2004)].
13. L. W. Molenkamp, H. van Houten, C. W. J. Beenakke, *et al.*, Phys. Rev. Lett. **65**, 1052 (1990).
14. S. F. Godijn, S. Moller, H. Buhmann, *et al.*, Phys. Rev. Lett. **82**, 2927 (1999).
15. A. S. Dzurak, C. G. Smith, C. H. W. Barnes, *et al.*, Phys. Rev. B **55**, R10197 (1997).
16. S. Moller, H. Buhmann, S. F. Godijn, and L. W. Molenkamp, Phys. Rev. Lett. **81**, 5197 (1998).
17. S. Maximov, M. Gbordzoe, H. Buhmann, *et al.*, Phys. Rev. B **70**, 121308(R) (2004).
18. A. G. Pogosov, M. V. Budantsev, D. Uzur, *et al.*, Phys. Rev. B **66**, 201303(R) (2002).
19. P. W. Anderson, E. Abrahams, and T. V. Ramakrishnan, Phys. Rev. Lett. **43**, 718 (1979).
20. R. Fleischmann, T. Geisel, and R. Ketzmerick, Europhys. Lett. **25**, 219 (1994).
21. R. Kubo, J. Phys. Soc. Jpn. **12**, 570 (1957).
22. P. J. Price, J. Appl. Phys. **53**, 6863 (1982).
23. C. Jasiukiewicz and V. Karpus, Semicond. Sci. Technol. **11**, 1777 (1996).
24. N. J. Appleyard, J. T. Nicholls, M. Y. Simmons, *et al.*, Phys. Rev. Lett. **81**, 3491 (1998).

Translated by E. Golyamina

JETP Letters, Vol. 81, No. 9, 2005, pp. 467–470. From Pis'ma v Zhurnal Éksperimental'noĭ i Teoreticheskoĭ Fiziki, Vol. 81, No. 9, 2005, pp. 583–586.

Weak Intermolecular Charge Transfer in the Ground State of a π-Conjugated Polymer Chain¶

D. Yu. Paraschuk[1], S. G. Elizarov[1], A. N. Khodarev[1], A. N. Shchegolikhin[2], S. A. Arnautov[3], and E. M. Nechvolodova[3]

[1] *International Laser Center, Moscow State University, Moscow, 119992 Russia*
e-mail: paras@polys.phys.msu.su
[2] *Emanuel Institute of Biochemical Physics, Russian Academy of Sciences, Moscow, 119991 Russia*
[3] *Semenov Institute of Chemical Physics, Russian Academy of Sciences, Moscow, 119991 Russia*
Received March 2, 2005; in final form, March 25, 2005

We show that a π-conjugated polymer chain can demonstrate weak intermolecular charge transfer in the electronic ground state. Poly[2-methoxy-5-(2'-ethyl-hexyloxy)-1,4-phenylene vinylene]/2,4,7-trinitrofluorenone (MEH-PPV/TNF) donor–acceptor films have been studied by optical absorption, Raman, infrared spectroscopy, and differential scanning calorimetry. The factors influencing weak intermolecular charge transfer in π-conjugated chains are discussed. © *2005 Pleiades Publishing, Inc.*

PACS numbers: 82.35.Cd, 78.30.Jw, 78.40.Me

1. Introduction. As is well known for small aromatic conjugated molecules, they can easily form intermolecular charge-transfer (CT) complexes in the electronic ground state with a molecule having a higher electron affinity (see, e.g., [1, 2]). Such CT complexes were widely studied in the 1950s–1960s, and their properties were successfully interpreted in the framework of the Mulliken model of weak CT interaction suggesting mixing of the ground-state wavefunctions [3]. These CT complexes usually have characteristic optical absorption in the visible range corresponding to a CT band. As was recently shown, relatively large π-conjugated molecules such as fullerenes or phthalocyanines can also form a ground-state CT complex [4, 5]. Nonconjugated polymers demonstrate CT interaction in the electronic ground state as well; e.g., polyvinylcarbazole CT complexes have been thoroughly studied since the 1970s [6, 7]. Intramolecular CT complexes of a conjugated polymer have been reported recently for polythiophene [8], where weak CT occurs from a polymer unit cell to the covalently bonded acceptor molecule.

At the same time, to our best knowledge, there is no reliable evidence in the literature reporting noticeable intermolecular CT interaction of a π-conjugated polymer chain in the electronic ground state, although a number of types of donor–acceptor blends and bilayers of π-conjugated polymers with low-molecular (e.g., [9, 10]) and high-molecular [11–14] acceptors, including fullerenes [15, 16] and nanotubes [17], have been studied. It was demonstrated that donor–acceptor blends of conjugated polymers and organic electronic acceptors, e.g., MEH-PPV/C_{60} [15], MEH-PPV/tetracyanoquinodimethane (TCNQ) [9], do not usually demonstrate ground-state CT. Despite early studies of poly(3-octylthiophene)/C_{60} films that showed nonadditive features in the optical absorption spectrum [18, 19], their vibrational IR spectra did not show any signs of nonadditivity [20]. Note that nonadditivity in the optical absorption spectrum of a donor–acceptor blend could result from other reasons, e.g., acceptor (donor) aggregation. At the same time, vibrational spectroscopy data could give strong evidence of CT complex formation, since CT interaction should result in frequency shifts of the donor (acceptor) vibrational bands, which are the most sensitive to redistribution in the π-electron density.

In our recent studies, MEH-PPV blended with low-molecular organic acceptors, TNF or 1,5-dinitroantraquinone (DNAQ), we have observed that both the optical and IR transmission spectra of the blends are nonadditive [21]. This could indicate CT interaction in the electronic ground state, if the origin of the nonadditivity were established. In fact, phase separation typical for donor–acceptor blends can increase light scattering, thus giving an observable effect of nonadditivity. In this letter, we show conclusive evidence for intermolecular CT interaction between a π-conjugated polymer chain and a low-molecular organic acceptor. We studied MEH-PPV/TNF blends (Fig. 1) and show that a CT absorption band appears in the optical absorption spectra and several vibrational donor (acceptor) bands demonstrate frequency shifts both in Raman and IR spectra. Further evidence follows from differential scanning calorimetry (DSC) data. We interpret these observa-

¶ This article was submitted by the authors in English.

0021-3640/05/8109-0467$26.00 © 2005 Pleiades Publishing, Inc.

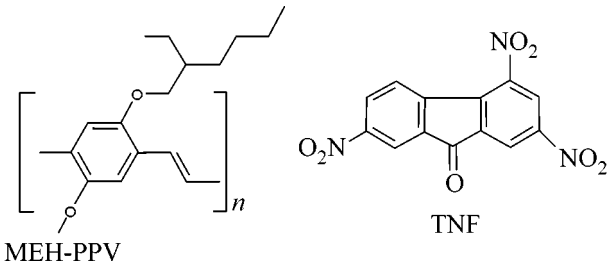

Fig. 1. Structural formula for MEH-PPV and TNF.

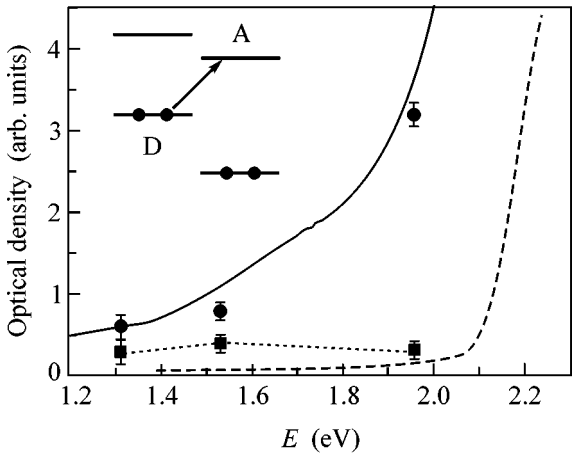

Fig. 2. Absorption spectra of 1 : 1 MEH-PPV/TNF (solid) and pristine MEH-PPV (dashed) drop-cast films prepared from chlorobenzene. Points show the sum of absorption and scattering (circles) and only the scattering (squares) contributing to the measured optical density of the 1 : 1 MEH-PPV/TNF film by using a technique described in [22]. The absorption and scattering data for the MEH-PPV/TNF molar ratio within the range 0.1–1 fall between those of pristine MEH-PPV and 1 : 1 MEH-PPV/TNF. The inset illustrates the donor and acceptor energy levels; the arrow indicates the CT complex absorption corresponding to the electron transfer from the highest occupied orbital (HUMO) of the donor (D) to the lowest unoccupied orbital (LUMO) of the acceptor (A).

tions as a result of partial ground-state CT in the donor–acceptor pair, i.e., CT interaction.

2. Experimental. Drop-cast films of pristine MEH-PPV (Sigma-Aldrich, MW = 125.000) and its blends with TNF (Fig. 1) were prepared from different solvents (chlorobenzene, toluene, cyclohexanone) with MEH-PPV concentration in the range of 0.5–2 g/l and by varying the molar ratio of the acceptor per polymer unit chain in the range of 0.1–1. Films on glass substrates and free-standing films were studied. All the measurements were done in ambient conditions.

The optical absorption spectra were recorded using a spectrophotometer (Hitachi 300). MEH-PPV/acceptor blends in a ratio of 1 : 1 had higher optical scattering than pristine MEH-PPV films. To evaluate the contribution of scattering losses in the optical transmission spectra, we measured the film transmission in narrow and wide (0.25 sr) solid angles at several laser wavelengths (633, 810, 946 nm) [22]. The IR transmission spectra of free-standing films of the blends and Raman spectra of the same films lightly packed in a "cavity" sample holder were recorded with 2-cm^{-1} resolution using a Perkin–Elmer FTIR (Model 1720-X) spectrophotometer furnished with a NIR-FT Raman attachment. The backscattering geometry and a liquid nitrogen–cooled InGaAs detector were used for acquiring Raman spectra at an excitation wavelength of 1064 nm. DSC data were taken at a 10-K/min heating rate using a Perkin-Elmer Series 7 DSC analyzer calibrated by indium and zinc melting standards.

3. Experimental results. MEH-PPV/TNF films have a substantial difference in color from that of pristine polymer. The absorption spectra of the MEH-PPV/TNF films are shifted to the red and have extended absorption tails, as compared to pristine MEH-PPV, that extend down beyond 1.5 eV (Fig. 2). Although addition of the acceptor results in a noticeable increase in the scattering losses (Fig. 2), they give the major contribution to the measured optical density only for energies below 1.5 eV. Since TNF absorbs light mainly in the ultraviolet spectral range, the observed optical absorption below the absorption edge of pristine MEH-PPV (Fig. 2) could be a consequence of noticeable ground-state interaction of MEH-PPV chains with the TNF molecules resulting from CT complex formation (Fig. 2, inset). Increasing the optical scattering in MEH-PPV/TNF blends compared to pristine MEH-PPV films could result from the portion of the TNF molecules that are not involved in CT interaction. In fact, TNF crystallites are seen in 1 : 1 MEH-PPV/TNF blends using an optical microscope. Note that the appearance of a redshift and of an extended tail in the MEH-PPV spectrum could be induced by two other effects: aggregation of polymer chains [23] and/or presence of relatively long conjugated chains. However, since the absorption tails observed for the blends were too intense and redshifted, it is difficult to suppose that either could result from blending of noninteracting components.

Partial CT in the electronic ground state is expected to induce shifts in the vibrational frequencies of both the donor and acceptor [1]. Indeed, as Fig. 3 shows, Raman bands of MEH-PPV at ~1550 and ~1580 cm^{-1}, corresponding to carbon–carbon (CC) stretching of the phenyl ring, are redshifted by 3–4 cm^{-1} in the 1 : 1 MEH-PPV/TNF blend. The observed redshifts support our assumption about partial CT from MEH-PPV to TNF in the electronic ground state. As compared with our case, doping of conjugated polymers, as has been reported for *p*-doped PPV [24, 25], corresponds to full CT and is capable of lowering the Raman frequencies of phenyl ring CC stretching modes, which are strongly

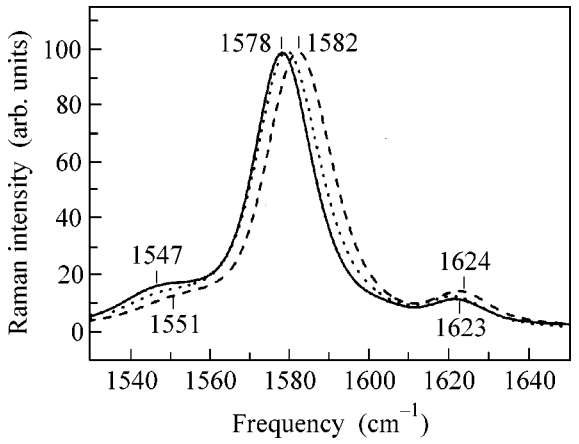

Fig. 3. Raman spectra of pristine MEH-PPV (dashed), 1 : 0.2 MEH-PPV/TNF (dotted), 1 : 1 MEH-PPV/TNF (solid) free-standing films in the region of the strongest Raman band of MEH-PPV.

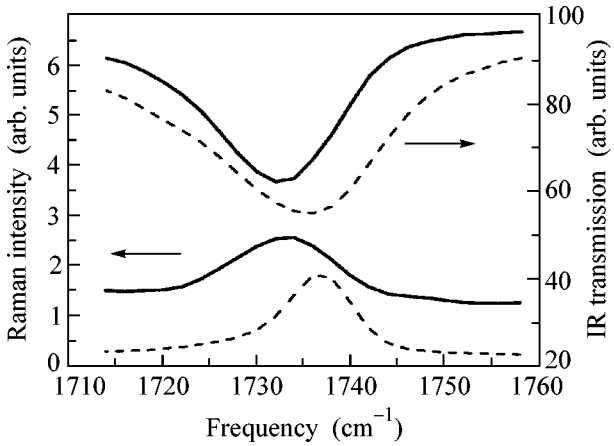

Fig. 4. Raman and IR spectra of pristine TNF (dashed) and 1 : 1 MEH-PPV/TNF (solid) free-standing films in the region of the TNF C=O stretch vibration. The spectra are offset vertically for clarity.

coupled with delocalized π electrons by up to a few tens of wavenumbers.

Furthermore, we have found that a number of other Raman and IR bands in the MEH-PPV/TNF blends are not just a superposition of the corresponding spectra of pristine MEH-PPV and TNF. Here, we discuss frequency shifts relevant only to the TNF carbonyl C=O vibration in the vicinity of ~1730 cm^{-1} observed both in IR and Raman spectra (Fig. 4). The noticeable redshift of the C=O band in TNF for a few wavenumbers is explained by an increase in the electron density in the conjugated system of TNF resulting from partial ground-state CT. As is well documented for substituted fluorenones [26], introduction of electronegative substituents into a fluorenone molecule tends to increase the C=O frequency, and the increase can amount to up to ~25 cm^{-1} within the series from aminofluorenone to TNF. The observed redshifts of the C=O frequency in MEH-PPV/TNF imply that the electronegative action of nitro substituents could be partly compensated for by extra electron density donated by MEH-PPV.

Thus, our vibrational studies indicate noticeable mixing of the ground-state electronic wavefunctions of MEH-PPV and TNF providing partial CT from the donor to the acceptor. The observed shifts of vibrational bands in the MEH-PPV/acceptor blends (by a few wavenumbers) indicate the relatively weak CT interaction typical of Mulliken CT complexes.

If a CT complex is formed, it can give an observable effect in the DSC traces [27]. We have found that a strong endotherm peak corresponding to the melting point of the crystalline TNF phase decreased substantially in 1 : 1 MEH-PPV/TNF films and fully disappeared in 1 : 0.2 MEH-PPV/TNF films (Fig. 5). Thus, there is no evidence of the presence of the crystalline acceptor phase in the 1 : 0.2 MEH-PPV/TNF film, and, therefore, almost all the acceptor molecules are involved in some type of interaction with MEH-PPV. We interpret these observations as a direct consequence of intermolecular CT interaction between MEH-PPV and TNF.

4. Discussion. As mentioned above, despite the number of donor–acceptor blends of conjugated polymers that have been studied by now, weak CT from a π-conjugated polymer chain in its electronic ground state has not been observed. At the same time, from the very beginning of the study of the field of π-conjugated polymers, they have been well known to be easily doped by elements and inorganic compounds [28]. Apparently, this doping corresponds to full CT. It is unclear why weak ground-state CT is not easy to

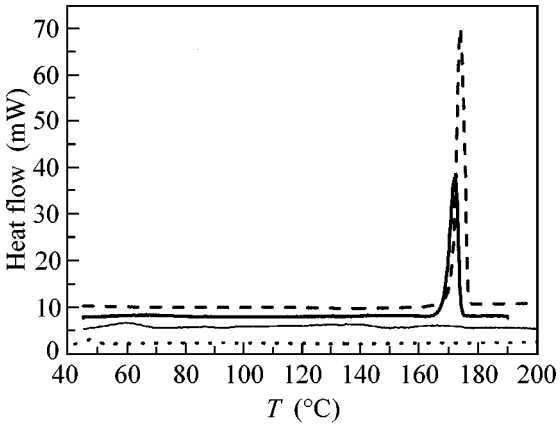

Fig. 5. DSC traces for neat TNF (dashed line), 1 : 1 MEH-PPV/TNF film (bold solid line), 1 : 0.2 MEH-PPV/TNF film (thin solid line), and pristine MEH-PPV polymer (dotted line). All curves are normalized to equal sample weight and are offset vertically for clarity.

observe in π-conjugated polymers. We discuss here the main factors influencing weak CT from a π-conjugated chain. The important parameter controlling donor–acceptor intermolecular CT is the difference between the donor ionization potential and the acceptor electron affinity (EA) [1]. The EA of TNF is about 2.2 eV [29], which is within the range of EAs of acceptors studied in blends with MEH-PPV in [9]. Therefore, the magnitude of EA alone does not determine the ground-state CT in π-conjugated chains. On the other hand, according to Mulliken's model [1], intermolecular CT in the electronic ground state depends on the overlapping of the HOMO donor and the LUMO acceptor wavefunctions. Since the wavefunction at an extended conjugated chain (donor) is strongly delocalized, noticeable overlapping of the donor and acceptor wavefunctions necessitates delocalization of the acceptor wavefunction as well. This could explain why such a strong acceptor as TCNQ does not lead to ground-state CT in MEH-PPV/TCNQ blends [9]. However, ground-state CT was not observed for the acceptors longer and shorter than TNF either [9]. One can suggest that the TNF molecular orbital pattern provides for better overlapping with the corresponding MEH-PPV molecular orbitals. Note that another acceptor, namely, DNAQ, which has an EA and length similar to those of TNF, seems to provide weak ground-state CT in MEH-PPV/DNAQ blends as well. In these films, the CT band was less intense and the frequency shifts in the vibrational spectra were weaker [21] than in MEH-PPV/TNF films.

5. Conclusions. Thus, we have given conclusive evidence that a π-conjugated polymer can participate in intermolecular ground-state CT interactions. MEH-PPV/TNF films show optical absorption spectra extending down to the near-IR spectral range, while the vibrational spectra of the blends exhibit shifts of some characteristic vibrational bands belonging to both the donor and the acceptor. In addition, DSC studies of MEH-PPV/TNF films indicate that the content of the crystalline TNF phase in the blend is substantially decreased. These observations have been interpreted as results of CT interaction between MEH-PPV and TNF in their electronic ground state. Our data are consistent with the Mulliken model of intermolecular CT complexes, which suggests noticeable mixing of the donor and acceptor wavefunctions.

This research was supported by European Office of Aerospace Research and Development via the International Science and Technology Center (grant no. 2666P) and by the Russian Foundation for Basic Research (project no. 04-02-16658).

REFERENCES

1. S. P. McGlynn, Chem. Rev. **58**, 1113 (1958).
2. R. E. Merrifield and W. D. Phillips, J. Am. Chem. Soc. **80**, 2778 (1958).
3. R. S. Mulliken, J. Am. Chem. Soc. **74**, 811 (1952).
4. M. Ichida, T. Sohda, and A. Nakamura, Chem. Phys. Lett. **310**, 373 (1999).
5. G. Ruani, C. Fontanini, M. Murgia, and C. Taliani, J. Chem. Phys. **116**, 1713 (2002).
6. G. Weiser, J. Appl. Phys. **43**, 5028 (1972).
7. O. Rocquin and C. Chevrot, Synth. Met. **89**, 119 (1997).
8. P. J. Skabara, I. M. Serebryakov, I. F. Perepichka, *et al.*, Macromolecules **34**, 2232 (2001).
9. A. J. Heeger, F. Wudl, N. S. Sariciftci, *et al.*, J. Phys. I **6**, 2151 (1996).
10. J. J. Dittmer, K. Petritsch, E. A. Marseglia, *et al.*, Synth. Met. **102**, 879 (1999).
11. J. J. M. Halls, C. A. Walsh, N. C. Greenham, *et al.*, Nature **376**, 498 (1995).
12. M. M. Alam and S. A. Jenekhe, J. Phys. Chem. B **105**, 2479 (2001).
13. A. J. Breeze, Z. Schlesinger, S. A. Carter, *et al.*, Sol. Energy Mater. **83**, 263 (2004).
14. R. Pacios and D. D. C. Bradley, Synth. Met. **127**, 261 (2002).
15. C. H. Lee, G. Yu, D. Moses, *et al.*, Phys. Rev. B **48**, 15425 (1993).
16. G. Yu, J. Gao, J. C. Hummelen, *et al.*, Science **270**, 1789 (1995).
17. H. Ago, M. S. P. Shaffer, D. S. Ginger, *et al.*, Phys. Rev. B **61**, 2286 (2000).
18. S. Morita, A. A. Zakhidov, and K. Yoshino, Solid State Commun. **82**, 249 (1992).
19. L. Smilowitz, N. S. Sariciftci, R. Wu, *et al.*, Phys. Rev. B **47**, 13835 (1993).
20. K. H. Lee, R. A. J. Janssen, N. S. Sariciftci, and A. J. Heeger, Phys. Rev. B **49**, 5781 (1994).
21. A. A. Bakulin, A. N. Khodarev, D. S. Martyanov, *et al.*, Dokl. Chem. **398**, 204 (2004).
22. S. G. Elizarov, A. E. Ozimova, D. Yu. Paraschuk, *et al.* (unpublished).
23. T. Q. Nguyen, I. B. Martini, J. Liu, and B. J. Schwartz, J. Phys. Chem. B **104**, 237 (2000).
24. A. Sakamoto, Y. Furukawa, and M. Tasumi, J. Phys. Chem. **98**, 4635 (1994).
25. M. Baitoul, J. Wery, S. Lefrant, *et al.*, Phys. Rev. B **68**, 195203 (2003).
26. C. J. Pouchert, *The Aldrich Library of FTIR Spectra* (Aldrich Chemical, Milwaukee, WI, 1985).
27. H. Yang and A. Natansohn, Chem. Mater. **6**, 1842 (1994).
28. A. J. Heeger, S. Kivelson, J. R. Schrieffer, and W. P. Su, Rev. Mod. Phys. **60**, 781 (1988).
29. E. C. M. Chen and W. E. Wentworth, J. Chem. Phys. **63**, 3183 (1975).

JETP Letters, Vol. 81, No. 9, 2005, pp. 471–474. Translated from Pis'ma v Zhurnal Éksperimental'noĭ i Teoreticheskoĭ Fiziki, Vol. 81, No. 9, 2005, pp. 587–590.

Nonmonotonic Variation of the Electrical Conductivity of C_{60} Fullerene Crystals Dynamically Compressed to 300 kbar As Evidence of Anomalously Strong Reduction of the Energy Barrier of C_{60} Polymerization at High Pressures

Yu. A. Ossipyan[1], B. V. Avdonin[2], K. L. Kagan[2], R. K. Nikolaev[1], V. I. Postnov[2], N. S. Sidorov[1], D. V. Shakhraĭ[2], A. F. Shestakov[2], V. V. Kveder[1], and V. E. Fortov[2]

[1] *Institute of Solid State Physics, Russian Academy of Sciences, Chernogolovka, Moscow region, 142432 Russia*

[2] *Institute of Problems of Chemical Physics, Russian Academy of Sciences, Chernogolovka, Moscow region, 142432 Russia*

Received February 15, 2005; in final form, March 30, 2005

The electrical conductivity of a C_{60} fullerene crystal is measured under the conditions of quasi-isentropic loading by a diffuse shock wave to a pressure of 30 GPa at room temperature. Nonmonotonic behavior of the conductivity of the samples with an increase in pressure is observed: first, conductivity increases by several orders of magnitude and, then, decreases rapidly. An increase in conductivity is explained by a decrease in the band gap under pressure, whereas a decrease in conductivity may be explained under the assumption that the energy barrier of C_{60} polymerization decreases similarly to the band gap with an increase in pressure. As a result, the rate of C_{60} polymerization at high pressures increases considerably (by more than seven orders of magnitude).

PACS numbers: 71.30.+h, 81.40.Vw

The study of the electrical properties of materials at high pressures reveals rather nontrivial dependences of conductivity on pressure [1], which reflect the complex character of the change in the material state under compression. The study of the electrical conducting properties of fullerene crystals is of obvious interest, because, owing to the large size of fullerene molecules, the manifestation of metallization can be expected at lower pressures than in the case of hydrogen and other small molecules [2].

Moreover, the exhaustive study of fullerenes, which are used in numerous applications from medicine to superconductors, is of obvious fundamental importance for a deeper understanding of their properties. In particular, experiments on shock compression, where the distance between fullerene molecules in the lattice is changed very rapidly, can ensure the determination of the dynamics of chemical bonding between neighboring molecules.

In our previous work [3], we measured the conductivity σ of C_{60} fullerene crystals under the conditions of quasi-isentropic loading by a spread shock wave to a pressure of 15 GPa at two initial temperatures: $T = 293$ and 77 K. As a result, we observed a dramatic increase (by more than six orders of magnitude) in σ in the pressure range 0–15 GPa. When pressure was removed, the initial σ value was restored. The results of that work indicated a dramatic pressure-induced decrease in the band gap of C_{60} crystals. However, the character of the temperature dependence of conductivity under loading observed in our experiments favored the assumption that the band gap did not vanish and that the sample at a pressure of 15 GPa still was a semiconductor. X-ray phase analysis showed that the C_{60} sample under these conditions preserved its initial phase state when the pressure was removed. Similar but weaker effects in the conductivity behavior were also observed in experiments on hydrostatic compression of C_{70} [4].

This study is aimed at measuring the conductivity of C_{60} fullerene crystals at higher pressures in order to answer the question of the possibility of metallization of C_{60}. In our experiments, we used the mode of multistage quasi-isentropic compression of fullerene crystals by a series of successive shock waves to provide for the attainment of extremely high pressures without the considerable overheating of the sample characteristic of compression by a single shock wave. For example, the change in the fullerene temperature behind the front of a single shock wave with an amplitude of 30 GPa is evaluated using the well-known compressibility of C_{60} crystals [5, 6] as 900 K, whereas the heating of the sample in the quasi-isentropic mode used in the present experiments *a priori* does not exceed 100–150 K.

Experimental procedure. The schematic of the experiments is shown in Fig. 1. The sample *1*, a C_{60} crystal in the form of a rectangular $8 \times 2 \times 1$-mm plate, and a piezoresistive manganin pressure gauge *2* were located between two 1-mm Teflon layers *3* and *4*.

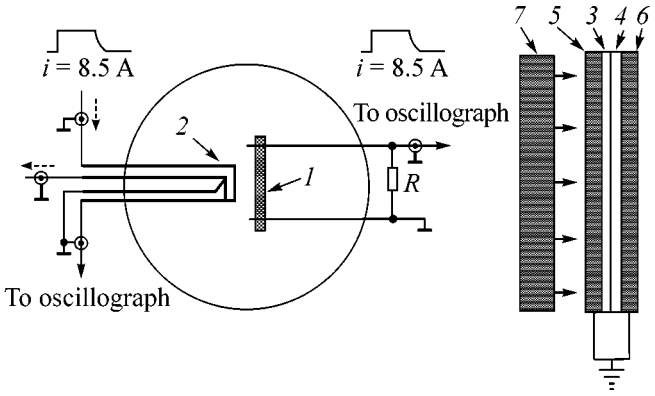

Fig. 1. Schematic of the experiment: (*1*) C_{60} crystal, (*2*) pressure gauge, (*3*, *4*) Teflon layers, (*5*) basis, (*6*) reflector, and (*7*) plate.

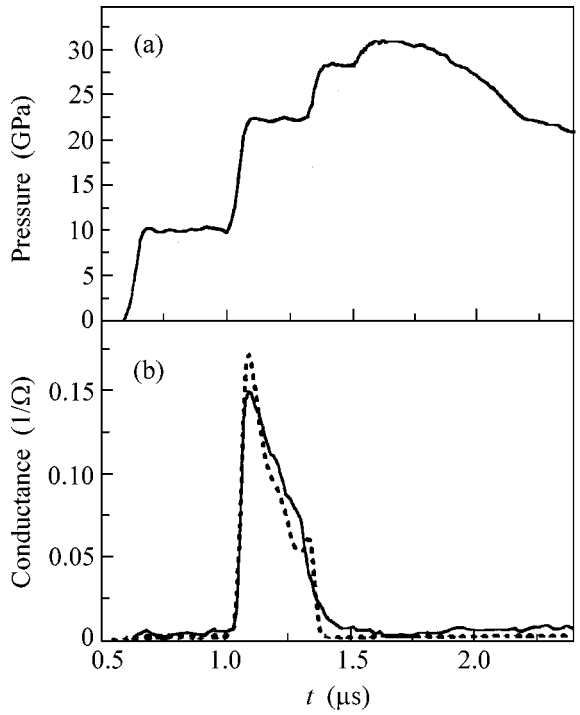

Fig. 2. Time dependence of (a) pressure *P* and (b) conductivity of the C_{60} crystal at the initial temperature $T = 300$ K. The dashed line is the theoretical curve calculated with $\beta' = 2.1$ meV/GPa and $\beta = 2.24$ meV/GPa.

Dynamic loading of the sample was produced by a series of shock waves circulating between basis *5* and reflector *6*. The shock waves were generated by an impact of steel plate *7* accelerated to a velocity of 2.0–2.5 km/s by a special explosive device.

The conductivity of the sample and the manganin pressure gauge during impact was measured by recording electrical signals on a TDS-7444A Tektonix digital oscilloscope that were then processed on a computer. The result of a typical measurement of the conductivity of C_{60} during stepwise quasi-isentropic compression to a final pressure of about 30 GPa is shown in Fig. 2 as time dependences of sample conductivity σ and pressure *P* measured by the manganin pressure gauge. It is seen that the conductivity of the sample first increases dramatically and, then, decreases gradually. It is important that an increase in conductivity can be attributed to an increase in pressure, whereas a decrease in conductivity is also observed in the region of nearly constant pressure. It should be noted that the characteristic space and time scales under the conditions of dynamic loading are such that diffusion and chemical interaction between the samples and the medium are absent, which excludes an interpretation of the results by these effects.

Discussion of the results. Fullerene C_{60} in the crystalline state is a semiconductor with a band gap E_g of about 2 eV. The edge of the optical exciton absorption corresponds to an energy of about 1.7 eV [7–9].

The C_{60} molecules in a crystal are bonded mainly by van der Waals interactions, and, therefore, the compressibility of C_{60} crystals under hydrostatic loading is very high (the Young modulus equals 13.5 GPa [5, 6]). Thus, a noticeable reduction of the distances between the neighboring C_{60} molecules in a crystal takes place even at moderate pressures. This reduction results in a sharp increase in overlapping of electron shells and, thus, to a sharp decrease in the band gap due to the broadening of both filled (valence) and unfilled energy bands. In the limiting case, the transition of the crystal into the metallic state can be expected.

Analysis of numerous data on the change in the optical absorption spectra of C_{60} crystals at hydrostatic pressure [9–13] shows that the band gap decreases with an increase in pressure with a coefficient $\beta = dE_G/dP$ of about 70–100 meV/GPa. Under the assumption that the Fermi level in the pure crystals used in experiments is approximately in the middle of the band gap, the pressure dependence of conductivity σ at a constant temperature *T* is estimated as

$$\sigma/\sigma_0 = \exp(-\beta P/2kT), \qquad (1)$$

where σ_0 is conductivity at zero pressure. Figure 3 shows the pressure dependence $\log_{10}(\sigma/\sigma_0)$ obtained in several experiments. It is seen that at the experimental data for pressures $P < 11$ GPa are well described by Eq. (1) with a β value of about 84 meV/GPa. For higher pressures, the β value calculated formally as $\beta = -2kTd(\log(\sigma/\sigma_0))/dP$ from the slope of the dependence shown in Fig. 3 decreases considerably, which, to some extent, can be a consequence of a decrease in the compressibility (increase in the Young modulus) of the crystal because of a pronounced nonparabolicity of the interaction potential between C_{60} molecules.

However, the most important result of this study is that, with an increase in the pressure above 20 GPa, the conductivity does not further increase but rather begins

to decrease (Figs. 2 and 3). Unlike an increase in conductivity that is obviously explained by an increase in pressure, the decrease in conductivity is also observed at a constant pressure, which indicates the occurrence of a certain kinetic process developing in time (Fig. 2).

Let us discuss the results. For interpretation of the effect observed in this work, it is important that, according to [14–17], at pressures exceeding P_0 = 0.5–1.0 GPa, the C_{60} polymer phase becomes dynamically advantageous. This phase is characterized by the formation of covalent bonds between C_{60} molecules. Thus, with an increase in pressure, a decrease in the band gap is accompanied by the appearance of the thermodynamic conditions for the phase transition to the polymer state.

At the same time, it is well known that the polymerization of C_{60} is a very slow thermally activated process with a rather high energy barrier. An elementary act in polymerization is the formation of bonds between neighboring C_{60} molecules in the lattice (dimerization) whose activation energy at a pressure P = 1 GPa is ~1.4 eV [18]. At pressures up to 1.5–2.0 GPa, polymerization is observed only at temperatures exceeding 500–600 K and after a sufficiently long (dozens of minutes) keeping of samples at high pressures. For this reason, we attempted to observe the insulator–metal transition in C_{60} crystals by using pulsed pressures, expecting that polymerization did not occur under these conditions.

Nevertheless, we believe that the only way to interpret a decrease in sample conductivity at pressures $P >$ 20 GPa is to assume a dramatic acceleration of the polymerization process at pressures exceeding 15–20 GPa. This assumption is based on the fact that the activation energy of the dimerization of C_{60} molecules is close to the energy of triplet exciton excitation. One can assume that this closeness is not accidental and that dimerization occurs if one of the molecules is excited to the triplet state. Indeed, in terms of chemistry, a fullerene molecule in an excited triplet state is a biradical and, like other radicals, may be readily attached to neighboring molecules along double bonds. This picture correlates with the well-known fact that the dimerization and polymerization of optically excited C_{60} molecules occur at room temperature and zero pressure [19–21]. In the primary reaction, an excited triple C_{60} molecule is apparently attached to a neighboring unexcited molecule, and they form a dimer in the triplet state with only one C–C bond between the molecules. According to the calculations by the density functional method with the PBE density functional [22] in the SBK basis [23] by the Priroda program [24], this process results in an energy gain of about 0.23 eV. Taking into account a decrease in the volume during such dimerization, one can assume that this decrease may be more considerable.

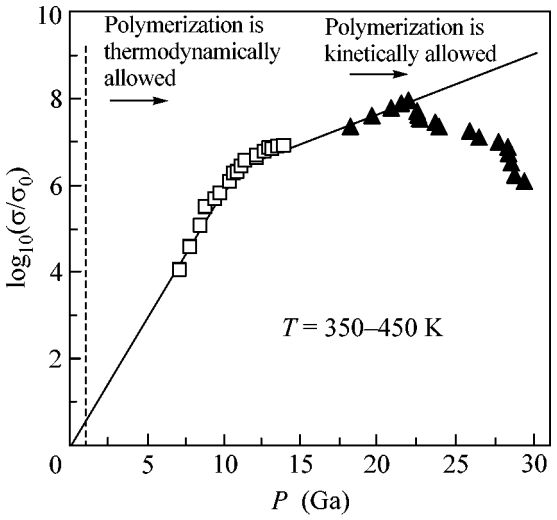

Fig. 3. Pressure dependence of conductivity σ for C_{60} crystals under pulse loading. The squares indicate data taken from [1], and triangles are data obtained in this study (see Fig. 2).

As the band gap decreases with an increase in pressure, the thermodynamically equilibrium concentration of excited triplet states also increases. At high pressures, the concentration of triplet excitations may increase so that their direct interaction becomes possible. If the spins are oriented oppositely, this interaction leads (without any activation) to the simultaneous formation of two C–C bonds between fullerene molecules (annihilation of triplet excitons). Thus, the polymerization process at high pressures may be considerably accelerated and, thus, result in the conductivity drop observed in the experiments. Using the effective rate constant of the first order r, we may describe this process in the first approximation as

$$r/r_0 = \exp(-\beta' P/kT), \quad (2)$$

where r_0 is the rate constant at P = 0 and β' is the coefficient on the order of β. Thus, under compression, the fraction of unpolymerized C_{60} would exponentially decrease with time t as exp(–rt). Assuming for simplicity that the conductivity of the C_{60} polymer phase is low (e.g., on the order of σ_0), one may write the time dependence of conductivity at pressure P as

$$\sigma/\sigma_0 = 1 + \exp(-\int r dt)(\exp(-\beta P/2kT) - 1). \quad (3)$$

Although this relationship is rather crude (e.g., effects associated with the features of the percolation of the two phases are disregarded), it qualitatively agrees with the experimental observations. The dashed line in Fig. 2b is calculated by Eq. (3) under the assumption that $\beta' \approx \beta \approx 21$ meV/GPa at pressures $P >$ 15 GPa.

Thus, the experimental data can be interpreted under the assumption that the energy barrier of the polymer-

ization of C_{60} decreases with an increase in pressure to the same extent as the band gap.

This study was supported by the Presidium of the Russian Academy of Sciences (programs "Low-Dimensional Quantum Structures" and "Thermal Physics and Mechanics of Extreme Energy Actions"), State Research Program "Controlled Synthesis of Fullerenes and Other Atomic Clusters," Council of the President of the Russian Federation for Support of Young Russian Scientists and Leading Scientific Schools (project no. NSh-1938.2003.2), and the Russian Foundation for Basic Research (project no. 03-02-16322).

REFERENCES

1. V. V. Yakushev, V. I. Postnov, V. E. Fortov, and T. I. Yaksheva, JETP **90**, 617 (2000).
2. V. E. Fortov, V. Ya. Ternovoi, M. V. Zhernokletov, *et al.*, JETP **97**, 259 (2003).
3. Yu. A. Ossipyan, V. E. Fortov, K. L. Kagan, *et al.*, Pis'ma Zh. Éksp. Teor. Fiz. **75**, 680 (2002) [JETP Lett. **75**, 563 (2002)].
4. Y. K. Vohra and S. T. Weir, in *Proceedings of International School of Physics "Enrico Fermi" on High Pressure Phenomena, Varenna, Italy, 2001*, Ed. by L. Ulivi *et al.* (IOS Press, Amsterdam, 2002), p. 96.
5. Yu. I. Prilutskii and G. G. Shapovalov, Phys. Status Solidi **201**, 361 (1997).
6. N. P. Kobelev, R. K. Nikolaev, Ya. M. Soifer, and S. S. Khasanov, Chem. Phys. Lett. **276**, 263 (1997).
7. A. N. Izotov, V. V. Kveder, Yu. A. Ossipyan, *et al.*, Zh. Éksp. Teor. Fiz. **114**, 2211 (1998) [JETP **87**, 1205 (1998)].
8. U. D. Venkateswaran, M. G. Schall, Y. Wang, *et al.*, Solid State Commun. **96**, 951 (1995).
9. G. Z. Li, J. Mater. Sci. **38**, 921 (2003).
10. F. Moshary, N. H. Chen, I. F. Silvera, *et al.*, Phys. Rev. Lett. **69**, 466 (1992).
11. K. P. Meletov, V. K. Dolganov, O. V. Zharikov, *et al.*, J. Phys. (Paris) **2**, 2097 (1992).
12. A. K. Sood, Solid State Commun. **81**, 89 (1992).
13. Yong-Nian Xu, Ming-Zhu Huang, and W. Y. Ching, Phys. Rev. B **46**, 4241 (1992).
14. I. O. Bashkin, V. I. Rashcupkin, A. F. Gurov, *et al.*, J. Phys.: Condens. Matter **6**, 7491 (1994).
15. Y. Iwasa, T. Arima, R. M. Fleming, *et al.*, Science **264**, 1570 (1994).
16. L. Marques, Nunes-M. Regueiro, and M. Perroux, Phys. Rev. B **54**, R12 633 (1996).
17. A. M. Rao, P. C. Eklund, U. D. Venkateswaran, *et al.*, Appl. Phys. A **64**, 231 (1997).
18. V. A. Davydov, L. S. Kashevarova, A. V. Rakhmanina, *et al.*, Chem. Phys. Lett. **333**, 224 (2001).
19. A. M. Rao, Zhou Ping, Wang Kai-An, *et al.*, Science **259**, 955 (1993).
20. C. Sekar, A. Thamizhavel, and C. Subramanian, Physica C (Amsterdam) **275**, 193 (1997).
21. I. Manika, J. Maniks, and J. Kalnacs, Fullerene Sci. Technol. **5**, 149 (1997).
22. J. P. Perdew, K. Burke, and M. Ernzerhof, Phys. Rev. Lett. **77**, 3865 (1996).
23. H. Basch and P. G. Jasien, Can. J. Chem. **70**, 612 (1992).
24. D. N. Laikov, Chem. Phys. Lett. **281**, 151 (1997).

Translated by L. Man

JETP Letters, Vol. 81, No. 9, 2005, pp. 475–478. Translated from Pis'ma v Zhurnal Éksperimental'noĭ i Teoreticheskoĭ Fiziki, Vol. 81, No. 9, 2005, pp. 591–594.

Ferromagnetic Ordering of Iron Impurities in the Kondo Semiconductor SmB_6

T. S. Altshuler[1], M. S. Bresler[2], and Yu. V. Goryunov[1]

[1] *Zavoĭskiĭ Physicotechnical Institute, Russian Academy of Sciences, Kazan, 420029 Tatarstan, Russia*
e-mail: tatiana@kfti.knc.ru

[2] *Ioffe Physicotechnical Institute, Russian Academy of Sciences, St. Petersburg, 194021 Russia*
e-mail: mikhail.bresler@pop.ioffe.rssi.ru

Received March 29, 2005

The Kondo semiconductor SmB_6 doped with 1 at. % Fe has been studied by the EPR method. The ferromagnetic ordering of iron ions observed at a relatively high temperature of 100 K is explained by their indirect exchange via the polarization of the SmB_6 matrix, which is enhanced owing to fluctuating-valence ions. © *2005 Pleiades Publishing, Inc.*

PACS numbers: 71.27.+a, 75.20.Hr, 76.30.–v

Samarium hexaboride (SmB_6) is a classical Kondo insulator (i.e., a narrow-gap semiconductor) [1]. This material has been studied by various methods during the last two decades, but many aspects in the physics of fluctuating valence remain unclear. This study is devoted to the EPR analysis of a SmB_6 single crystal doped with iron ions (1 at. %). The single crystal was grown using the solution–melt technique in the form of a $1.5 \times 1.5 \times 0.3$-mm wafer. Measurements were made at a frequency of 10^{10} Hz in the range $T = 1.6$–300 K.

In the entire temperature range, the EPR spectrum contains several lines. This spectrum belongs to iron ions, since pure (undoped) SmB_6 shows no signals in this field range. For angles $\varphi = \theta = 0$ (where φ and θ are the angles of rotation of the magnetic field about the tetrad axis of the single crystal in the plane of the sample and in a plane perpendicular to the plane of the sample, respectively), the g factors of the EPR lines at $T =$ 300 K are $g_1 = 2.22 + 0.04$, $g_2 = 3.00$, and $g_3 \sim 1.76$. The most intense line is the central one with g_1, which apparently corresponds to the unionized iron atom Fe^0. The electron structure of Fe^0 is analogous to that of $Ni^{2+}(3d^8\ {}^3F)$ and, in the cubic field of MgO, gives a single isotropic line with a g factor close to that observed in $Sm_{0.99}Fe_{0.01}B_6$ ($g_{Ni} = 2.227$) [2]. (The crystal structure of SmB_6 is a simple cubic lattice analogous to that of CsCl.)

Unionized iron atoms are quite rarely observed by the EPR method. These atoms were observed for the first time in silicon in 1955 and later by other authors (see, e.g., [3]). Two other lines are equidistant from the central line and depend on the angle of rotation of the sample in the magnetic field (these lines are interchanged for $\varphi = 90°$). Apparently, some of the unionized iron atoms are in local axisymmetric fields formed from the initial cubic field.

The most interesting result of this study is the temperature dependence of the positions and widths of EPR lines. As the temperature decreases to 100 K, the positions of the lines remain unchanged, but, below this temperature, a sharp shift of the lines is observed towards lower and higher fields at $\theta = 0$ (see Fig. 1) and 90°, respectively. Such behavior is an indication of the ferromagnetic ordering of the iron impurity. Below the Curie temperature (about 100 K), spontaneous magnetization M_0 appears and displaces the resonance field. The temperature dependence of spontaneous magneti-

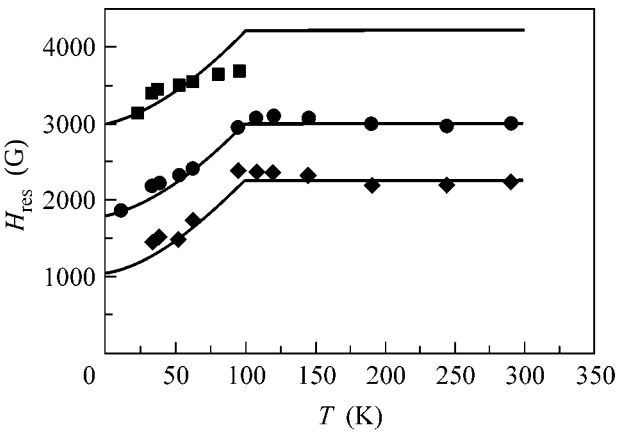

Fig. 1. Temperature dependence of the positions of EPR (central and side) lines of unionized Fe^0 atoms for angles $\varphi = \theta = 0$. The solid curves are the theoretical computations by formula (3).

0021-3640/05/8109-0475$26.00

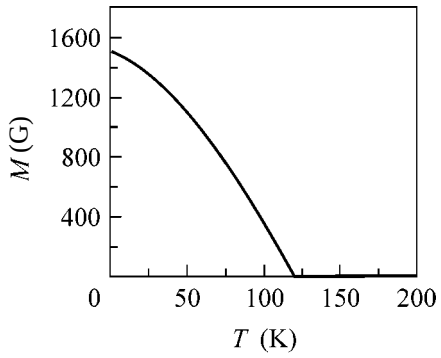

Fig. 2. Temperature dependence of the spontaneous magnetization resulting from the ordering of iron ions as calculated by formula (1).

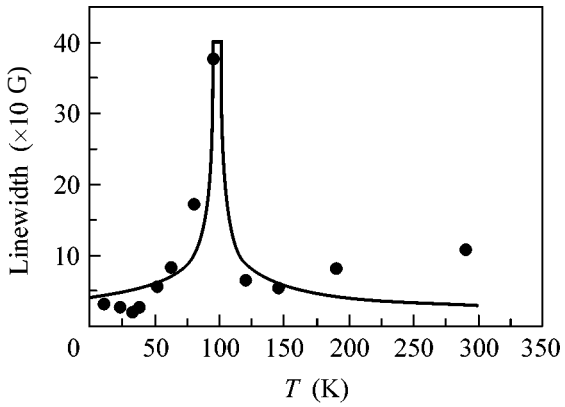

Fig. 3. Temperature dependence of the width of EPR lines of unionized iron atoms. Points correspond to the experiment, and the solid curve was obtained by formula (4) according to the Landau theory.

zation at low temperatures (as compared to the Curie temperature) is determined by the excitation of magnons and can be approximately described by the formula ([4], p. 22)

$$M_0(T) = M_{00}(1 - (T/T_c)^{3/2}). \quad (1)$$

Although this formula is obviously invalid for an ordered ferromagnet at temperatures close to the Curie point, we have used it for a rough description of the position of resonance lines at $T < T_c$ (the grounds for such a processing of the results and the reason for good agreement with experiment will be given below).

Figure 2 shows the temperature dependence of spontaneous magnetization plotted in accordance with formula (1). We used these results for determining the positions of resonance lines at temperatures below the Curie point.

In the presence of ferromagnetism, the internal magnetic field differs from the external field due to demagnetization factors. The demagnetization factor is zero when the magnetic field is oriented in the wafer plane and is equal to 4π for the direction perpendicular to the wafer plane. In our geometry, the ferromagnetic resonance frequency is given by

$$\omega = g\mu_B[H_0(H_0 + 4\pi M_0(T))]^{1/2}, \quad (2)$$

whence the position of resonance in the ferromagnetic region is described by the formula

$$H_R(T) = \sqrt{H_{R0}^2 + 4\pi^2 M^2(T)} - 2\pi M(T), \quad (3)$$

where H_{R0} is the resonance field at a high temperature and M_{00} (= 239 G) was chosen so that a good agreement with experiment was achieved.

The results of calculations based on formula (3) are shown by solid curves in Fig. 1. It can be seen that the agreement with experiment is quite satisfactory.

Analysis of the temperature dependence of the linewidth reveals that experimental linewidth can be determined exactly and reliably at room temperature only for the central line. It is equal to 300 G and is virtually independent of temperature; however, a spike is observed near 100 K (Fig. 3). The resonance linewidth is apparently determined by the dipole–dipole interaction and, hence, is independent of temperature (it is difficult to answer at this stage why motion narrowing is absent). However, a considerable contribution to the linewidth comes from fluctuations of magnetization M near the Curie temperature (~100 K). Since magnetization M shifts the position of the resonance, fluctuations of magnetization lead to broadening of the resonance line. The mean square of magnetization fluctuations is given by

$$\langle(\Delta M)^2\rangle = \frac{T_c\chi}{V} \propto |T_c - T|^{-1}; \quad (4)$$

i.e., the fluctuation of M is inversely proportional to the square root of the temperature deviation from the Curie point (see [5], Section 146, p. 528). In the scaling theory (see [5], p. 542), the exponent –1 is replaced by –1.4 [4]. Taking a value of 100 K for the Curie point, we simulated the temperature behavior of the linewidth in Fig. 3 on the basis of the Landau theory without claiming an exact quantitative description of the results.

At a temperature near 100 K, ferromagnetic ordering takes place in the system of Fe ions. Since the assumption that iron ions occupy regular positions in the SmB_6 crystal lattice is groundless, it is the ferromagnetism of a disordered system [6], which is analogous in many respects to the ferromagnetism of the PdFe and AuFe alloys. It is well known that the ferromagnetic transition in such systems occurs due to the indirect exchange interaction between iron ions of the

type $V = V_0(R/r)\exp(-r/R)$, and the Curie point is determined by the percolation-theory conditions of formation of a "large cluster" of interacting ions (see [6]). It should be noted that alloys of the PdFe type with a magnetic ion concentration of 1 at. % have Curie temperatures on the order of tens of Kelvin (40 K for PdFe and 60 K for PdCo). Although ferromagnetic ordering is observed in degenerate semiconductors due to the exchange of magnetic ions via the Ruderman–Kittel–Kasuya–Yosida (RKKY) interaction, we can hardly expect that this mechanism is operative in a Kondo semiconductor with a narrow gap, in which the conduction electron concentration decreases exponentially with a decrease in temperature in the temperature range where ferromagnetic ordering is observed.

The energy of the exchange interaction of an iron ion having spin $\mathbf{S}_0$ with the surrounding fluctuating ions is equal to

$$\hat{H} = -\sum J_{0i}(\mathbf{R}_0 - \mathbf{R}_i)(\mathbf{S}_0\mathbf{S}_i). \quad (5)$$

Averaging the spin of a matrix ion over the volume and taking into account that the exchange integral decreases rapidly (exponentially) with distance from the ion, we arrive at the following approximate expression for the potential of the interaction of the iron ion with its surroundings:

$$\hat{H} \approx -J\chi\exp(-r/R)\mathbf{S}_0. \quad (6)$$

At a temperature lower than the energy gap, the main contribution to the magnetic susceptibility of a Kondo semiconductor comes from the large Van Vleck term reflecting the polarization of fluctuating ions. The indirect interaction energy increases with the susceptibility of the matrix, and, obviously, it is not surprising that the ferromagnetic ordering of impurities occurs in the region of the highest magnetic susceptibility.

Let us now consider the temperature dependence of spontaneous magnetization following from the theory of disordered ferromagnets. According to Korenblit and Shender [6], this dependence is described by a function that depends significantly on the parameter $\nu_R = (4/3)\pi nR^3$ (n is the impurity ion concentration and R is the characteristic range of the indirect interaction of iron ions). Formula (1) quite closely approximates a curve plotted in [6, Fig. 8] for $\nu_R = 5 \times 10^{-3}$ (see Fig. 4). This result justifies our procedure for finding the resonance positions at temperatures below the Curie point. Note that it would be more appropriate to find the dependence $M(T)$ from the positions of resonances and use it to determine the parameter ν_R and, hence, the range R. However, such a procedure for estimating ν_R and R is not preferred for a large width of resonance lines because of the indeterminacy associated with it.

Our estimates for $\nu_R = 5 \times 10^{-3}$ and a concentration of 1 at. % show that the characteristic range is $R \sim 2$–3 Å. This value corresponds to the ranges $R \sim 3$–5 Å in Pd (Fe, Co, Mn) alloys [6]. However, from the Curie temperature

$$T_c = U_c\frac{R}{r_0}\exp\left(-\frac{0.87}{Rn^{1/3}}\right), \quad (7)$$

where $U_c \approx U_0S^2$, $r_0 = 0.87/n^{1/3}$, and S is the spin of interacting ions, the interaction constant U_0 is estimated as $U_0 \approx 3 \times 10^5$ K, which is an inordinately large value compared to ~10^3 K for PdFe. In our opinion, this large value is due to the high magnetic susceptibility of the Kondo semiconductor, indicating a high density of states in the narrow f band of samarium. Thus, the matrix formed by valence-fluctuating ions intensifies the indirect ion exchange between impurities and is responsible for the high value of the Curie temperature.

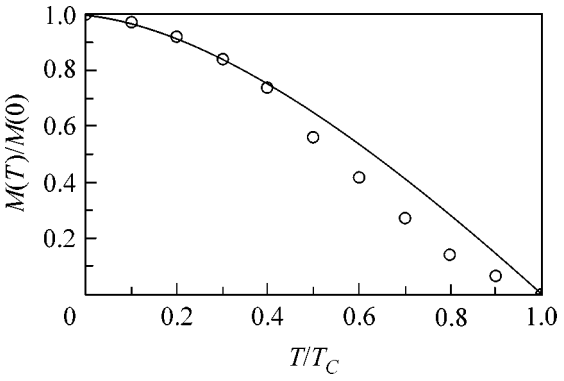

Fig. 4. (Curve) The postulated temperature dependence of spontaneous magnetization in comparison with (points) the dependence calculated by Korenblit and Shender [6] from the theory of disordered ferromagnets.

Thus, we have observed the ferromagnetic ordering of iron ions introduced as an impurity in the Kondo semiconductor SmB_6 at a relatively high temperature of 100 K and a small impurity ion concentration of about 1 at. %. This result can be attributed to the influence of the samarium hexaboride matrix formed by fluctuating valence ions. The ferromagnetic ordering of iron ions takes place as a result of their indirect interaction through polarization of the electron shells of matrix ions surrounding iron ions, and the fluctuating valence state facilitates such a polarization by weakening the rigidity of the shells being polarized.

Following advances in spintronics, considerable interest is being evinced in magnetic semiconductors with a high Curie temperature [7]. We believe that Kondo semiconductors have considerable promise as such materials.

This work was supported by the Russian Foundation for Basic Research (project nos. 03-02-17453 and 03-02-16382).

REFERENCES

1. Z. Fisk, J. L. Sarrao, S. L. Cooper, *et al.*, Physica B (Amsterdam) **223–224**, 409 (1996).
2. A. Abragam and B. Bleaney, *Electron Paramagnetic Resonance of Transition Ions* (Clarendon, Oxford, 1970; Mir, Moscow, 1973).
3. G. W. Ludwig and H. H. Woodbury, in *Solid State Physics*, Ed. by F. Seitz and D. Turnball (Academic, New York, 1962), Vol. 13, p. 223.
4. A. Z. Patashinskiĭ and V. L. Pokrovskiĭ, *Fluctuation Theory of Phase Transitions*, 2nd ed. (Nauka, Moscow, 1982; Pergamon, Oxford, 1979).
5. L. D. Landau and E. M. Lifshitz, *Course of Theoretical Physics*, Vol. 5: *Statistical Physics*, 4th ed. (Nauka, Moscow, 1995; Butterworth, London, 1999).
6. I. Ya. Korenblit and E. F. Shender, Usp. Fiz. Nauk **126**, 233 (1978) [Sov. Phys. Usp. **21**, 832 (1978)].
7. T. Dietl, Semicond. Sci. Technol. **17**, 377 (2002).

Translated by N. Wadhwa

JETP Letters, Vol. 81, No. 9, 2005, pp. 479–483. Translated from Pis'ma v Zhurnal Éksperimental'noĭ i Teoreticheskoĭ Fiziki, Vol. 81, No. 9, 2005, pp. 595–599.

Crystal–Quasicrystal Local Structural Transition in Al–Cu–Fe

A. P. Menushenkov[1], Ya. V. Rakshun[2], M. N. Mikheeva[3], K. V. Klementiev[4], A. A. Teplov[3], and A. M. Bryazkalo[3]

[1] *Moscow Engineering Physics Institute (State University), Kashirskoe sh. 31, Moscow, 115409 Russia*
e-mail: menushen@htsc.mephi.ru

[2] *Budker Institute of Nuclear Physics, Siberian Division, Russian Academy of Sciences, pr. Akademika Lavrent'eva 11, Novosibirsk, 630090 Russia*

[3] *Russian Research Centre Kurchatov Institute, pl. Kurchatova 1, Moscow, 123182 Russia*

[4] *HASYLAB, DESY, D-22607 Hamburg, Germany*

Received April 4, 2005

The rearrangement of the local environments of copper and iron in the ternary alloy $Al_{65}Cu_{22}Fe_{13}$ in transition from a crystalline phase to a quasicrystalline phase has been studied by combined extended x-ray absorption fine structure (EXAFS) and x-ray absorption near-edge structure (XANES) analysis. It has been found that the nearest environment of copper retains symmetry characteristic of a crystal; however, a turn and small shifts of copper matrix atoms causes a considerable rearrangement of aluminum atoms around iron. As a result, icosahedral clusters with pentagonal symmetry are formed around iron atoms, and translational symmetry breaking is accompanied by the transition of $Al_{65}Cu_{22}Fe_{13}$ to a quasicrystalline state. © *2005 Pleiades Publishing, Inc.*

PACS numbers: 61.10.Ht, 61.44.Br

Quasicrystals (quasiperiodic crystals) form a new class of solids whose properties cannot be described in terms of classical crystallography [1]. They are intermediate in degree and character of order between amorphous and crystalline materials: in the absence of translational symmetry, they retain long-range order in the spatial arrangement of atoms. Although all of the components of quasicrystals are good metals, the density of electronic states at the Fermi level exhibits a pseudogap-like feature. The specific resistance of a quasicrystalline phase is higher than the resistance of alloys in both crystalline and amorphous states by more than one order of magnitude because of electron localization on stable atomic configurations (clusters), which serve as deep potential well traps for valence electrons [2]. The symmetry of clusters, in particular, pentagonal symmetry, is noticeably different from the symmetry of a matrix; this is indicative of the formation of new short-range order [3]. The processes of local atomic ordering in a transition from a crystalline to a quasicrystalline state are not clearly understood. This is primarily due to the weak sensitivity of integrated techniques (x-ray diffraction analysis and neutron scattering) to local structure peculiarities. Obvious advantages of x-ray absorption spectroscopy for studying local structural ordering in quasicrystals have not been adequately used.

To fill the above gaps, in this work, we performed a comparative study of quasicrystalline and crystalline Al–Cu–Fe phases of the same stoichiometric composition using combined extended x-ray absorption fine-structure (EXAFS) and x-ray absorption near-edge structure (XANES) analysis. The aim of this study was to determine the local mechanism of transition from a crystalline to a quasicrystalline state. A combination of the above two techniques allowed us not only to determine coordination numbers, interatomic distances, and atomic species in the nearest environments of copper and iron in a quasicrystal but also to refine the character (symmetry) of their mutual arrangement.

Quasicrystalline $Al_{65}Cu_{22}Fe_{13}$ samples were synthesized by mixing electrolytically pure metal powders and thermally treating the dried mixture in a vacuum at 800°C for 2 h. The prephase crystal samples resulted from a thermal vacuum treatment at 500°C for 20 min. According to x-ray diffraction analysis, an icosahedral structure (*i*2213) or a tetragonal ω phase (ω2213) accounted for more than 95% of the quasicrystalline or prephase crystal samples, respectively.

The XAFS measurements above the *K* edges of copper (8978.7 eV) and iron (7111.3 eV) were performed at the E-4 station of the HASYLAB synchrotron center, DESY. The use of a double crystal Si(111) monochromator gave an energy resolution of ~1.2 or ~1.0 eV in the Cu or Fe *K*-edge region, respectively. The temperature over the range 20–300 K was controlled with a closed-cycle helium cryostat and kept constant to within 1 K. The EXAFS spectra were processed using the VIPER [4] and IFEFFIT [5] programs in accor-

0021-3640/05/8109-0479$26.00 © 2005 Pleiades Publishing, Inc.

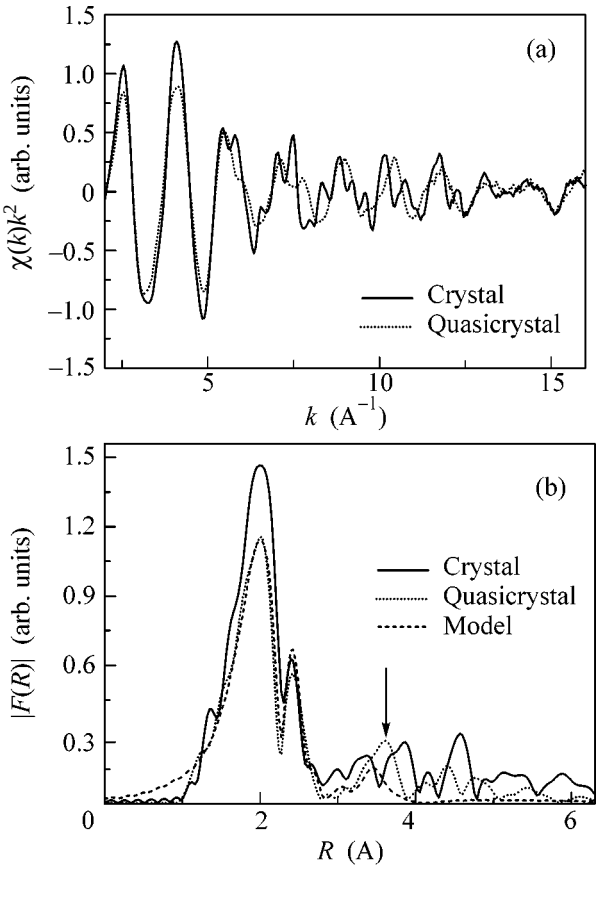

Fig. 1. (a) EXAFS function $\chi(k)k^2$ measured above the *K*-absorption edge of Cu at 20 K and (b) the Fourier transform $|F(R)|$ of this EXAFS function. The solid, dotted, and dashed lines correspond to the ω2213 crystal, the *i*2213 quasicrystal, and the simulation result for the quasicrystal, respectively.

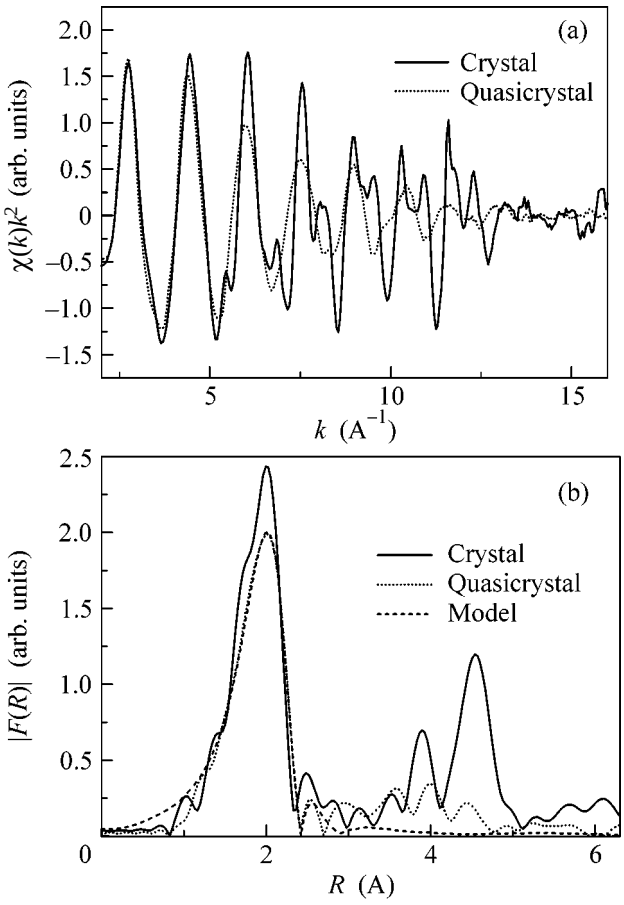

Fig. 2. (a) EXAFS function $\chi(k)k^2$ measured above the *K*-absorption edge of Fe at 20 K and (b) the Fourier transform $|F(R)|$ of this EXAFS function. The solid, dotted, and dashed lines correspond to the ω2213 crystal, the *i*2213 quasicrystal, and the simulation result for the quasicrystal, respectively.

dance with a standard procedure for the extraction and Fourier analysis of the EXAFS function

$$\chi(k) = -S_0^2 \sum_n \frac{1}{kR_n^2} N_n |f_n(\pi, k)| \times \sin(2kR_n + 2\delta_1(k) + \phi_n(\pi, k)) e^{-2\sigma_n^2 k^2}, \quad (1)$$

where N_n is the coordination number; R_n is the average radius of the *n*th coordination sphere; and σ_n is the standard deviation of the interatomic distance from its average value, referred to as the Debye–Waller factor. The scale factor S_0^2 takes into account multielectron effects. The amplitudes $f_n(\pi, k)$ and the backscattering phases $2\delta_1(k) + \phi_n(\pi, k)$ were calculated using the FEFF-8.20 program [6].

The use of a special procedure that allowed us to increase the time of data acquisition with increasing the photoelectron wave vector ~k^2 together with measuring the spectra at low temperatures ensured a high signal-to-noise ratio up to $k \approx 16$ Å^{-1} (see Figs. 1a, 2a). This procedure considerably improved the reliability of data extracted from the EXAFS analysis, as compared with previously published data [7, 8], which were obtained in the analysis of shorter spectra to 12 Å^{-1}.

Figures 1 and 2 show the experimental EXAFS functions $\chi(k)k^2$ measured at $T = 20$ K above the *K* edges of copper and iron and the magnitudes of the Fourier transform $|F(R)|$ of the EXAFS functions of a crystal and a quasicrystal. Note that the positions of $|F(R)|$ maxima differ from the real positions of atoms because of a phase shift of photoelectron backscattering (1). The true interatomic distances were extracted by the simulation of experimental EXAFS functions. The table summarizes the results of EXAFS analysis. The main $|F(R)|$ peaks for the crystalline and quasicrystalline phases were identified based on x-ray diffraction analysis, which demonstrated that the structure of an ω2213 prephase is close to the *P*4/*mnc* structure of a

well-studied analog crystal of Al_7Cu_2Fe (for example, see [9, 10]).

It can be seen in Fig. 1 that both the EXAFS functions of the crystal and quasicrystal measured above the *K* edge of copper and the magnitudes of the Fourier transform of these functions are similar to each other. A decrease in the $|F(R)|$ maximum amplitudes in the region 1.0–2.8 Å for the quasicrystalline sample is due to a structural disorder in the nearest environment of copper. Differences in a more distant region to ~3.5–4.1 Å are more significant; however, the main peculiarities are repeated with a shift of corresponding peaks toward shorter distances.

An analysis of the spectra demonstrated that a model that uses environmental parameters in a prephase crystal at fixed coordination numbers and varied interatomic distances adequately describes the local environment of copper in the quasicrystal (see the table). In this case, the best fit of a model spectrum to the experimental one was achieved by the replacement of some Al(4) atoms by iron atoms. The model adequately describes not only the splitting of the first sphere but also a maximum at a distance of ~2.7 Å (see Fig. 1b). At the same time, the peak at 3.7 Å marked with an arrow does not appear in model spectra because it is due to multiple scattering effects. Thus, the EXAFS analysis data suggest that the quasicrystal inherited a local structure around copper atoms from the crystal with a shift and splitting of the nearest coordination spheres.

At the same time, the structure of the local environment of iron changes radically after the transition to a quasicrystalline state. This change manifested itself in a dramatic decrease in the amplitude of the experimental EXAFS function (Fig. 2a). The shape of the Fourier transform of the EXAFS function of the quasicrystal is more characteristic of an amorphous system (Fig. 2b). The shape and position of the $|F(R)|$ peak corresponding to the nearest coordination sphere change, whereas

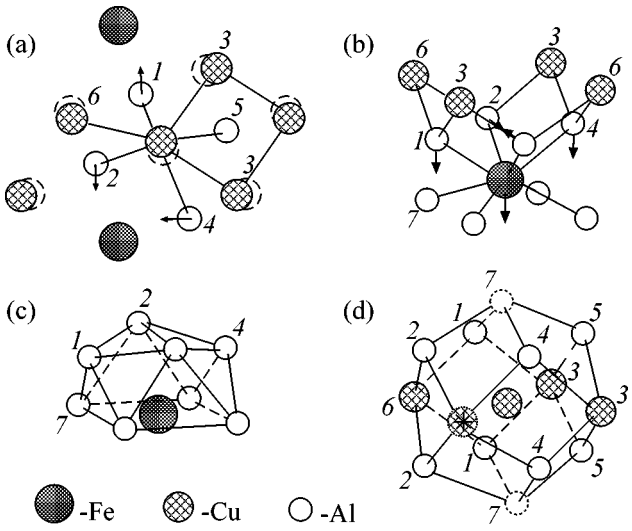

Fig. 3. Schematic diagram of local structure rearrangements in the formation of a quasicrystal: (a) the rotational displacement of a copper subsystem (viewed along the *c* axis), (b) the displacements of aluminum atoms to form an icosahedral cluster around iron atoms, (c) the upper part of an icosahedron around iron, and (d) the formation of a dodecahedron around copper. A vacancy in the environment of copper is indicated with an asterisk.

the next nearest environment spheres at distances of ~2.9 and ~4.5 Å are practically indistinguishable. This behavior is indicative of both an atomic rearrangement within the nearest sphere and a disorder in the arrangement of atoms outside the nearest environment sphere of iron within the quasicrystal.

Of course, these dramatic changes cannot be described within the framework of a crystalline approximation, as in the case of the analysis of the local environment of copper. Previously [11], we found that the best simulation of the experimental Fe *K*-edge EXAFS function was achieved when the first coordination

Parameters of the nearest environments of copper and iron atoms in a crystal and a quasicrystal of $Al_{65}Cu_{22}Fe_{13}$ at $T = 20$ K. The distances were measured to within 0.01 Å. X-ray diffraction data for an analog crystal of Al_7Cu_2Fe [10] are marked with an asterisk

K edge	Crystal				Quasicrystal		
	atom	*N*	*R**, Å	*R*, Å	atom	*N*	*R*, Å
Cu	Al(1)	2	2.506	2.46	Al	2	2.47
	Al(2)	2	2.516	2.53	Al	2	2.52
	Cu(3)	2	2.610	2.59	Cu	2	2.64
	Al(4)	2	2.620	2.59	Al(Fe)	2	2.59
	Al(5)	2	2.710	2.69	Al	2	2.68
	Cu(6)	1	3.023	3.02	Cu	1	2.83
Fe	Al	1	2.447	2.33	Al	9	2.52
	Al	4	2.475	2.45	Cu	3	2.59
	Al	4	2.478	2.64			

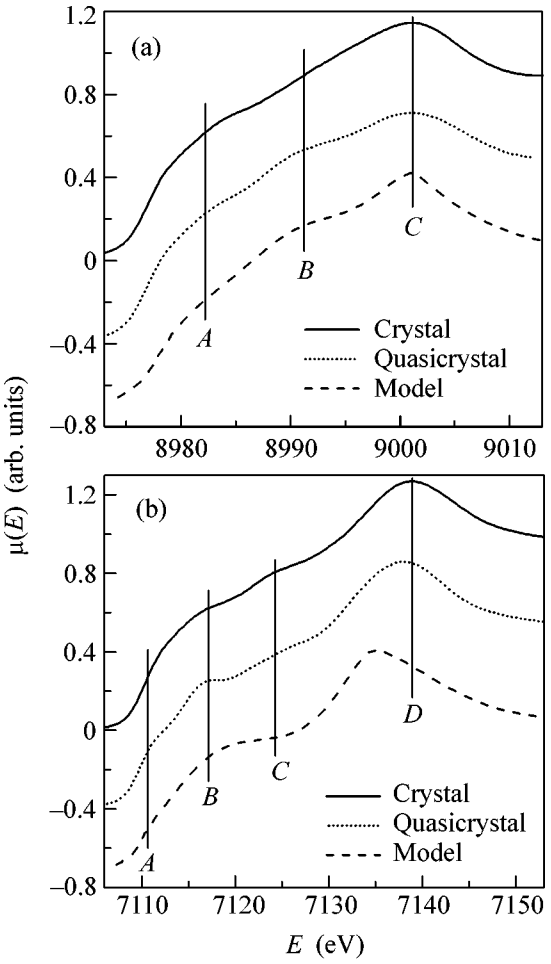

Fig. 4. Shapes of the *K*-absorption edge in (solid line) a crystal of the ω2213 prephase and (dotted line) an *i*2213 quasicrystal at 20 K for (a) copper and (b) iron. The dashed lines indicate the results of a simulation for the quasicrystal.

sphere around iron was an icosahedron. However, unlike Sadoc *et al.* [7] and Gomilsek *et al.* [8], who also used an icosahedral environment, we found that, in addition to aluminum atoms, copper atoms also entered the nearest sphere. These copper atoms occupied the positions of some aluminum atoms in the prephase crystal (see the table). Correspondingly, as noted above, iron atoms with the coordination number $N \approx 0.5$ were found in the positions of some aluminum atoms in the nearest environment of copper within the quasicrystal.

Using the results of the combined EXAFS analysis of the peculiarities of the local environments of copper and iron, we propose the following mechanism of the local structure ordering of an *i*2213 quasicrystalline phase. In the transition from the crystal to the quasicrystal, the distance between the central atom of copper and copper atoms located in *3*-positions somewhat increases and the distance to copper atoms in *6*-positions decreases more significantly (see Fig. 3a and the table). With the retention of the symmetry of the local structure around copper atoms as a whole, the described change in distances can result from a turn of the squares of copper atoms (with a simultaneous increase in the side of the square) toward the nearest atoms of aluminum. Because the Cu–Al distances remain almost unchanged after the transition to the quasicrystalline phase, the aluminum atoms that surrounded copper shifted, following copper atoms with respect to iron, to form an icosahedral cluster of pentagonal symmetry with an iron atom at the center (see Figs. 3b, 3c).

A study of the XANES *K*-edge shapes of copper and iron shown in Figs. 4a and 4b, respectively, supports the proposed mechanism. As is seen in Fig. 4a, the absorption-edge structure of copper changes only slightly after the transition from the crystal to the quasicrystal. The greatest changes are associated with an increase in the amplitude of peak *B* and a decrease in the amplitude of the main maximum *C*. The retention of the energy positions of the main spectral singularities suggests a similarity between the symmetries of the nearest environments of copper atoms in the crystal and quasicrystal.

Changes in the shape of the absorption edge of iron are more significant: along with a strong increase in the amplitude of peak *B*, an energy shift of maxima *A*, *C*, and *D* is observed, which is indicative of a symmetry change in the local environment of iron.

The XANES spectra were simulated using the FEFF-8.20 program [6], which is based on the *ab initio* calculation of absorption spectra. The exact description of the shape of an absorption edge was beyond the scope of this work. We attempted to choose a model for local environments that most adequately describes the energy positions of the main spectral singularities at reasonable cluster sizes.

In the shape analysis of the Cu *K* edge in a quasicrystal with the use of various clusters [12], a model in which the first coordination sphere around copper atoms is a dodecahedron was found to be most adequate. The results of an optimum simulation are shown in Fig. 4a as a dashed curve for a cluster of 57 atoms with a size of 5.23 Å. An increase in the cluster size results only in an increase in the running time and does not significantly improve the quality of simulation. This is additional evidence for the retention of symmetry and a sufficiently high degree of order of the local environment of copper in the quasicrystal.

The occurrence of several nonequivalent iron positions in a quasicrystal [13] makes an unambiguous simulation of the shape of the Fe *K* edge difficult. An icosahedral model was found better. In this case, a local character of ordering in the nearest environment of iron was supported by the fact that satisfactory results were obtained only with the use of sufficiently small clusters of size 4.61 Å (43 atoms). An increase in the cluster size resulted in an impairment of the simulation results. This suggests a symmetry breaking and supports the

EXAFS-based conclusion on structural disorder outside icosahedral clusters in the environment of iron.

Thus, a combined EXAFS and XANES analysis above the *K*-absorption edges of copper and iron allowed us to find characteristic changes of the local structure upon a transition from a crystalline to a quasicrystalline state. Figure 3 schematically shows these structural changes.

In accordance with the results of EXAFS analysis, a turn of copper squares causes a rearrangement of aluminum atoms. This results in the formation of icosahedral clusters around iron. These changes are described as phases (a) and (b) in Fig. 3. Figure 3c shows the upper part of an icosahedral cluster around iron and Fig. 3d demonstrates the resulting cluster as a dodecahedron formed around copper atoms in accordance with the results of XANES analysis. Vertex positions *7* are close to the positions of Al in a crystal, whereas a site in the plane saturated with copper is vacant. The vacancy occurs at distances of ≃2.5 and ≃4.0 Å from the nearest copper atoms.

The occurrence of a vacancy in the nearest environment of copper in the quasicrystal is consistent with the results of quasielastic neutron scattering: fast ($\tau \simeq$ 10 ps) local jumps of copper atoms to distances of ≃2.5 and ≃4.0 Å were detected [14]. In this case, the local jumps of iron atoms were much slower ($\tau \simeq 160$ ps).

In conclusion, note that the mechanism proposed for a local structural transition is consistent with conclusions on an important role of copper in the formation of electronic states on the Fermi surface in quasicrystalline Al–Cu–Fe [15]. Based on a study of x-ray photoemission, Belin *et al.* [15] demonstrated that the Cu(3*d*) states shift the densities of Al(3*p*) and Fe(3*d*) states toward higher and lower binding energies, respectively; this is favorable for the Fe 3*d*–Al 3*p* hybridization and an integral decrease in the density of states with the formation of a pseudogap on the Fermi surface.

We are grateful to N.A. Chernoplekov, M.G. Zemlyanov, P.P. Parshin, and A.V. Kuznetsov for stimulating discussions and helpful remarks and to G.V. Laskova and D.S. Shaĭtura for sample preparation and x-ray diffraction analysis. This work was supported by the Russian Foundation for Basic Research (project nos. 05-02-16996 and 04-02-16017) and the program "Universities of Russia" (project no. 146-05).

REFERENCES

1. D. Shechtman, I. Blech, D. Gratias, and J. W. Cahn, Phys. Rev. Lett. **53**, 1951 (1984).
2. V. F. Gantmakher, Usp. Fiz. Nauk **172**, 1283 (2002) [Phys. Usp. **45**, 1165 (2002)].
3. J.-M. Dubois, Mater. Sci. Eng. **294–296**, 4 (2000).
4. K. V. Klementev, J. Phys. D: Appl. Phys. **34**, 209 (2001).
5. M. Newville, J. Synchrotron Radiat. **8**, 322 (2001).
6. M. Newville, B. Ravel, D. Haskel, *et al.*, Physica B (Amsterdam) **208–209**, 154 (1995).
7. A. Sadoc, J. P. Itié, A. Polian, *et al.*, Physica B (Amsterdam) **208–209**, 495 (1995).
8. J. P. Gomilšek, I. Arčon, A. Kodre, and J. Dolinšek, Solid State Commun. **123**, 527 (2002).
9. M. G. Bown and P. J. Brown, Acta Crystallogr. **9**, 911 (1956).
10. G. T. de Laissardière, Z. Dankházi, E. Belin, *et al.*, Phys. Rev. B **51**, 14035 (1995).
11. A. P. Menushenkov, Ya. V. Rakshun, D. S. Shaĭitura, *et al.*, Poverkhnost **11**, 66 (2003).
12. K. Sugiyama, T. Kato, T. Ogawa, *et al.*, J. Alloys Compd. **299**, 169 (2000).
13. P. P. Parshin, M. G. Zemlyanov, A. V. Mashkov, *et al.*, Fiz. Tverd. Tela (St. Petersburg) **46**, 510 (2004) [Phys. Solid State **46**, 526 (2004)].
14. S. Lyonnard, G. Coddens, B. Hennion, and Y. Calvayrac, Physica B (Amsterdam) **234–236**, 28 (1997).
15. E. Belin, Z. Dankhazi, A. Sadoc, *et al.*, J. Phys.: Condens. Matter **2**, 4459 (1992).

Translated by V. Makhlyarchuk